ELECTROSPUN NYLON-6 NANOFIBER MEMBRANES FOR CAPTURING EXHALED BREATH AEROSOLS CONTAINING SUBMICRON AND NANO- SIZE PARTICLES

A Thesis

Presented to the Faculty of the Graduate School

of Cornell University

In Partial Fulfillment of the Requirements for the Degree of

Master of Science

by

Catherine Ging Reyes

August 2014

ABSTRACT

In this thesis, electrospun nanofibrous membranes for capturing submicron particles from simulated exhaled breath are investigated. Although it is known that aerosols of Influenza are responsible for increased rates of infection, studies have yet to succeed in quantifying sub-micron Influenza particles present in contagious exhaled breath. Therefore, here we observe the extent to which airborne sub-micron particles, modelling the size, and surface charge of exhaled viral particles, can be captured by electrospun Nylon-6 nanofiber media. An aerosol of salt particles was generated from an aqueous sodium chloride solution. This solution modeled an exhaled Influenza type aerosol because the majority of droplet sizes ranged from 0.52μm to 4.0μm; the typical size range of aqueous droplets in exhaled saliva. A large animal respirator simulated the process of human breathing.

During exhalation, the respirator dispersed the salt aerosol to nanofiber membranes for capture. The Nylon-6 membranes used in this study were uniformly electrospun on a large scale [15cm by 96cm] with targeted fiber diameters ranging from 100 nm to 200 nm. FESEM (Field Emission Scanning Electron Microscopy) and EDX (Energy Dispersive X-Ray Spectroscopy) were used to show that these membranes captured salt particles ranging from 30nm - 200nm (the viral particle size range reported most difficult to isolate). Nylon-6 nanofiber membranes could overall capture up to 39% higher salt aerosol concentrations than the control membranes, and did not break during the test process. BET (Brunauer-Emmett-Teller) and porometry analysis of the electrospun membranes show that small pore sizes (104nm – 122nm) and high surface areas ($44m^2/g$ – $58m^2/g$) contribute to better aerosol capture than for the control membranes. Furthermore, a cascade impactor was employed to quantify the changes in salt capture before and after the nanofiber filter membrane was using in the breathing apparatus. Compared to the control membranes, the highest percent of smallest sized aerosol droplets, between 0.52μm – 1.55μm, can be captured by all types of electrospun membranes.

Additionally, to increase hydrophilicity of the Nylon-6 membranes, poly(acrylic acid) was grafted to the Nylon-6 membrane by two methods. In the first method, poly(acrylic acid) was grafted onto the chain-end surfaces of the Nylon-6 electrospun membrane using the amine-to-carboxylic acid coupling agent: EDC (1-ethyl-3-(3-dimethylaminopropyl)carbodiimide hydrochloride). For the second method, the electrospun membranes were mutually gamma irradiated in an acrylic acid monomer solution to initiate free radical polymerization grafting. The second method resulted in high add-on of acrylic acid in the form of monodisperse beads on the surface. Found via FTIR (Fourier Transform Infrared) analysis, there is 17% - 20% chance of grafting occurring, with up to a 9% overall weight increase in the membranes. The crystalline structure of the Nylon-6 is also significantly modified in the process, with higher ΔH_m values. Overall surface area, porosity, and mechanical properties of the membranes decreased, and the salt particle capture did not improve, however.

The end use goal for the plain and surface modified nanofiber membranes is that they can serve as effective wearable textile materials to supplement the capture, and characterization, of aerosol-driven nanoscale infectious particles exhaled from human breath.

BIOGRAPHICAL SKETCH

Catherine Ging Reyes was born in New York City, on December 4, 1990. Her mother is of both Chinese and Ecuadorian descent, and emigrated from Ecuador to the United States in the 1970s. While in New York, she met Catherine's father, who is Puerto Rican, and decided to raise a family. Growing up, Catherine spent most of her time with her older brother, Denny, who often taught her about many of the subjects he was interested in school at the time. Most of these involved engineering. Through experimental games, such as building complex toy race tracks, and simply just discussing about how machines worked, Catherine developed early analytical skills, and an appreciation for scientific inquiry. This led her to later on become interested in chemistry and forensic science.

In 2008, Catherine became the first student from her public high school to be accepted to an Ivy League university with alumni trustee, and NY state funded scholarships. In 2012, she graduated from Cornell University with a bachelor's degree in Chemistry and Chemical Biology. During this time, she was given the opportunity to participate in an internship with the NYPD Forensic Science Laboratory in NYC. After learning polarized microscopy analysis on trace evidence fibers, and speaking with analysts who both had backgrounds in chemistry and textiles science, Catherine decided to continue her studies at Cornell and pursue a M.S. in Fiber Science, and a minor in chemistry.

During her master's program she became familiar with the creative and useful types of interdisciplinary work between fiber and materials scientists. Catherine is now interested in pursuing research which can combine all three of her interests and skills in: chemistry, materials science, and fiber/textile applications, for creating multi-functional, flexible materials for various practical uses. In June 2014 she began an internship in the Physics and Materials Science Research Unit at the Université du Luxembourg to coaxially electrospin liquid crystal ultraviolet light sensitive nanofibers. Catherine will also begin her Ph.D. work in Materials Science at the Université du Luxembourg in the Fall.

Dondequiera que mis aventuras me lleven,
siempre estarán en mi pensamientos :
ma, pa, Lee y abuelita.

ACKNOWLEDGMENTS

First, thanks Professor Margaret Frey, for giving me the opportunity to conduct this master's research. I didn't know much about electrospinning, nanofibers, or about anything related to textile science when I started, and by the end, my master's thesis turned into a broader-than-expected study. I've learned so much, from research to teaching, and it's in part thanks to Prof. Frey for the advice, and the freedom, to be able to work in her lab.

In the past 2 years, I learned that not all problems are solved in the time it takes a grad to get the "Free Snacks" in the mailroom. Sometimes it takes a lot of work, and this is when the communication between you and your adviser becomes crucial, regardless if you're there for a master's or a phd. Not all professors make good graduate advisers, but I'm glad I had 2 who were pretty good at being both, the second being Professor Geoffrey Coates.

Secondly, when things get difficult, it's important to have a family who you can cry and complain to, for instance, if your lab suddenly gets a postdoc who you think is going to be miserable to work with. So thanks – ma, pa, Denny-Lee & abuelita for keeping my mind in perspective, and my worries to a minimum, when unexpected surprises turned up.

Thirdly, having great technical advice from experts in materials characterization reduces a lot of frustrations. Thanks to the CCMR and Sam in HEB. This work made use of the Cornell Center for Materials Research Shared Facilities which are supported through the NSF MRSEC program (DMR-1120296).

Lastly, while on the graduate journey, I had a few friends with whom I was lucky enough to research with, have fun with, and who made life a little sweeter. Thank you all: profs, postdocs, phd and fellow master's students who have ever had a desk (or more than one) in HEB 150 – you've taught me how to smile, and sing while I work. Special thanks to: Lina, Nidia, Stephane, Minji, & Ana Cecilia, for all of your strange, and wonderful, sometimes scary, stories – they will all serve as lessons which I will take with me on the road less travelled.

TABLE OF CONTENTS

LIST OF FIGURES

2 – Literature Review

3 - Experimental Tools, Methods & Set-Ups

4.1 - Large Scale Nylon-6 Nanofiber Membrane Characterizations

4.2 - Nylon-6 Nanofiber Surface Modifications: Two Graft Methods

4.3 - Aerosol Capture Results

6 - Future Work

LIST OF TABLES

LIST OF ABBREVIATIONS

SBA: Simulated Breathing Apparatus

10CM NSM: Electrospun membrane at 10 cm, with rotating drum and **no** axial sliding mechanism

10CM SM: Electrospun membrane at 10 cm, with rotating drum and axial sliding mechanism

12.5CM SM: Electrospun membrane at 12.5 cm, with rotating drum and axial sliding mechanism

FESEM: Field Emission Scanning Electron Microscopy

EDX: Energy Dispersive X-Ray Spectroscopy

BET: Brunauer–Emmett–Teller Theory

DSC: Differential Scanning Calorimetry

AFM: Atomic Force Microscopy

H1N1: Haemagglutinin glycoprotein 1, Neuraminidase enzyme 1 found on Influenza virus surface

QtPCR: Quantitative Polymerase Chain Reaction

RNA: Ribonucleic Acid

^{99m}**Tc:** Technetium 99m isotope

NIOSH: National Institute for Occupational Safety & Health

DMA: Differential Mobility Analyzer

CPC: Condensation Particle Counter

PAA: Poly(Acrylic Acid)

AAc: Acrylic Acid

EDC: 1-ethyl-3-(3-dimethylaminopropyl)carbodiimide hydrochloride

Sulfo-NHS: N-hydroxysulfosuccinimide

1 – INTRODUCTION

Though it's known that Influenza is transmittable via aerosols produced by coughs and sneezes, studies examining the sizes and concentrations of these exhaled viral particles are limited.[14, 16, 100] Known strains of Influenza A, B and C can be between 80 nm to 120 nm in diameter, and many attempts throughout the years have been made to try to capture these smaller particles from exhaled breath of infected individuals. [101]

In this thesis, we investigate how Influenza-like particles flowing in an air stream simulating human breathing can be captured using nanofiber membranes. The aerosol particle size distribution and concentration are determined by examining the nanofiber membrane after aerosol exposure. The methods used to characterize the particle capture range from using spectroscopic and microscopic instrumentation; gravimetric analysis, FTIR, and FESEM, to name a few. Discussions evaluating the usefulness and significance of using such methods for nanoscale particle characterization on the electrospun nanofiber membranes will follow.

To simulate the exhalation of airborne Influenza particles, a large animal respirator will disperse a nebulized sodium chloride solution with a variety of submicron and nano-sized particles for capture. Though electrospun membranes have been used in filtration applications, the idea of combining their use with wearable textiles in commercial clothing is still in its infancy. Electrospun membranes to capture these salt particles may elucidate the potential for implementing thin layers of nonwoven nanofibers layers into protective textiles, such as surgical masks. Such a combination can further lead to the implementation of other technologies, such as microfluidic channels and microchips, to have the membranes function as sensors and detection devices. They may also provide methods for isolating hazardous nanoparticles for further study.

Nanofibers of various polymer blends and chemical functionalities can be obtained through the process of electrospinning, and have already been used in biological and

industrial fields.[24-26] In particular, Nylon-6 is known to be chemically resistant to many natural environments, has high tensile strength, and can easily create nanofibers.[30] Chapter 2 discusses current literature on methods used to capture Influenza particles, as well as the difficulties in assessing the ability to capture and detect smaller, more easily inhalable particles. Motivations for using nanofiber membranes as potential capture devices are justified using theoretical considerations of air flow around the fibers; Knudsen number, and slip-flow theory. Additionally, the electrospinning method for nanofiber production and possibilities for further Nylon-6 nanofiber functionalization with other polymers (acrylic acid and poly(acrylic acid)) via grafting are reviewed.

Chapters 3 discusses the specific electrospinning process undertaken to fabricate the Nylon-6 nanofiber membranes using a modified rotating drum collector with novel polymer solution transport. The assembly for the apparatus used in dispersing the model viral aerosol (a sodium chloride solution) for capture onto the nanofibers is also detailed. Experimental trials in capturing the salt aerosol onto three nanofiber membranes, each fabricated with different specifications, and one commercial filter type are examined. Spectroscopic and analytical characterization methods used to quantify salt capture, and examine the extent of grafting functionalization are considered.

Chapter 4 will summarize the main findings of this study starting with a consideration of how large scale nanofiber membranes with specific fiber diameters can be electrospun with uniform tensile properties. Three methods to measure porosity quantitatively using: capillary porometry, BET analysis, and ImageJ SEM image analysis software were performed. The results of attempted grafting experiments using poly(acrylic acid) and confirmation of success are also noted with considerations as to how aerosol capture is influenced by these functionalized membranes. Analysis of the salt aerosol capture trials performed on these membranes in comparison to the aerosol captured onto the commercial filter is examined in detail.

Finally, assessments of equipment limitations present in this study, conclusions, and recommendations for further nanofiber modification to enhance aerosol particle capture are discussed in Chapters 5 and 6.

2 – LITERATURE REVIEW

2.1 – Influenza Size Range & Viability as an Aerosol

Typical infectious viruses range from 30nm to 300nm in size. Currently, the largest known virus discovered in 2003, Mimivirus, shows a diameter of ~750 nm.[1] Known strain particles of Influenza A – C exhibit diameters ranging from 80 nm to 200 nm. Individually observed Influenza virion particles through AFM (Atomic Force Microscopy) have shown viral spherical envelopes, the layer containing glycoprotein "spikes" used by the virus to infect host cells, to be ~8nm to ~12 nm in diameter.[2] However, Influenza particles are known to aggregate based on changes in pH and form clusters, as well as "honeycomb" like structures.[2] These effects further make identifying the true size of viral particles difficult, and their reported cluster sizes can go up to ~400 nm. Decades of study focusing on the transmission pathways of pathogens have concluded that 3 general routes of infection exist, they are: 1. infection through direct contact (touching, biting...etc.), 2. infection through indirect contact via air or another medium (coughing, sneezing), and 3. infection through vectors (disease carriers which transmit pathogens).[3-5]

Because of recurring outbreaks of Influenza virus throughout the last five years, the focus in epidemiology studies has shifted to determining whether Influenza is most transmittable via the aerosol borne indirect contact pathway.[6-9] Several reports on the ability of viral aerosols to remain airborne for long time periods and travel at significant speeds (up to 200 m/s when coughing) have been confirmed.[10-13] However, normal respiration patterns without significant sneezing and coughing have been shown to account for most viral particle dispersion.[10] Currently, it's known that approximately 64% of the Influenza A (H1N1) particles smaller than 2.5 μm can remain aerially suspended on commercial airplanes, health and day-care centers for hours.[14, 15] Additionally, it's now known that these smaller nanosize clusters ranging from 200 nm to 400 nm can, be small enough to be within the normal human inhalable range (particles may be ≤ 4 μm).[16, 14]

2.2 – Methods Applied for Capturing Viral Nano & Micron Particle Aerosols

Methods for attempting to capture and isolate these viral particles expelled in human breath have ranged from using viral replication assays, QtPCR (quantitative polymerase chain reaction), to various bioaerosol and cascade impactor samplers.[16-18] To date, there has been difficulty in quantifying and capturing airborne Influenza particles because of their expansive size range, from nanometers to microns, and because of the relatively still unknown ways in which these particles behave in aerosols travelling through air.[19] Additionally, modeling aerosol formation that can simulate human breathing or coughing has also been difficult to stimulate.

Figures 2-1 and 2-2, below, show two independent experimental designs where aerosols have been produced to simulate airborne particle flow and potential capture methods. In Figure 2-1, active H1N1 viral strains were nebulized via compressed air and dispersed through 4 commercial capture devices to determine their efficiency in capturing large viral concentrations. QtPCR analysis was used to determine viral RNA (Ribonucleic Acid) concentrations collected from each device. Viral nucleic acid assays examined the capture virus infectivity.

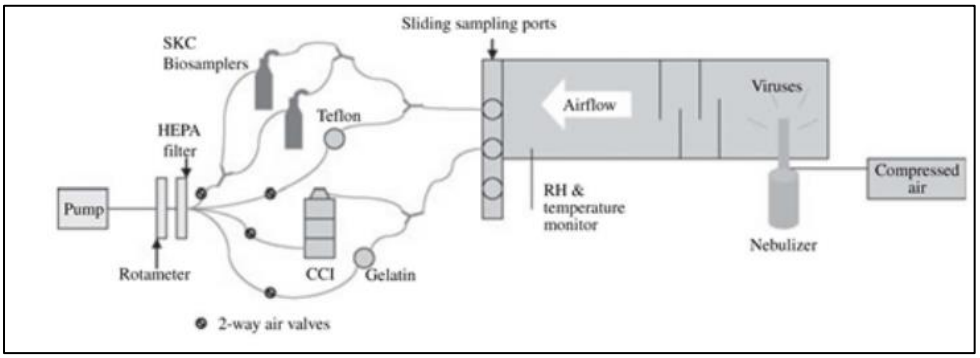

Figure 2-1: Experimental setup for aerosolizing and capturing Influenza viral particles using 4 different types of capture media.[17]

In this case, final conclusions were that commercially available SKC™ Bioaerosol samplers were best for capturing viral particles and preserving their infectivity. However, it

was noted that these samplers required the use of a liquid medium in order to trap the viral particles. It would also be mostly ineffective for capturing aerosols with particles smaller than 1µm.

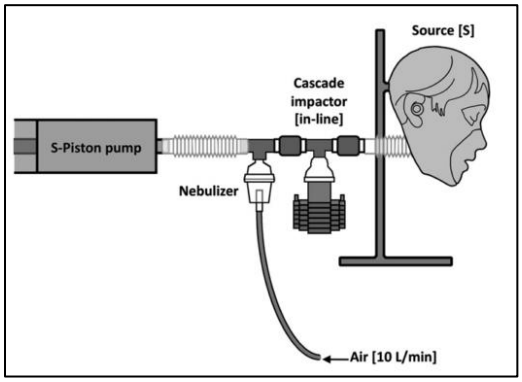

Figure 2-2: Experimental setup for aerosolizing and dispersing isotope labeled saline solution. This setup models human breathing mechanism.[20]

Figure 2-2, shows an experimental design involving simulated human respiration using a large animal respirator, expelling an aerosol of ^{99m}Tc (Technetium-99m) labeled saline solution, through a mannequin face to model the efficiency of current NIOSH approved protective and surgical masks at preventing viral/pathogen exposure. Using an 8-stage cascade impactor, for collecting particles sized between 0.54 µm - 21 µm, it was found that most aerosol particles were able to be deflected by regular surgical masks when compared to NIOSH (National Institute for Occupational Safety and Health) N95 respirators. Two suggestions for mask modification made by the researchers were to: alter the particle deflection paths on the masks by changing the mask shape, and to change the fit of the mask for users.[20] These two alterations could greatly improve bioaerosol pathogen capture.

Surgical safety masks are traditionally made from the melt-blowing process.[21, 22] This creates a membrane with fiber diameters ranging from 2 μm to 7 μm. The melt-blowing process involves the high speed extrusion of a melted polymer solution through various dies, and applied air pressure to solidify the polymer streams into fibers which get collected onto a screen.[23] Because nanofibers offer a smaller size range of fiber diameters, it's possible that

these electrospun materials can enhance current surgical safety masks in their particle capture capabilities, their comfort, and their fit.

2.3 – The Electrospinning Process

Nanofibers composed of various polymer blends and chemical functionalities can be obtained through electrospinning. These functionalized nanofibers have been used for improving textile, biological and industrial materials requiring specialty performance.[24-26] A high voltage potential applied to a flowing polymer solution will cause a disruption in the surface tension of the solution molecules. When the electrical field generated overcomes the solution surface tension, fibers are formed in a Taylor cone jet, and propagate onto a conductive collector.[27] A basic electrospinning setup containing the polymer solution feeding pump, the fiber membrane collector, and a voltage source are shown in Figure 2-3.

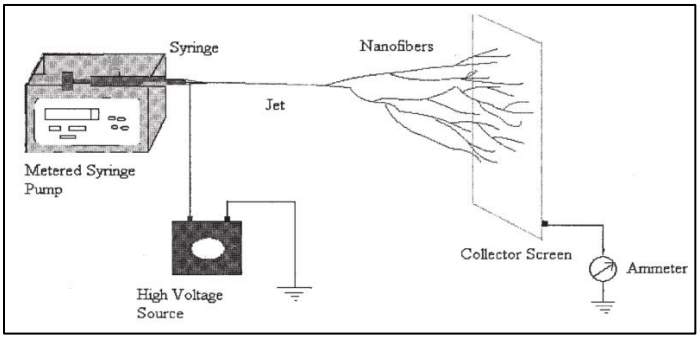

Figure 2-3 – The Electrospinning Process.[27]

The formation of the nanofiber membrane on the collector is highly dependent on five main variables: the polymer solution concentration and composition, the syringe feeding rate, the voltage applied, and the distance of the syringe from the charged collector. In varying these parameters simultaneously, or individually, nanofiber membranes with varying morphologies and properties can be created.

Yan et. al, reported on the formation of self-assembled honey-comb patterned nanofiber morphologies after electrospinning PEO [poly(ethylene oxide)], PVA [poly(vinyl alcohol)] and PAN [poly(acrylonitrile)] at varying concentrations on aluminum and plastic film

substrates.[28] Though it was originally hypothesized that the increasing charge density from the applied voltage would be enough to force the fibers away from each other, the high surface tension of the solution permitted the still wet fibers forming to join together at certain points. In other words, combinations of the surface tension from the polymer solution being fed, and the voltage difference applied, were enough to cause a structural alignment of the nanofibers into honeycomb webs (Figure 2-4a).

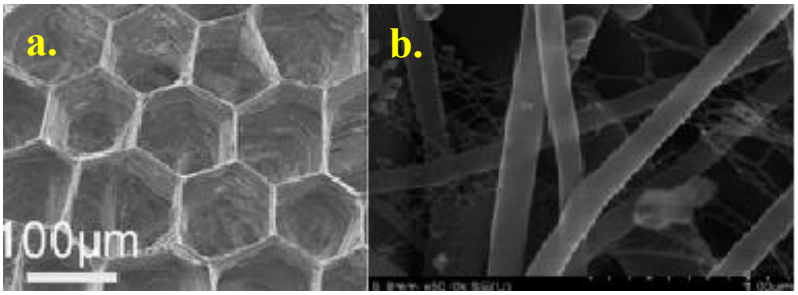

Figure 2-4a,b – Examples of alternative nanofiber structures from variations in electrospinning parameters: a. self-assembled honeycomb structured fibers, and b. gelatin powder incorporated fibers showing beads.[28, 29]

Additionally, composites of nanofibers containing chemical modifiers have also been examined. Nylon-6 is known as a polymer with high tensile strength, high elasticity, ease of electro-spinnability and resistance to abrasion.[30] Electrospun Nylon-6/gelatin composites incorporating 30wt% gelatin powder from bovine bone showed the formation of beads within the Nylon-6 membrane (Figure 2-4b). This composite was exposed to a culture of osteoblast cells for a period of 1, 2 and 7 days. Ultimately, it was found that increased gelatin within the nanofiber mat helped accelerate the binding of hydrophilic cells onto the Nylon-6 surface.[29] This suggests possible future directions for modifying known synthetic, and hydrophobic polymer nanofibers. In doping the polymer solutions prior to electrospinning, the authors have proposed a novel method for creating robust, yet biodegradable tissue scaffolds.[31]

2.3.1 – Fiber Diameter Importance in Creating Electrospun Non-Woven Filter Media

In creating filter media for particle capture, the fiber diameter size within the membrane must be considered. According to various filtration theories, fiber diameter size is inversely proportional to the amount of resistance that the fiber experiences when exposed to a fluid (air, or liquid) flowing against it. Therefore, smaller fiber diameters in a nonwoven mat will create denser fiber membranes. With denser membranes, there will be smaller pore sizes, and this contributes to low permeability and highly efficient filters.[32] Since fiber diameter size is dependent on several factors, control of this attribute involves the consideration of the aforementioned five parameters used for electrospinning. Though the electrospinning process can produce variable results the polymer composition is altered, there are consistent trends that exist for changes in feeding rates, concentration, distances and voltages applied**.**

In general, increases in the polymer molecular weight, and the solution (polymer plus solvent) concentration for electrospinning, will form membranes containing smooth, filamentous, round and beadless fibers. Figure 2-5 shows SEM images of the resulting nanofiber membrane morphologies for PVP [poly(vinyl pyrrolidone)] and PEO spun at differing concentrations.[33] Increasing the ratio of PEO to solvent will result in beadless fibers, while concentrations of PVP below 2% in solvent created a “beads-on-a-string” type morphology.[34, **35**]

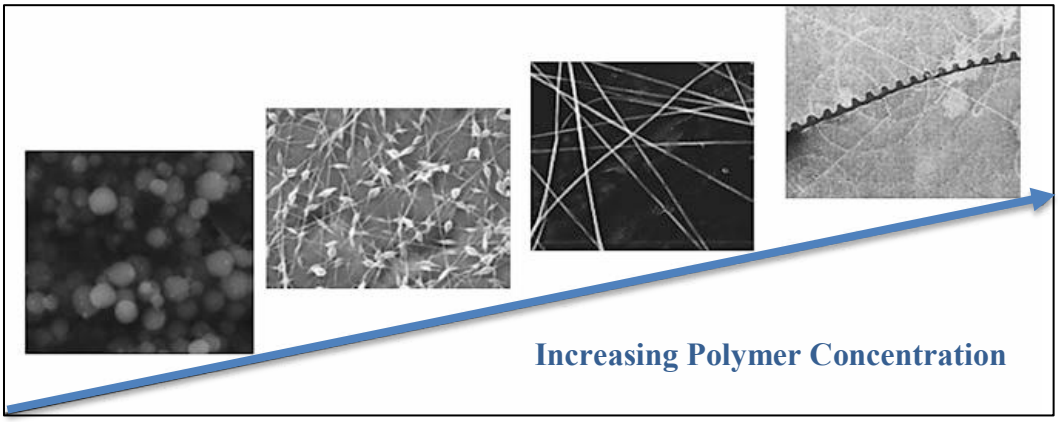

Figure 2-5 – SEM images of products resulting from electrospun low polymer concentrations (left-most image) to electrospun highly concentrated solutions (right-most image).[33]

At very low concentrations, the formation of micro particle structures will dominate; the polymer solution will have undergone an "electrospraying" process instead with no fiber formation. As the concentration increases, the surface tension within the solution also increases and the formation of fibers is more likely. This is due to heightened intermolecular interactions within the solution as it's subjected to the voltage potential.[33] Typically, after keeping all other parameters constant, increasing the solution concentration (after the appropriate concentration threshold for electrospinning has been found) will result in increased nanofiber diameter sizes within the nonwoven membrane. Nylon-6 membranes, increasing the concentration from 20wt% to 25 wt% has shown to increase the diameter size by approximately 30% - 50%.[36] Likewise, decreasing the concentration will generally result in smaller fiber diameters.

Additionally, there are instances of when increasing the amount of voltage applied to the solution can also contribute to differences in the nanofiber diameter size formed. While controversy still exists as to whether increasing the voltage alone can create narrower fiber diameters, it's generally accepted that it's a combination of the voltage applied, and the starting polymer solution conductivity, that contributes to shrinking the diameter sizes.[37, 38]

Because researchers are able to tailor electrospinning parameters to create nanofiber membranes with desired diameter sizes, the applications for these nonwovens in

filtration studies have increased. Models showing the effects of fiber cross-sectional shapes, and the effects of their cross-sectional diameter sizes, on filtering capability demonstrate how these membranes can be used to capture airborne nanoparticles.[39] Cylindrical fiber lengths and circular cross sections reduce the permeability of a filter as a whole. This is because tighter air slip streams can form around nanofibers with small diameters. These closer lying streams around the fibers can then influence the particles within the uniform air currents to be drawn to the fiber surface. This process is illustrated in Figure 2-6A,B.

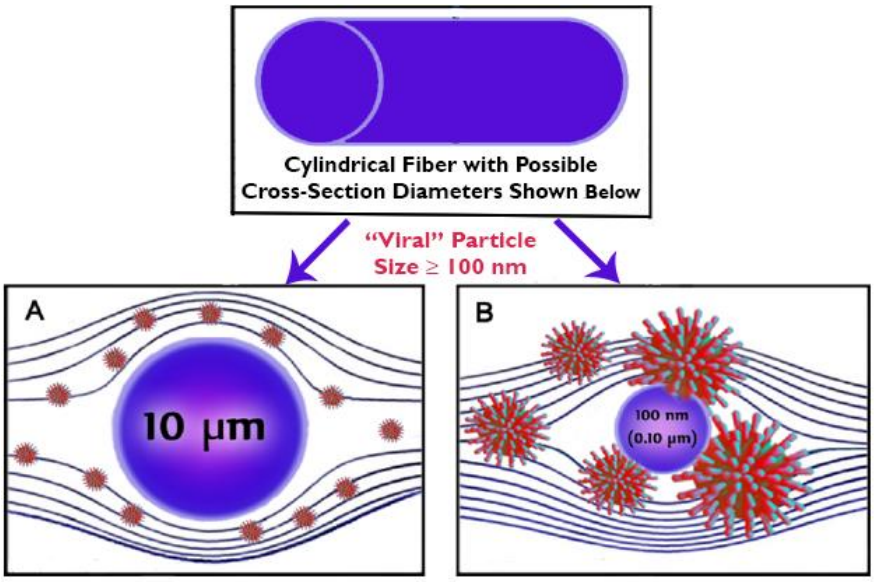

Figure 2-6A,B – Diagram showing the ability of nanofibers with small (~100nm) circular diameter cross-sections to capture aerosol particles (or viral material) that can be larger in size. This is due to the difference in slip streams formed at the fiber surface for micron fiber diameters (A) & nano fiber diameters (B).

Furthermore, Figure 2-6B also shows how increased particle capture can result from fibers with smaller diameter sizes. In considering the Knudsen number, the ratio which describes how surrounding air particles interact with the surface of the filter fiber media, calculated by:

$$K_n = \frac{\lambda}{r_f} \qquad (2.1)$$

where λ and r_f are the molecular mean free path, and the fiber radius, respectively, a theoretical fiber diameter which is optimal for air filtration can be calculated.[40, 41] In filtration

studies, the "pressure drop" for a filter can be described as the membrane's resistance to airflow, and is directly related to the filter's efficiency.[42, 43] For clean filters, the pressure drop increases with decreasing fiber diameter. As the filter becomes "dirty" during continuous particle capture, the pressure drop continues to increase, as particulate accumulation on the filter further decreases its permeability. Calculations for the pressure drop of a filter must take K_n into consideration because this value is crucial to describing the how particles in air will become trapped into the membrane. In air, at standard temperature, the molecular mean free path is generally 66 nm, and so K_n is not negligible.[41, 44] Furthermore, at low pressures and at high temperatures, λ also increases.[45]

Typically for a nanofiber membrane, where the molecular movement of the surrounding air can significantly affect the membrane, K_n is generally assumed to be > 0.1, and a non-zero air veloctity is present at the fiber surface.[41] Thus, fiber diameters less than 500 nm are most likely to generate non-zero velocity air streams nearest to their fiber surfaces.[40] This is known as the slip-flow regime. Air streams close to the nanofiber surface increase the probability that nearby particles of a larger size can collide and embed onto the fiber. These air streams also contribute to lower air drag on the fiber surface. Lower air drag explains the higher pressure drop the smaller fibers experience (Figure 2-6B). Therefore, increased particle capture becomes possible when the filter media is in the slip-flow regime. When the fibers are micron sized, such as in Figure 2-6A, slip-streams close to the fiber surface do not form, and the no-slip assumption holds. Here, particle capture is reduced because there is zero air velocity at the fiber surface. For these fibers, K_n would be significantly smaller than 0.1.

Therefore, electrospinning nanofibers with 100 nm to 200 nm diameters will facilitate the capture of larger 200 nm to 500 nm sized particles as they are carried by the fiber surface slip streams. This fiber diameter calculation depends on considerations of the known non-zero velocity at fibrous surfaces.[41] The 200 nm – 500 nm size range would be

representative of aerosol Influenza particles difficult to capture.[14, 15]

2.4 – Methods for Quantifying Particles & Residues on Surfaces & In Aerosols

The presence of particles, residues and other modifications on the surface of polymers can be quantified using a variety of means. FESEM (Field Emission Scanning Electron Microscopy) and SEM (Scanning Electron Microscopy) techniques can reveal changes in material morphology, and show the distribution of particles within a substrate.[46-48] Quantitative distributions of particle, pore, and other size features present within a sample can also be extrapolated. Regarding the differences in FESEM and SEM techniques; lower operating voltages are possible using FESEM, than SEM, to examine finer details of a specimen.[49-50] FESEM can better correct image astigmatism caused by poor beam alignment. Because astigmatism can be manually corrected, more accurate measurements of round fiber diameters, and better distinction of particulate edges are possible.

To analyze the chemical composition of materials, EDX (Energy Dispersive X-Ray) and FTIR (Fourier Transform Infrared) spectroscopic methods are often employed. Though obtaining exact atomic percentage quantities of elements is difficult for materials with irregular 3D surfaces (such as fiber membranes), these approaches give insight to element type losses and gains in a modified material.[52] In FTIR spectroscopy, the change in absorbance, or the wavenumber shift, of a known peak corresponding to a functional group in a sample, indicates changes in chemical bonding. For instance, the appearance of amide peaks in the 1530cm^{-1} to 1630cm^{-1} region for certain biological fungi can be reduced when these samples are exposed to microwaves. Excessive water that would otherwise interact with the amide groups evaporates, and the amide peaks within the spectra are reduced.[51] However, when the fungal samples are embedded in cellulose paper fibers, FTIR easily shows fungi presence from the amide peaks (cellulose does not contain these). Likewise, changes in energy counts detected for elements in EDX spectra, coupled with elemental image mapping

analysis, give precise indications of where new elemental species were introduced, and if previously known components were removed.[53-56] The homogeneity of samples, especially those altered or created through composite assembly (layer-by-layer, vapor deposition…etc.), aerosol exposure, or sol-gel synthesis, benefit from the qualitative and quantitative information obtained using EDX.

Regarding the methods used to detect the distribution quantity of particles dispersed in aerosols, instrumentation will vary based on the relative particle sizes sampled. For aerosol particles in the nanometer range, differential mobility analyzers (DMAs) coupled with condensation particle counters (CPCs) will be used.[57, 58] These devices have been used extensively in the atmospheric sciences field to determine the particle size distribution, and spread, of pollutant particles dispersed by wind.[59, 60]

Aerosols comprised of nanoparticles between 1nm and 1μm in size are captured within the DMA, which contains two electrodes for charging particles. As the particles traverse between the two electrodes in the apparatus, an electric field created charges the aerosol. The charged aerosol gets collected along the inner portion of the apparatus based on flow rate and charge. The electrical mobility of the aerosol can be related to the particle diameter through Stokes' law combining the use of the Cunningham slip factor and particle Knudson number. Thus, information of accurate particle size distributions is created. Recently, DMAs and CPCs have been used in the biotechnology field to characterize airborne viruses, proteins, and other large biological macromolecules.[61, 62] An issue with these instrumentations, however, is that they are costly and not easily combinable with other "in-lab" made equipment. Other alternatives have been to use multi-stage cascade impactors and SKC bio-samplers, aforementioned in Section 2.2.

Microscopic techniques have also been used for detecting particles in polymer membranes, matrices, and biological tissues.[63] Confocal fluorescence microscopy, which provides a true 3D resolution of the specimen by blocking the signals reflected from certain

planes, utilizes fluorophores that excite to higher energy states when struck with the microscope's laser. The fluorophores are applied to the specimen to be imaged beforehand, and once approached by the laser, features of the specimen can be differentiated from the colors emitted. Confocal fluorescent microscope images of magnetic silica beads are shown in Figure 2-7.

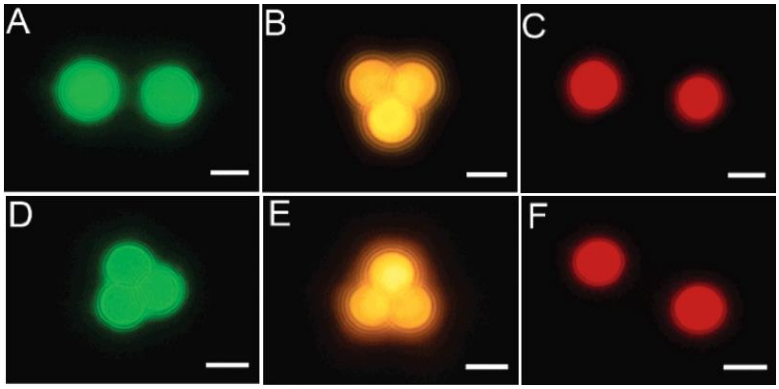

Figure 2-7 - Color fluorescence microscopic images of nonmagnetic (A-C) & magnetic silica beads (diameter: 4.0μm) doped with quantum dots emitting wavelengths at 530, 590, and 630nm.[64]

Additionally, chemical microscopy has been used since the 1940s.[65, 66] These qualitative methods for detecting the presence of elements and other ions in substances use the principles of reaction chemistry to force a visible physical change (precipitation, or dissolution) in the sample which can be observed using a basic light microscope. Often, these methods are adequate for an initial survey of chemical components.

Conductivity measurements of liquids and solids can also relate to the concentrations of known particles in liquids. However, for accurate measurements of solution conductivity, temperature compensation, probe calibration, and, if possible, a standard concentration versus conductivity curve of the desired particles in solution should be considered.[67, 68]

2.5 – Surface Modification of Nanofiber Membranes (Solution & Radiation Chemistry Methods)

Researchers have long since attempted to further modify the physical properties of electrospun nanofibers using a variety of means. Modification techniques to introduce, and successively layer, multiple chemical functionalities onto the fiber surface have varied from using wet chemical methods to using plasma and radiation graft polymerizations.[69-72] Additionally, recent developments have shown that nanofiber membranes can be used as catalysts, DNA carriers, and enzyme immobilizers.[73-75] In these instances, nanofibers can play the supporting role to aid a desired reaction taking place, as opposed to merely being the final product. The possibilities for nanofiber use in creating tissue scaffolds, battery electrode separators, and enhanced coatings via layer-by-layer assembly, to name a few, are increased after fiber functionalization. As a result, nanofibers can be used in a variety of environments.[76-78]

Nanofiber surface chemistry altered through wet chemical methods typically involves the use of reagents, such as crosslinkers, bases, or acids, to activate the desired moiety (located on a nanoparticle, polymer, cell structure…etc.) for binding to the nanofiber surface. Surface hydrolysis techniques using sodium hydroxide have been used to make the surface of PCL [poly(ε-caprolactone)] electrospun fibers more hydrophlilic to induce the proliferation of osteoblast cells.[79] Figure 2-8 compares the osteoblast cell growth on the surface modified PCL fibers against the cell growth on the non-NaOH treated fibers. While cell growth still continued on the non-treated fibers, this growth was not as dense or as widespread as that shown on the hydrolyzed fibers.

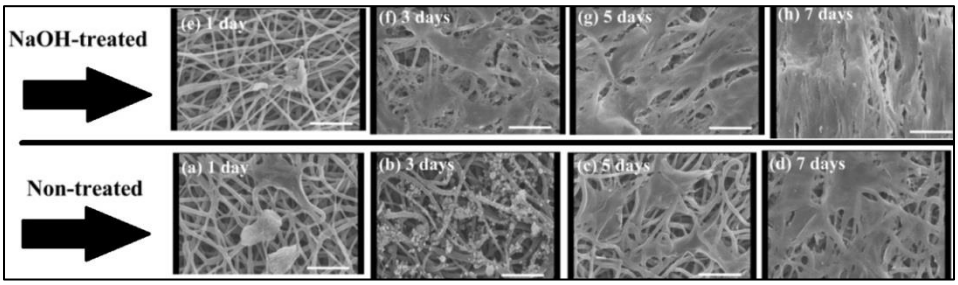

Figure 2-8 – Osteoblast cell growth on PCL NaOH hydrolyzed and non-hydrolyzed fibers (Scale Bar: 30µm).[79]

In another instance, pre-manufactured Nylon-6 films were grafted with AAc [acrylic acid] using solution methods to enhance the conductivity of the films for use in alkaline storage batteries.[80] Prior to monomer exposure, the films had been swelled in an aqueous solution of formic acid. This precursor step was performed to ensure that the initiator would disperse uniformly throughout the film during grafting. The presoaked dry films were then introduced to a solution of ceric ammonium nitrate, sulfuric acid and AAc. Ceric ammonium nitrate, CAN, along with other inorganic salt reducing and oxidizing agents (potassium per sulfate, ammonium per sulfate…etc.) have historically been used as initiators to graft copolymerization.[81, 82] Figure 2-9 shows the proposed grafting mechanism using CAN as the initiator to bind AAc to the amide groups on the Nylon. Conductivity results of the AAc-g-Nylon-6 films were found to increase with increasing degree % of grafting (found by gravimetric means).

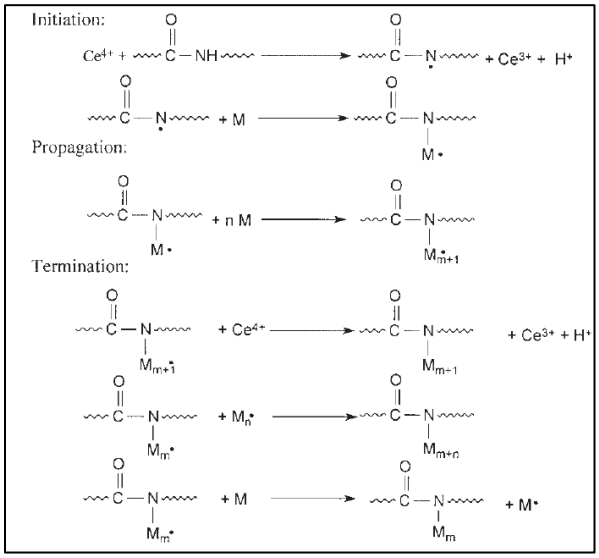

Figure 2-9 – Reaction mechanism using CAN, Ce4+, as an initiator to graft AAc to Nylon-6 films.[82]

Overall, wet chemical techniques have shown to be effective approaches to modifying the surface of fiber membranes and films. These are relatively quick methods, mostly limited by the process of determining appropriate solution concentrations, but which

can yield effective results. A similar approach to Nylon film surface modification has used the zero-space crosslinking agent EDC (1-ethyl-3-(3-dimethylaminopropyl)carbodiimide hydrochloride) coupled with the intermediate stabilizer NHS (N-Hydroxysuccinimide).[83] Here, PAA [poly(acrylic acid)] was grafted onto the amine end groups of Nylon-6,6 films using EDC as an amidazation facilitator for carboxylic acid attachment.

PAA is known for its moisture regain and resistance to UV (ultra violet) degradation. Studies have also emphasized the ability of PAA to act as an adhesive for tissue surfaces; making it suitable for biological purposes.[84] These properties can increase the breathability and prolonged use of Nylon film. For electrospun Nylon membranes, it can potentially improve the texture of surgical masks and other personal protective applications. In the presence of water, PAA becomes anionic, losing its proton from the hydroxyl group. As an anionic polyelectrolyte, PAA can further enable the attachment of positively charged nanoparticles (antibacterial agents) through electrostatic attractions between the two surfaces.[85] Figure 2-10 shows the proposed scheme for the activation of PAA and Nylon-6 by EDC.

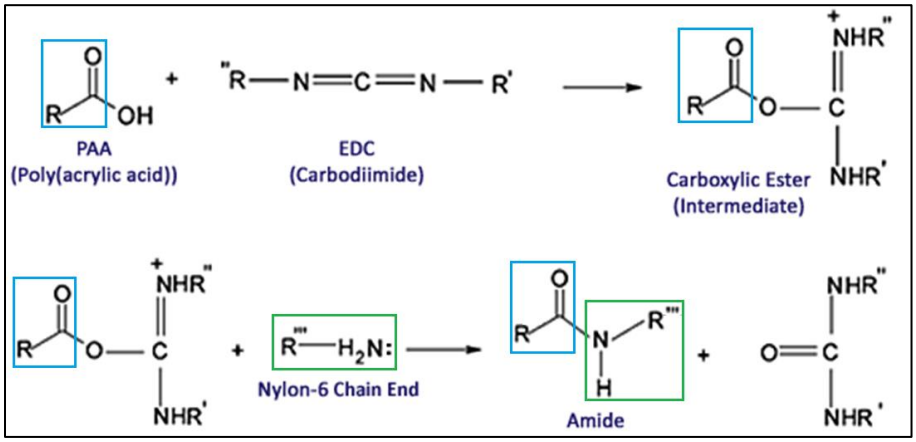

Figure 2-10 – Amidization of PAA (functional group: blue) with EDC carboiimide makes an ester intermediate. The intermediate undergoes nucleophilic substitution with Nylon-6 amine (green) to form the desired new amide linkage.[85]

Using NHS to further stabilize the O-acylisourea carboxylic intermediate formed will

give rise to the activated succinimyl ester complex.[86] This highly stable activated ester has a higher probability of reacting with the targeted amine end group. Without using NHS, the O-acylisourea intermediate would hydrolyze within 2-3 seconds at pH~ 4.75.[87] EDX results showed that an excess of EDC resulted in higher oxygen to carbon and lowered nitrogen to carbon peak ratios in the grafted samples, when compared to bare Nylon-6,6 films. PAA with 250 kD weight average molecular weight provided best surface coverage.

The surface modification of films and fibers using inert plasma, gamma and UV radiation means has also been explored. The advantages to using irradiation techniques to induce surface functionalization on materials are: the process is clean, can be performed quickly, and requires minimal, if any, catalysts.[88, 89] Two types of radiation sources can be used; they can either be comprised of non-polymerizing plasma, or polymerizing plasma. The former technique usually results in etched type of surface modifications, while the latter process, results in free radical formation that can be used to graft monomers. Both processes are illustrated in Figure 2-11A,B.

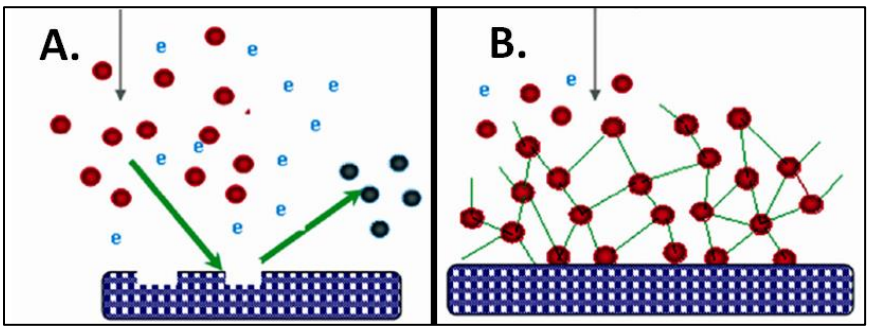

Figure 2-11 – Two types of surface reactions occurring from material exposure to: (A). non-polymerizing plasma & (B). polymerizing plasma. (A) - results in etching, or "cleaning" the material surface & (B) – results in creating binding sites (free radicals) on the surface for initiating polymerization.[88]

Gamma irradiation for inducing graft polymerization is especially versatile.[90, 91] Researchers have increased control in optimizing the graft yield on their materials by simply adjusting the dosage of radiation the materials receive. This also means that the depth of radiation exposure for the materials is also modifiable. Additionally, fiber substrates for

grafting have varied from using gel spun multifilament UHMPE [ultra high molecular weight poly(ethylene)], to knit woven Nylon-6 fabric, to carbon nanotubes, as examples.[92-95]

While it's expected that degradation can result from an overexposure to gamma treatments, there have been instances when radiation leads to other property changes without significantly distorting fiber strength. Electrospun PEDOT:PSS nanofibers were exposed to both gamma rays emitted from a Cs^{137} source at a dose rate of 69 rad/min, and X-rays from two sources (a rotating copper anode, and Cu Kα electrons).[96] The conductivity within the fibers was monitored continuously over a 15 hour period and was found to decrease for the X-ray irradiated fibers at a quicker rate than for the gamma irradiated fibers. Even though gamma radiation is of higher energy, the greater penetrative depth of the X-rays influences fiber degradation more. In a more recent study, PLLA [poly(L-lactide)] electrospun nanofibers were crosslinked in the presence of TAIC (trially isocyanurate) through gamma irradiation.[97] The degree of fiber crosslinking was found to increase as the gamma radiation dose was increased. Additionally, thermal decomposition of the fibers did not occur until an exposure of 25kGy was reached.

Overall, radiation doses and monomer concentrations for grafting onto surfaces are highly polymer dependent. There also appears to be no threshold for how much radiation or monomer can cause change. For grafting onto Nylon-6 fibers and films, radiation doses have varied from as little as $8*10^{-5}$ rad/min to ~460 rad/min.[92, 98] Monomer concentrations of acrylic acid introduced to the irradiated substrates have also varied from 10% to 20% using a variety of solvent mixtures (water, water:methanol mixture, DMF).[99] There is also agreement that usage of a metal ion inhibitor in the grafting mixture (Cu^{2+}, Fe^{3+} or Fe^{2+}) can reduce the effect of monomer homo-polymerization and increase grafting yield (Figure 2-12).[92]

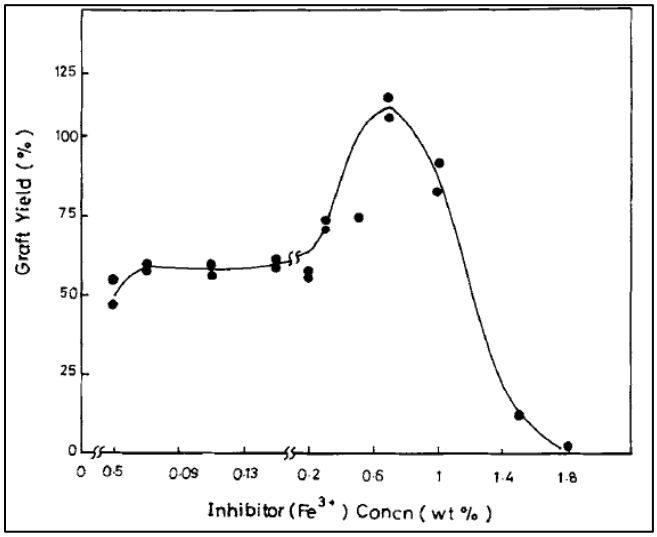

Figure 2-12 – Grafting yield trend for gamma irradiated Nylon-6 fibers (2Mrad) exposed to a (70% H_2O: 30% MeOH) solution of 10% AAc with Fe^{3+} inhibitor.[92]

3 – EXPERIMENTAL PROCEDURES

3.1 – Materials

3.1.1 – Chemicals

Nylon-6 (Mw~10kD, 3mm size pellets, CAS: 25038-54-4), Poly(Acrylic Acid) (Mw: 130kD, powder, CAS: 9007-20-9), Acrylic Acid (Anhydrous, with 180-200 ppm MEHQ [Hydroquinone Monomethyl Ether] inhibitor, CAS: 79-10-7) were purchased from Sigma-Aldrich. 1-Ethyl-3-(3-dimethylaminopropyl)carbodiimide (EDC) (powder, CAS: 1892-57-5) and *N*-hydroxysulfosuccinimide (Sulfo-NHS) (powder, CAS: 106627-54-7) were also ordered from Sigma-Aldrich. Formic acid (88%, CAS: 64-18-6), sodium hydroxide (pellet, CAS: 1310-73-2), sodium chloride (powder, CAS: 7647-14-5), and Monopotassium phosphate (KH_2PO_4) (powder, CAS: 7778-77-0) were purchased from Macron Fine Chemicals. Vacuum grease and silicone rubber resin sealants were purchased from Apiezon, and Dow Corning, respectively. Deionized water for the aerosol capture experiments was retrieved from the EMD Millipore Milli-Q Ultrapure water system.

3.1.2 – High Throughput Electrospinning Equipment

The rotating drum collector (aluminum, radius: 14cm, width: 15cm, length: 96cm) attached to the axial sliding base with Dayton motor, plexiglass needle stands, and acrylic insulation boxes (Figure 3-1) for the drum and needle stands were custom made through a collaboration between our research group and the Cornell University LASSP Machine Shop (Laboratory for Atomic and Solid State Physics) operators.

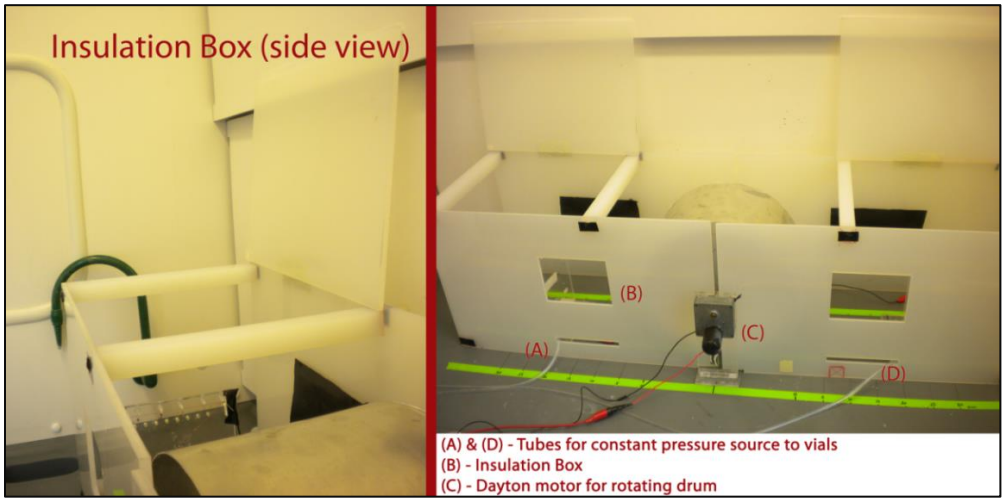

Figure 3-1 – Insulation box for Rotating Drum Large Scale Electrospinning Setup. This shows 2 box views with pressure tubes, and motor for drum rotation.

The (0-30kV) voltage supply for electrospinning and (5V) voltage supply for rotating and sliding the drum collector were provided by Gamma High Voltage Research and Heathkit. A programmable twin syringe pump was purchased from Harvard Apparatus (PHD Ultra). Syringes ranging from 10mL-30mL capacity were ordered from Terumo. Standard hub beveled needles, blunt needles with luer, and winged infusion needle sets, with 20, 22 and 25 gauges were purchased from Cadence Scientific, VWR International and Terumo, respectively. The stainless steel manifolds (with 6 – 20 gauge ports, 1 – 13 gauge side port) for dividing the solution to multiple needles were purchased from Small Parts Inc. Clearflex 60™ (ID: 1/8", OD: 1/4") and intramedic PE 90 tubing were used for solution and air transport.

3.1.3 – Simulated Breathing Apparatus (SBA) Equipment

A dual phase control large animal respirator (exhalation/inhalation) was purchased from Harvard Apparatus (SN No. B-55172).Disposable nebulizer cups (10mL maximum volume capacity), and a nebulizer compressor system (SKU: MED-HCS60004) were purchased from Medline Aeromist Plus.The conductivity meter for aerosol measurements in a 32oz. polyester waste container (wide mouth cap) was purchased from IQ Scientific Instruments.

An 8-stage stainless steel cascade impactor (Marple Series 290-8) with inline adaptor (290-I-A, with 1/4'' NPT) was acquired from Thermo Fisher Scientific. Cascade Impactor 34 mm diameter substrates were custom cut from parafilm (Pechiney Plastics "M" lab film) using the Human Ecology Building's wood shop laser cutter. Figure 3-2 shows the fit of the laser cut substrate to the impactor stage.

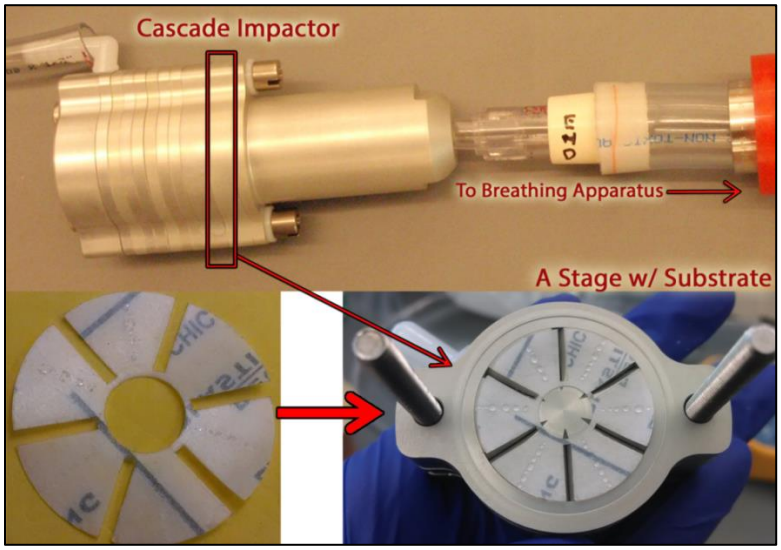

Figure 3-2 – Cascade Impactor laser cut substrates for droplet capture, and method for connection to breathing apparatus.

Various Nalgene, PVC (polyvinyl chloride), and Teflon reinforced tubing were used for apparatus assembly. Reducing couplings (3/4''x 1/2'') were used to fit tubes to ports for respirator and nebulizer with Tee-connector.

3.1.4 – Membrane Types Used & Membrane Assembly in SBA

Figure 3-3, (ID:1.25cm/OD:2cm), shows the tube end used as the filter holder for membrane testing. This tube opening with a membrane filter placed on top was connected to a stainless steel weld neck flange (Figure 3-4A and 3-4B) that held the membrane in place. On the other side of the flange, the aerosol sources (nebulizer/compressor, and respirator) were attached. A stainless steel pressure gauge (0-60 PSI) was acquired from VWR International.

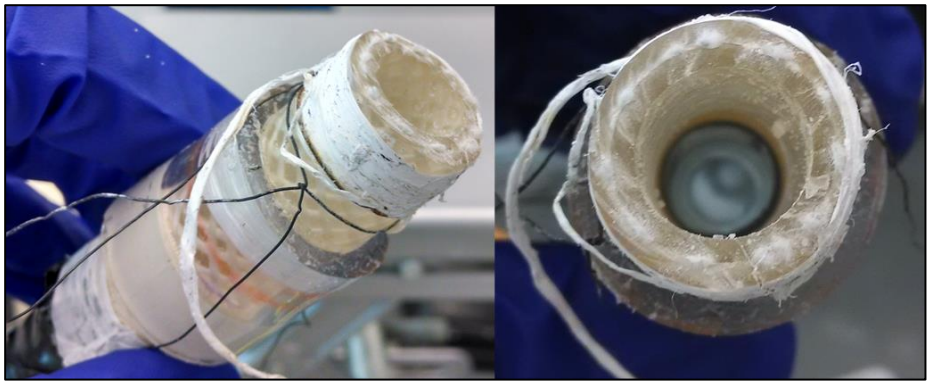

Figure 3-3 – Tube for attaching filter membrane (electrospun & controls) which will capture salt aerosol.

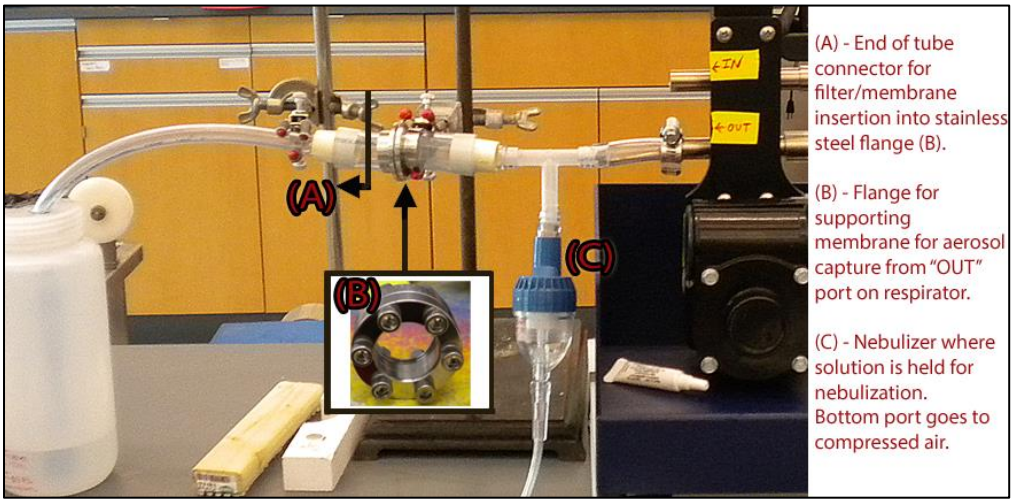

Figure 3-4 – Connection of membrane attachment tube (A) to additional supporting holder (B). Aerosol is generated in (C) and pushed towards sections (A) & (B).

Electrospun Nylon-6 membranes for aerosol capture were cut using the Cornell University Human Ecology Building machine shop laser cutter (Kern Laser System, Model HSE 52 X100). Circular (d: 3.5cm) and rectangular (2.5cm x 4cm) disks for fitting into the assembled breathing apparatus were cut. Cellulose filters (Whatman 1, 1001-042), polyester chiffon fabric, and Titan-3 Nylon syringe filters (0.2µm) by Thermo Scientific were used as membranes for aerosol capture as well. Further reinforcements used for the apparatus, in addition to silicone chemical resins, were: Super 88 vinyl electrical tape heavy duty grade (3M), 3 prong clamps (14mm – 17mm),stainless steel clamping rings (1/2'' – 1/4''), and PTFE

sealant tape. Stackable sterile polystyrene petri dishes (100mm x 15mm, Fisher Brand) were used for post aerosol capture membrane drying and storage.

3.2. – Solution Preparations, Apparatus Operations, Grafting Methods

3.2.1 – Nylon-6 Solution Preparations

Three 20 % w/w solutions of Nylon-6 in formic acid were created for a total volume of approximately 20mL per solution vial. The vials were shaken for between 15 – 20 hours using the Wrist Action Shaker (Burrell Scientific, Model 75) for until the solutions were homogenous and the Nylon-6 pellets completely dissolved. The solutions were not altered further before electrospinning.

3.2.2 – Electrospinning Apparatus Design & Operating Conditions

The rotating drum electrospinning apparatus with 12 needles set up is shown in Figure 3-5, with components of importance labeled. The drum with the insulation box is already referenced in Figure 3-1.

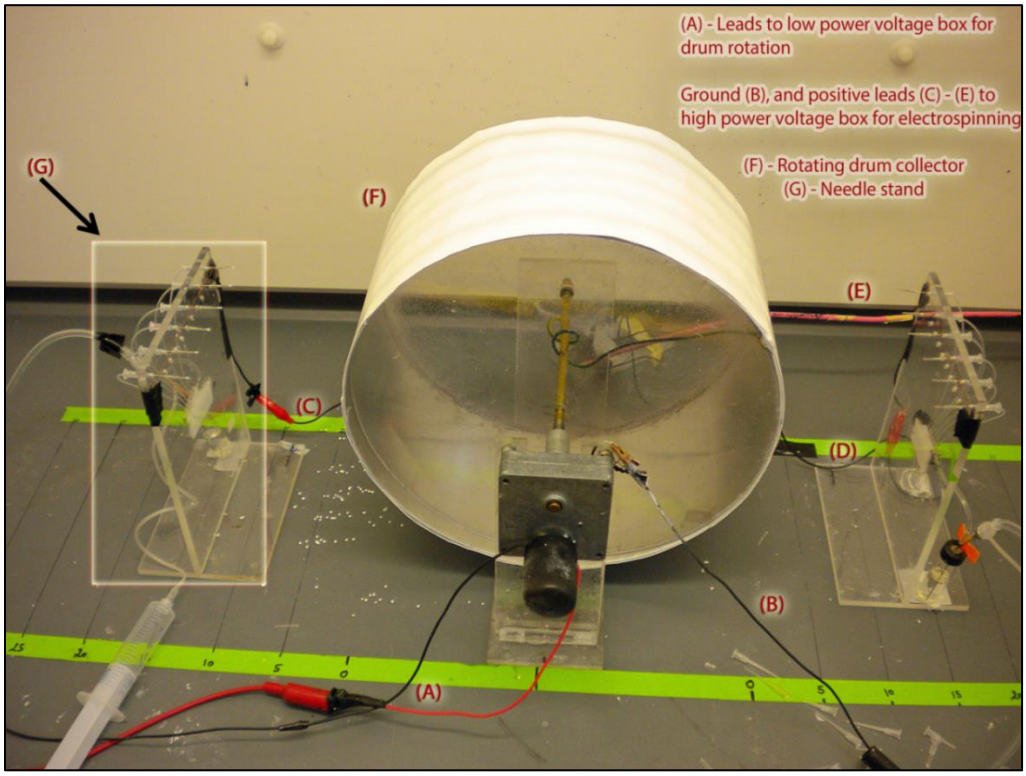

Figure 3-5 – Large scale electrospinning rotating drum setup with 2 needle stands (6 needles each) and voltage connections shown.

A close-up image of one needle stand and the solution pump vial required for solution transport are shown in Figure 3-6, with components labeled. The Nylon-6/formic acid solutions were inserted into 2 – 7ml screw cap vials with septum attachments. A vial was positioned against each needle stand and 3 needles (2 – 20 gauge, 1 – 25 gauge winged infusion) were inserted into each vial. Figure 3-6 shows that 2 of these needles do not penetrate the solution, while the last one does. The needle penetrating the solution is meant to transport the solution to the 6 - prong 22 gauge splitter, which then divides the solution to the 6 needles for electrospinning. The other two needles not immersed in the solution are meant to provide the constant pressure in the vial needed for the solution to flow into the transporting needle.

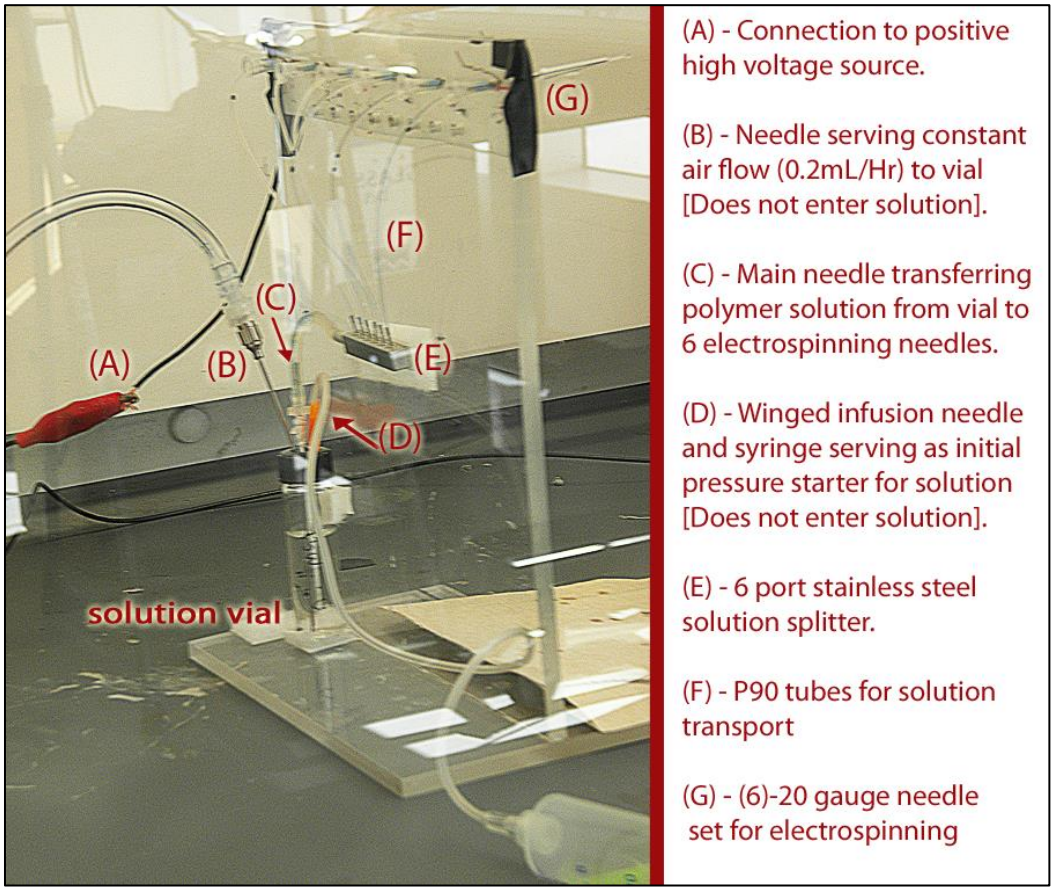

Figure 3-6 – Close-up parts of polymer-to-multi needle transport system for large scale rotating drum electrospinning. Needles (B) & (C) in solution vial show pressure mediated capillary flow of polymer to individual needle tubes. Pressure regulation is done through Needle (D).

Figure 3-7, shows a close-up of how the electrical potential required for solution to nanofiber conversion was provided to each needle. Copper wire was wrapped 2 times around each needle and gathered at the end using an alligator clip leading to the positive cable of the high voltage box. During the electrospinning process, a high voltage charge will be evenly applied to the emerging polymer solution from all 12 needles. The charged polymer will condense into fiber form and be collected on the rotating aluminum covered drum which contains the opposing charge.

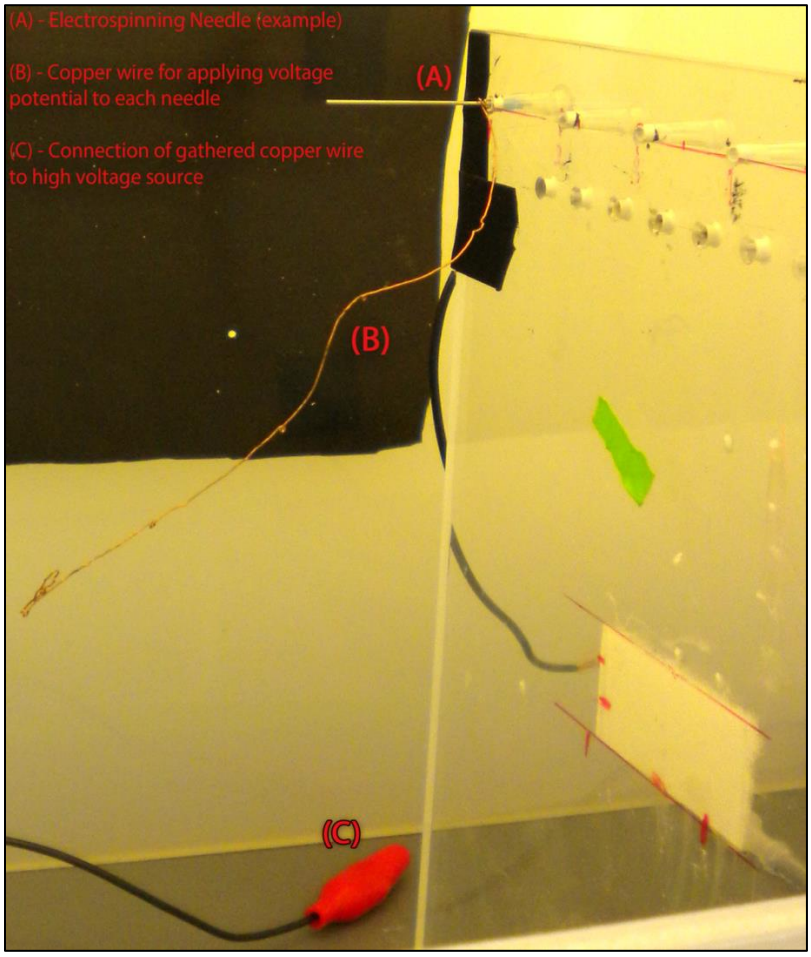

Figure 3-7 – Shows how the voltage potential to each needle in the needle stands is evenly distributed so that polymer flowing from the tips is charged. Copper wire is wrapped around each needle across and gathered at the end by alligator clip (C) to the high voltage source.

Two configurations of the rotating drum collector were used: stationary, and with axial sliding. Figure 3-8 shows the additional axial sliding capability added to the rotating drum. The axial slide is meant to move the collecting drum back and forth perpendicularly to the direction of the incoming polymer fibers. It is meant to increase uniform collector coverage and decrease processing time. The rotating drum with axial sliding mechanism was grounded with both the low power (used for rotating the drum) and high power (used for electrospinning) voltage boxes.

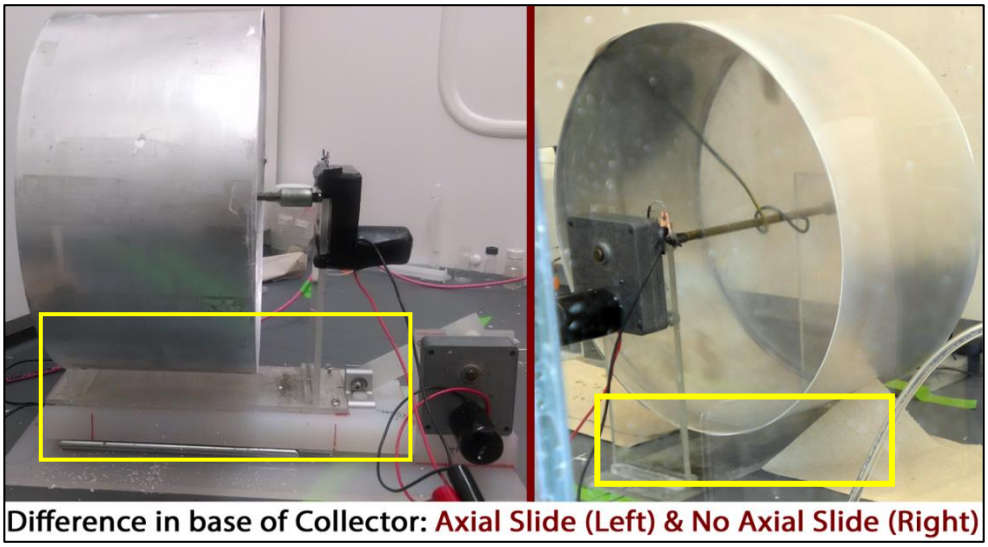

Figure 3-8 – Two different rotating drum collector configurations used for electrospinning. Left – an axial slide table mechanism (SM). Right – drum does not have axial slide motion (NSM) capability.

Three electrospun 20wt% Nylon-6 membranes, each 15cm by 96cm in size, were created to be used as standards for surface modification and aerosol testing. Table 3.1 below shows the parameters attributed to each membrane.

#	Needle Tip-to-Drum Collector Distance	Additional Drum Collector Axial Slide
1	10 CM	None
2	10 CM	Present
3	12.5 CM	Present

Table 3.1: Electrospinning parameters describing each unique Nylon-6 membrane spun.

3.2.3 – SBA Design & Operating Conditions

The assembled version of the simulated breathing apparatus is shown in Figure 3-9. Here, the apparatus is completely sealed and in operation. The respirator is connected to both the main tube line and to the nebulizer bulb via a T-connector. The “in” and “out” labels on the respirator describe which port is responsible for inhalation (in) and exhalation (out). To find the amount of aerosol particles captured on a membrane from exhaled breaths, the main line was connected here.

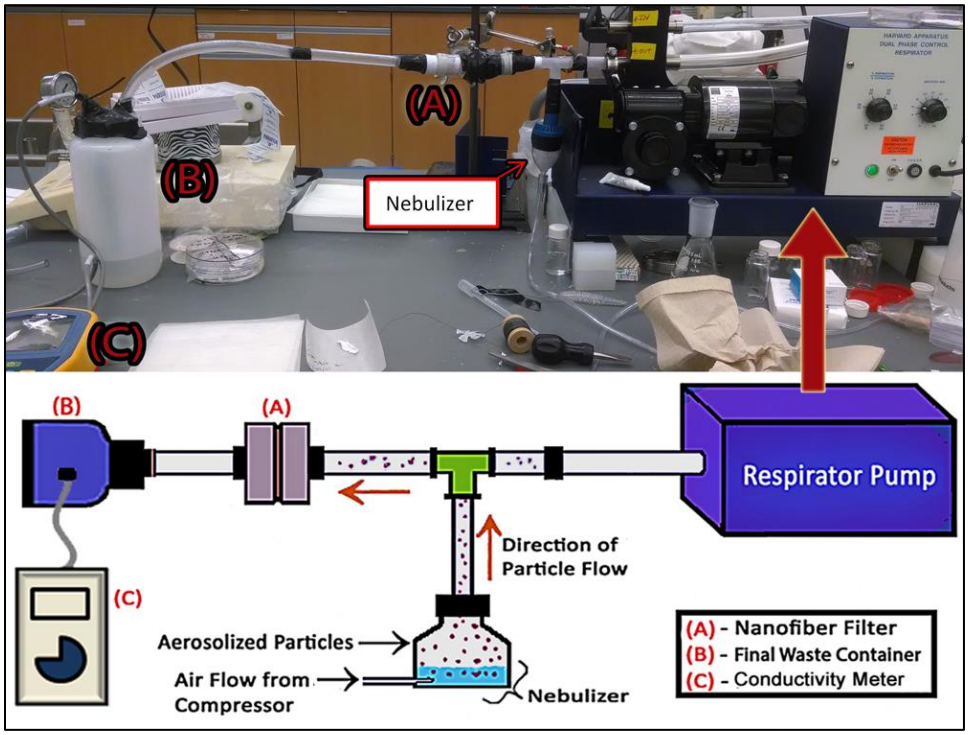

Figure 3-9 – Diagram setup of simulated breathing apparatus (SBA) with key elements: Nanofiber filter for aerosol capture, final waste container, and conductivity meter for measurements. Actual image of apparatus is shown above diagram.

The "breath inhaled" ratio to the "breath exhaled" is set using the: %Inspiration/%Expiration control. For simplicity, the ratio was kept at 50/50 during the aerosol trials. The Breaths/Min. control indicates the frequency of an inhale and exhale cycle the respirator can perform. Here, 10 – 12 breaths/minute was used. The adjusted tidal volume for air circulated was between 150-200mL. These parameters for the respirator operation were chosen to reflect respiratory rate of an adult at rest, and to maintain a pressure just low enough so that the nanofiber membranes fitted within the tube line would not rupture during aerosol capture.

The nebulizer bulb in Figure 3-9 was externally connected to a commercial compressor (not shown). This compressor provided constant air to nebulize a 1M sodium chloride (NaCl) solution in the bulb. This aerosol dispersed at pressures between ~1.5 PSI – 6.0 PSI. The salt aerosol which passed through the membrane was transported through the tube line into a waste container with deionized water (200ml). In this waste container, a

conductivity meter (Figure 3-10) measured the change in the water conductivity during the aerosol waste accumulation.

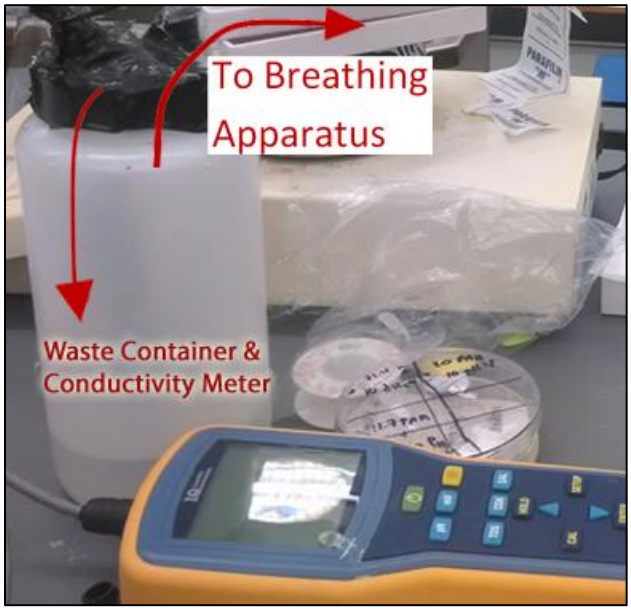

Figure 3-10 – Close-up of Waste Container containing Conductivity Meter Probe for measuring the change in aerosol waste not captured by the membranes in the Breathing Apparatus setup.

The conductivity meter was calibrated from 0.004µS to 0.008µS before each aerosol collection trial using deionized water. This was done to ensure that measurements were based on aerosol collection changes alone. It also canceled out the effects of other ionic content which could be present within the water prior to aerosol collection. Temperature compensation for the conductivity meter was set at 2%. A calibration curve for the conductivity meter against increasing NaCl was compiled from 0 ppm – 120 ppm NaCl content. This relationship between concentration and conductivity for the NaCl solutions was used to approximate the amount of salt concentration captured in the waste container, and on the membrane.

The third section of Chapter 4 discusses the type of aerosol dispersal and capture trials used for finding the amount of salt particles accumulated per membrane type. The analysis of aerosol capture results for each membrane is also discussed here.

3.2.4 – Nylon-6 Nanofiber & Acrylic Acid Grafting Preparations

3.2.4.1 – Mutual Gamma Irradiation

Strips of electrospun Nylon-6 (~2.5cm x 15cm) were cut from the original 15cm x 96cm sheet and were added to 10 % v/v solutions of acrylic acid (AA) in deionized water (pH 2.6). One strip was added per vial. These vials containing both the Nylon-6 strip and AA were mutually irradiated using a Nordion International Gamma Cell 1000 irradiator (source: Cs-137, dosage: 523 rad/min). The Nylon-6 strips were removed from solution, washed with deionized water, spread out flat to avoid folding, and dried in uncovered petri dishes for 24 hours. Samples were cut from these strips for aerosol capture tests, and for characterization.

3.2.4.2 – Amine Activation via EDC

Solutions containing 10mL KH_2PO_4/NaOH prepared buffer (pH 4.7) and ~21 mg of poly(acrylic acid) (PAA) each were prepared. Under N_2 conditions, a 1:2 ratio of EDC:NHS was added (approximately 0.009 g EDC and 0.018 g NHS). To activate the PAA polymer, these solutions containing EDC and NHS were shaken for another 30 minutes using a Burrell Wrist Action Shaker. Three Nylon-6 electrospun samples were added to the PAA/EDC/NHS mixtures, and were left to react via shaking overnight. The next day, samples were washed with distilled water, spread out flat to avoid folding, and dried in uncovered petri dishes for 24 hours. Samples were cut from these strips for aerosol capture tests, and for characterization.

3.3 – Characterization

3.3.1 – Cascade Impactor

Parafilm substrates that were laser cut to fit the cascade impactor stages for aerosol collection were weighed before assembling the impactor device. Nine substrates were used in total: 8 for each stage and 1 extra below the last stage to accumulate particles less than 0.5μm in size. Membrane samples intended for aerosol capture were assembled in the

breathing apparatus and held in place by the tube leading to the cascade impactor with inline adaptor port, Figure 3-2. The salt aerosol was continuously dispersed through the breathing apparatus for 25 minutes and was collected by the impactor stage substrates. The substrates and saturated membrane were dried overnight. They were weighed the following day to find the amount of precipitate collected.

3.3.2 – Gravimetric Weight Change Measurements

Membrane samples were weighed using a Voyager Pro balance (Ohaus, Model: VP214CN), before ($m_{Initial}$) and (m_{Final}) after aerosol exposure. Final masses of the samples were only acquired after overnight drying to ensure evaporation of all moisture. Intermediate values for the moisture gained immediately after aerosol exposure (m_{Wet}) were also obtained. Weight percent change gained before and after aerosol exposure was calculated using (Equation 3.1):

$$\%\ \boldsymbol{Weight\ Change} = \frac{\boldsymbol{m_{initial} - m_{final}}}{\boldsymbol{m_{initial}}} * \mathbf{100} \qquad \textbf{(3.1)}$$

Membrane samples that ruptured during the aerosol process were also weighed afterwards to find the potential aerosol mass lost. For membranes that were modified using PAA and AA, percent grafted calculations were also performed using Equation 3.1 as well.

3.3.3 – Field Emission Scanning Electron Microscopy (FESEM)

All electrospun Nylon-6 membrane samples used for experiments: unmodified, grafted, irradiated and those subject to aerosol capture, were mounted onto aluminum stubs (Electron Microscopy Sciences) and carbon coated using the carbon coater*(*Denton Vacuum, BTT- IV*)*prior to FESEM imaging. The flowchart (Figure 3-13) shows all of the capture membrane types examined through FESEM (LEO 1550).

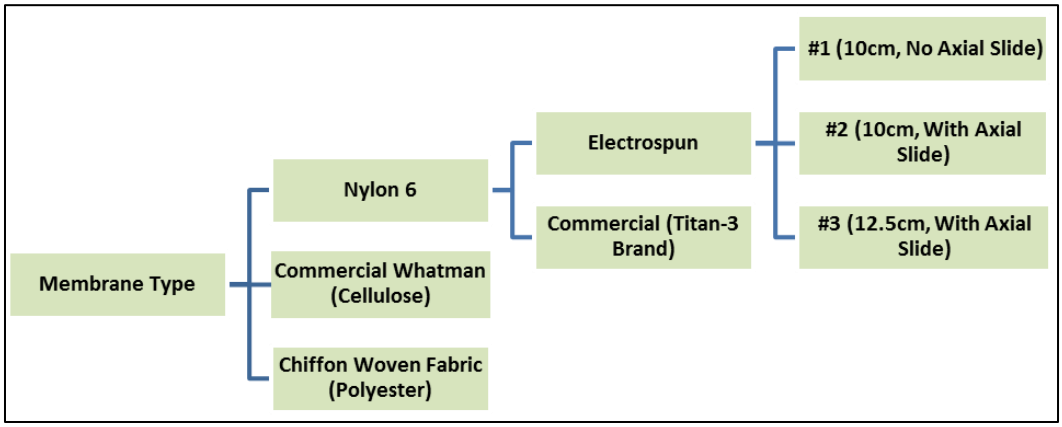

Figure 3-13 – Types of membranes exposed to aerosol salt and those analyzed in FESEM & EDX.

Samples were imaged with a LEO 1550 FESEM having an accelerating voltage of 2kV, 20um aperture, and working distance 10mm – 12mm. Multiple images at 10KX, 15KX, and 25 KX were taken per sample. At least 3 images at 25KX in different areas were used for fiber diameter, particle and pore size measurements per sample. Fifty, or more, measurements per image were acquired for fiber diameter determination.

3.3.4 – Instron© Tensile Testing

An Instron 5566 (1000N load-cell) was used to measure the tensile modulus and breaking stress and strain of the electrospun membranes. ASTM D882-12(Standard Test Method for Tensile Properties of Thin Plastic Sheeting) was used for membrane sample preparation. For all 3 Nylon-6 membranes electrospun: 1. (10CM NSM) 2. (10CM SM) 3. (12.5CM SM), 20 dumbbell-shaped samples (center length/width: 50mm/10mm) for testing were cut from random areas of the membranes. Of the 20 samples per membrane: 10 were cut from each membrane's vertical axis, and 10 from the horizontal axis, to test for strength consistency throughout (Figure 3-11). Prior to testing samples were conditioned at 23°C and 65% RH. Instron extension was performed using a strain rate of 1 mm/min.

Figure 3-11 – The two short & long end axes of the final electrospun membrane collected on the rotating drum.

3.3.5 – Porosity

Three methods for porosity measurements were performed: 1. Using capillary flow porometry, 2. Using ImageJ Feret's diameter statistics to count and measure pore sizes, 3. Using BET (Brunauer–Emmett–Teller) surface area analysis.

3.3.5.1 – Capillary Flow Porometry

One 18.4mm diameter circle of electrospun membrane from each of the three bulk spun sheets were cut. The method for analysis used was a "dry up/wet up" scheme. In other words, a dry sample was examined first, and then wetted before being examined again in a Capillary Flow Porometer (Porous Materials, Inc). The wetting fluid used was a 19.1 dynes/cm Slikwik fluid. In the dry phase, the sample is exposed to N_2 only and measurements are based on how much gas can be pushed through the sample's pores. In the wet phase, each wetted circle was placed under pressurized vacuum where N_2 gas was incrementally pumped into the sample to displace the fluid from the fiber pores. Bubble point (maximum), minimum, numerical mean (Equation 3.2), and area mean (Equation 3.3) pore diameters were calculated. N_i refers to the fraction of pores of a certain size M_i.

$$\textbf{Numerical Mean Pore Diameter} = \frac{\sum N_i M_i}{\sum N_i} \qquad \textbf{(3.2)}$$

$$\textbf{Area Mean Pore Diameter} = \frac{\sum N_i M_i^2}{\sum N_i M_i} \qquad \textbf{(3.3)}$$

3.3.5.2 – Feret's Diameter

The Feret diameter method was used to calculate the average pore diameter seen in the three bulk electrospun Nylon-6 sheets.[102, 103] Three representative FESEM images for each membrane were analyzed in Image J. To prepare the images for discriminating the "pores" from the fibers, the following process illustrated in Figure 3-12 was used.

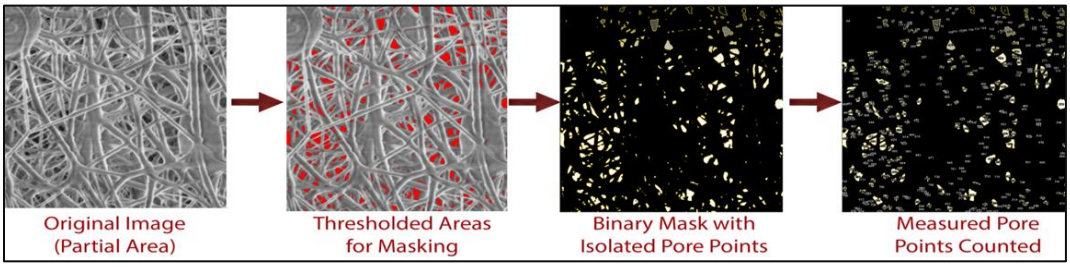

Figure 3-12 – Process for analyzing FESEM images using ImageJ to isolate and count pores between fibers.

Prior to taking measurements, each image was rescaled to reflect the accurate size range of the pores measured. A binary mask was created from a threshold scheme to isolate the pores. The binary mask was then used to find the Feret Diameter size. This process yielded between 600 – 2000 measurement points, per image. A similar procedure was performed to measure the captured salt particle sizes seen on the Nylon-6 membranes after aerosol exposure.

3.3.5.3 – BET Analysis

Brunauer–Emmett–Teller analysis was performed using a Gemini VII 2390 Surface Area Analyzer for the 3 bulk electrospun membranes to measure surface area, and pore size as well. A standard Whatman™ filter paper was used as a comparison. Samples weighing approximately 10mg – 12mg, were exposed to N_2 with relative pressure ranging from 0.005 – 0.1.

3.3.6 – Energy Dispersive X-Ray Spectroscopy (EDX)

An EDX beam and detector (Bruker) coupled to the LEO 1550 FESEM were used to observe the chemical nature of the Nylon-6 membranes prior to, and after aerosol exposure. EDX parameters were as follows: accelerating voltage – 10kV, working distance – 7 mm, magnification – 53X, scanning time – 2 minutes. Image maps of membrane areas containing significant features (such as aerosol particles, crystallized salt patterns, deformed fiber morphology) using the same EDX scanning parameters were acquired as well.

3.3.7 – Fourier Transform Infrared Spectroscopy (FTIR)

A Nicolet 560 Magna-FTIR spectrometer with ATR (attenuated total reflectance) accessory was used to find structural changes between the unmodified electrospun Nylon-6 membranes and the PAA and AA modified samples. Three spectra ranging from 4000cm^{-1}–400cm^{-1}(62 scans, resolution: 4) were taken per sample, using different areas of the membrane.

3.3.8 – Differential Scanning Calorimetry (DSC)

A DSC Q2000 (TA Instruments) was used to observe changes in the melting temperature of the electrospun Nylon-6 after PAA and AA modification. Using an automated electro-balance (Cahn 29) ~5mg of unmodified electrospun Nylon-6 from the three standard bulk spun sheets were added to a pressed Tzero pan with lid (TA Instruments). A reference, an empty pan and lid, was compared to the sample in the DSC. The samples and reference were heated in a temperature ramp from 20℃ to 300℃ at a rate of 10°/min. They were held at isothermal for 1 minute, and then cooled back down to 20℃ at the same rate.

Using Equation 3.4, the degree of crystallinity of the unmodified and modified samples was calculated. The heat of enthalpy (ΔH_m) for each sample was calculated by integrating the area under the melting temperature (T_m) curve using TA Instruments Universal Analysis software. Here, ΔH^o_f, represents an average value of the theoretical heat

of enthalpy for 100% α-crystalline Nylon-6 (~215℃). This average was calculated from the commonly cited literature values 190℃ & 240℃.[104-107]

$$\% \textbf{ Crystallinity} = \frac{\Delta \mathbf{H_m}}{\Delta \mathbf{H_f^o}} * \mathbf{100} \qquad \textbf{(3.4)}$$

3.3.9 – Wettability

Using the wettability test (KSV Sigma 700), rectangular samples of unmodified electrospun and grafted Nylon-6 samples were suspended over a distilled water container and dipped in at 10mm/min. One mm of the sample's edge was immersed in the water. As moisture accumulated throughout the sample through capillary action, the mass increase was plotted versus time elapsed (10 minutes). All samples were cut into 3cm x 5cm rectangles for testing. Small fish hooks were attached to the bottom of the samples to ensure that the thin edge of the nanofiber membranes penetrated the water surface vertically.

4 – RESULTS & DISCUSSION

4.1 – Large Scale Electrospun Nylon-6 Nanofiber Membrane Optimizations & Characterizations

In this section, the morphological differences in nanofiber membranes electrospun from using a large-scale rotating drum collector apparatus versus a small-scale stationary collector apparatus are discussed. Advantages of using a large scale setup are detailed. The characterization results (morphological, tensile, crystalline, pore/surface area, wetting properties) of three large scale spun Nylon-6 membranes, which will be further used in surface modification and aerosol capture studies, are also discussed.

4.1.1 – Electrospinning Results & Observed Differences from Using Large Rotating Drum Collector Vs. Small Stationary Collector

The differences in morphology of electrospun material created from using the rotating drum collector, and the material created by using small scale rectangular collectors, can be seen in Figure 4.1-1A,B. In the small scale electrospinning set up (Figure 4.1-2), the size of the collector is limited by the dimensions of the insulating box, and fibers are produced from one single needle source. Usually the collector is made smaller than the size of the insulating box to maximize the amount of electrospun material accumulated in the center of the collector.

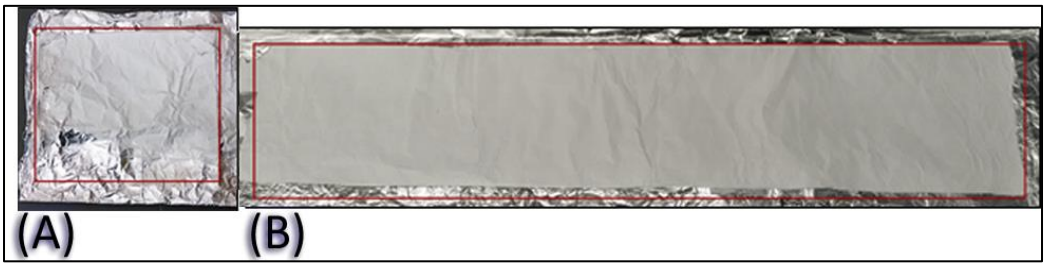

Figure 4.1-1 – Relative sizes of Nylon-6 electrospun membranes using Small Scale (A) & Large Scale (B) spinning setups. The sizes of material able to be spun are significantly different [See Red Outlines for A: 15cm x 15cm & B: 15cm x 96cm].

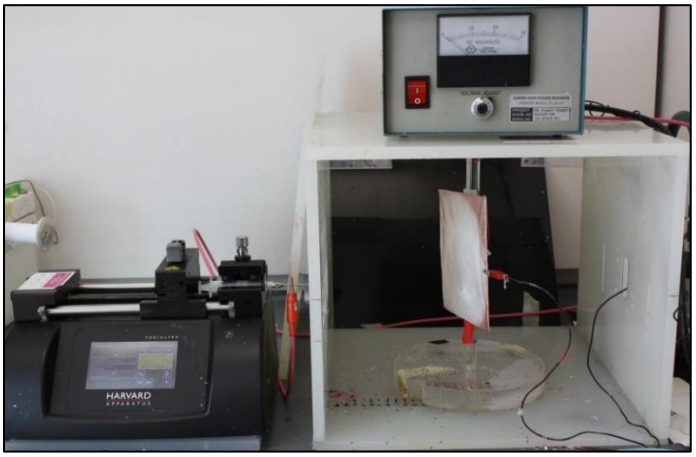

Figure 4.1-2 – Small Scale electrospinning setup with 1 needle source and a rectangular stationary collector.

Furthermore, because large quantities of electrospun material cannot be created at once, producing samples with the small scale electrospinning set up introduces an additional variable in subsequent experiments based on non-uniformity of material created at different times. For the creation of large quantities of uniformly distributed electrospun fibers, with statistical similar properties throughout the membrane, the use of a rotating drum collector with optimized needle orientation and distance placement is recommended (Figure 3-5).

In order to find the "optimal" electrospinning conditions, as noted by Li and Wang, for Nylon-6 in 98% formic acid, various voltages, distances and weight percent solution concentrations were experimented with using small scale collectors before scaling up the process.[33] Figure 4.1-3 shows the morphology of different Nylon-6 nanofiber membranes electrospun at low voltage and two distances. All membranes show considerable beading, irregular fiber diameters, and broken fibrils. Since the flow rate used for these processes led considerable polymer dripping at the needle tip, this meant that the applied voltage difference between the collector and needle was not enough to induce continuous fiber formation. Thus, beads, as well as irregular fiber lengths developed.

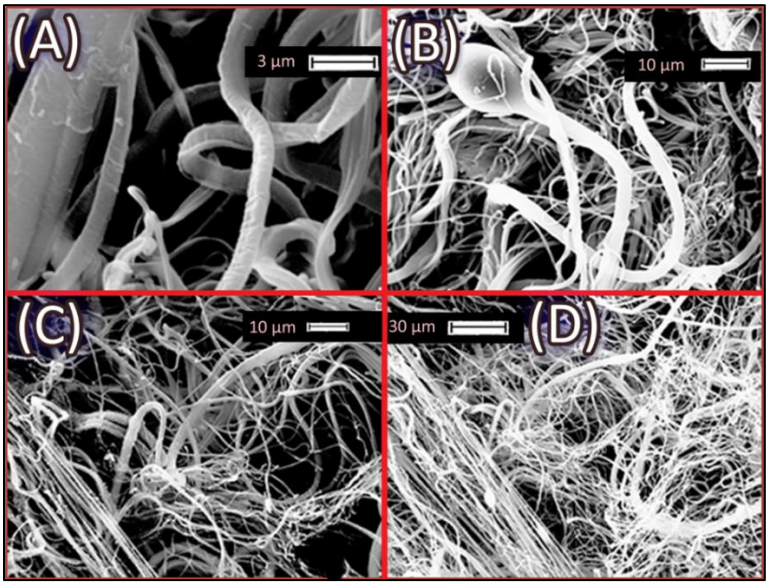

Figure 4.1-3 – 15 wt% electrospun Nylon-6 membranes using the small-scale stationary collector setup at: 17.25KV & 10cm needle-to-collector distance (A & B), and 17.25Kv & 12.5cm distance (C & D). The flow rate, which also dripped, was at 0.02 mL/Hr.

After optimization, we found that, for the small scale setup, the minimal optimal conditions for creating a membrane with fibers containing statistically similar diameters, without beads, and other imperfections on the fiber surface are: 15wt% Nylon-6 in 98% formic acid, 12 cm needle-to-collector distance, and 20 KV applied voltage.

Figure 4.1-4, and its corresponding Table 4.1.1, shows the measured fiber diameter differences from electrospinning 15wt%, 18wt% and 22wt% nanofiber membranes using the small scale setup. As expected, increased polymer solution concentration results in increased fiber diameter.

Concentration (Wt %)	Fiber Diameter (nm)	Error (nm)	N (# Sampled)
15%	91.33	5.78	61
18%	204.55	6.86	86
22%	238.86	12.50	91

Table 4.1.1 – Small scale electrospinning fiber diameters of membranes spun from 3 different concentrations.

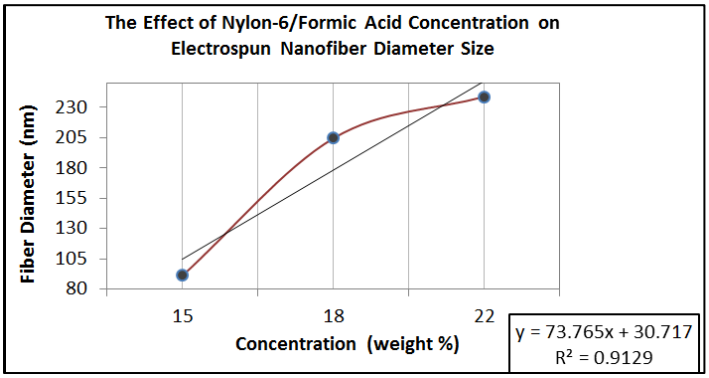

Figure 4.1-4 – Nylon-6 concentration effect on electrospun nanofiber diameter size.

Figure 4.1-5 shows the distribution of fiber diameters produced from the 15wt% and 22wt% solutions. FESEM images of their respective membrane morphologies are also shown. Although the fibers produced from these two concentrations are uniform, and are without morphological aberrations, the sample membranes were quite small. Because of this, they were unable to be used for cutting out multiple filter samples for aerosol testing in the assembled Simulated Breathing Apparatus (hereafter, abbreviated SBA).

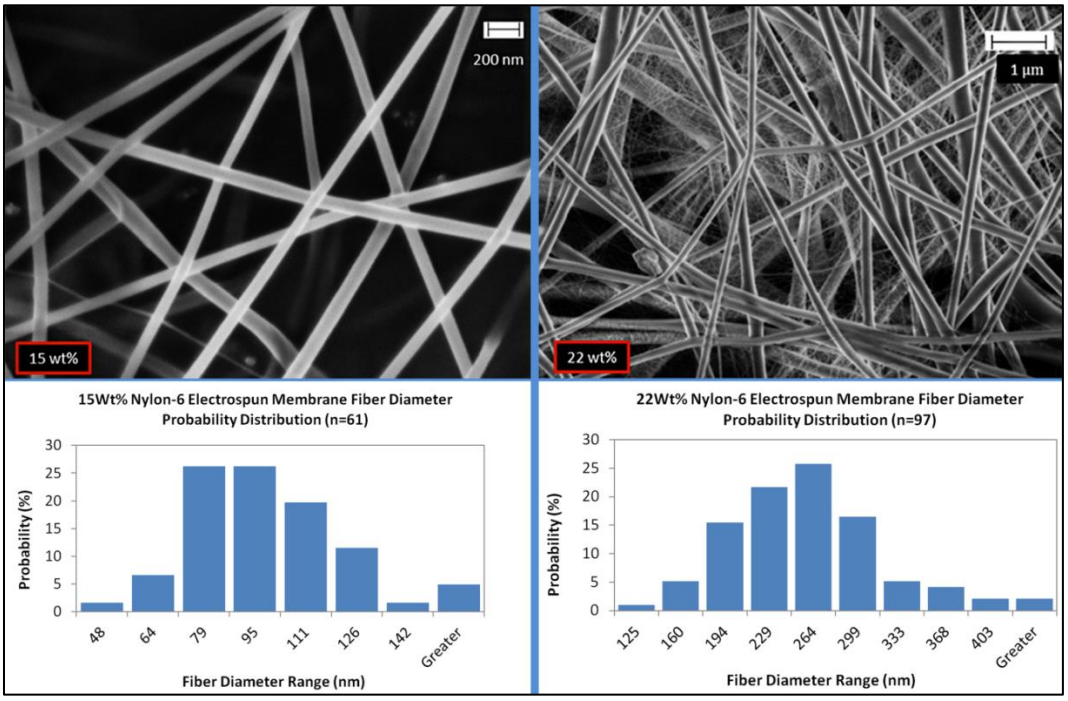

Figure 4.1-5 – Nylon-6 electrospun membranes at 15wt% & 22wt% with probability distributions for (n) measurements.

Since multiple sources have concluded that nanofiber membranes can capture particles in the "most difficult to capture size range", roughly between 100nm – 1µm, when fiber diameters are smaller than 500nm, the electrospinning process for creating fiber uniform membranes with fiber diameters within the 100nm – 200nm range needed further modifications.[39-42]

Thus, a rotating drum collector was optimized so that large uniform sheets of Nylon-6 nanofibers, with the desired fiber diameter ranges could be produced. Electrospinning large uniform sheets in this manner eliminated the variability which using the smaller electrospinning setup initially introduced. From these sheets, smaller filter membranes (5cm circles) for aerosol loading were laser cut.

4.1.2 – Electrospinning Results After Modifying the Large Scale Rotating Drum Collector (Containing the Electrospinnning Area Using an Insulating Box & Adding an Axial Sliding Mechanism)

After the assembly and optimization of the large rotating drum collector with 12 needle electrospinning, the effectiveness of using an insulating box to contain the voltage potential between the needle sets and collector was examined. Figures 3-1 and Figure 3-5 from Chapter 3, show the rotating drum with and without the insulation box.

Without external insulation, excessive static charges appear to accumulate on the surrounding surfaces of the electrospinning environment and cause the charged polymer fibers to form haphazardly in many directions. This may be also due to the high conductivity of the formic acid solution, the "leaky" dielectric, which allows the Nylon-6 to spin easily, but also increases the chance of charged fibers attracting to many surfaces when the voltage is high.

As a result, without the external insulator, the Nylon-6 membranes formed have inconsistent diameter sizes, a variety of round and flat ribbon morphologies, and excessive

split fiber entanglements, Figure 4.1-6A through Figure 4.1-6C. The morphologies of these membranes mimic those seen for the small scale setup when too low of a voltage is used.

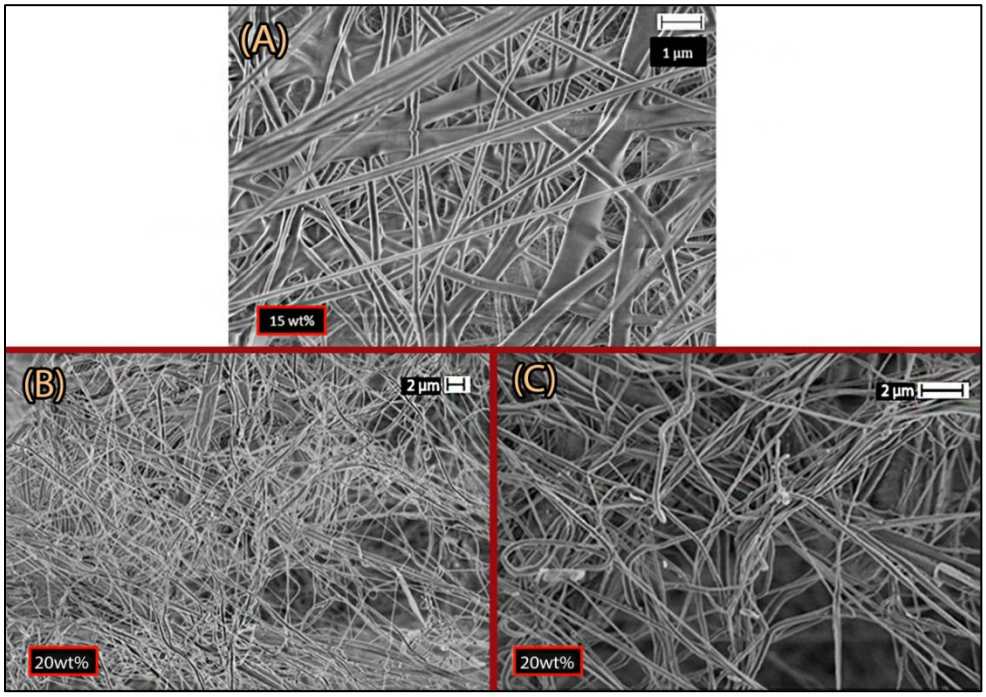

Figure 4.1-6 – Undesired membrane morphologies (flat, broken, irregular fibers) of two concentrations (15wt% [A,B] and 20wt% [C]) of Nylon-6 electrospun using the large scale rotating drum setup without charge insulation coverage.

Alternatively, using the insulation box facilitates the creation of nanofibers which have more consistent fiber diameters without entanglements, seen in Figure 4.1-7 for 15wt% and 20wt% solutions. This is because the voltage potential between the collector and charged needles is isolated from the external environment. Fibers are able to be directed towards the collector because the electric field between the needles and large collector is confined to just only this area. The insulation box prevents surrounding areas (metal fixtures in fume hoods, debris/dirt…etc.) near the charged needles and the grounded rotating collector from acquiring static charge, and possibly influencing the trajectory of the spun fibers.

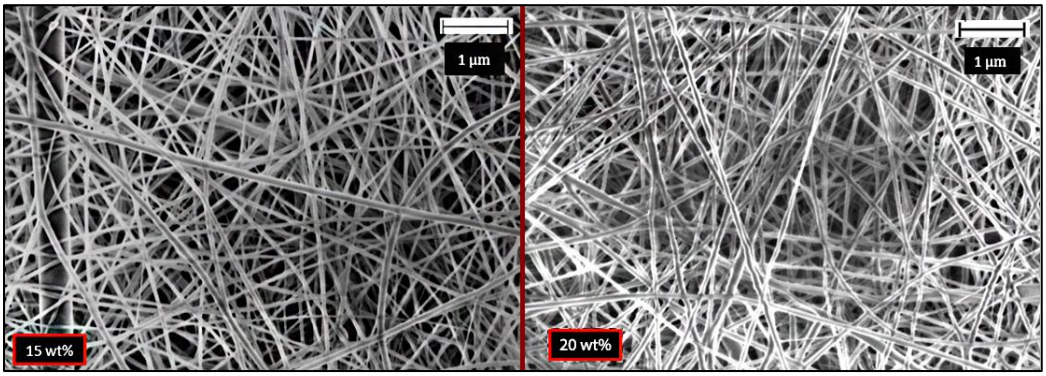

Figure 4.1-7 – FESEM images of membranes from Nylon-6 electrospun at two concentrations (15wt% and 20wt%) using the large scale rotating drum setup with charge insulation.

After using the insulated rotating drum collector, fiber diameters also decreased for the same weight percent concentrations spun as for the small scale set up. The fiber diameter results of 15wt% Nylon-6 spun on the rotating drum and stationary collectors are shown in Table 4.1.2. Needle tip-to-collector distance and voltage applied were kept the same. The decrease in nanofiber diameter is due to the additional stretch that polymer fibers from the Taylor Cone jet undergo as they are deposited onto the large rotating drum.[145, 146] As the drum rotates, the fibers are pulled throughout the length of the drum's surface and additional solvent is given more time evaporate per rotation. This process results in a fiber membrane that takes longer to cover the entire length of the collector, but one that gives thinner fibers.

One way to measure if this is what truly occurs during spinning onto the rotating collector is to observe, through a high speed camera, how the Taylor Cone jet changes shape as the rotating drum makes one revolution. Since the whipping jet is not constantly attracted to a flat collector surface, the curvature of the collector drum should influence an observable change in the Taylor Cone jet, similar to Reneker's experiment showing differences in jet stability for a wedge collector.[147] This experiment showed that changing distance from the needle-tip to collector dramatically effected the Taylor Cone shape, and led to differences in deposited membrane morphology and individual fiber diameters.

Fibers deposited onto a stationary collector do not undergo this stretching process as the needle-to-collector distance is always fixed at any given time.

Nylon-6 Conc.	Rotating Drum Collector	Stationary Collector
15 wt%	71.60 nm ± 5.39 nm	91.33 nm ± 5.78 nm

Table 4.1.2 – Decrease in Nylon-6 nanofiber average diameter after electrospinning the same polymer solution concentration on two different collector setups: rotating drum, and stationary (N = 61).

Ultimately, for creating Nylon-6 nanofibers with diameters between 100nm and 200nm, the final electrospinning conditions were: 20wt% Nylon-6 in 98% formic acid, 10 cm needle to collector distance, and 27 KV applied voltage. At a distance of 10 cm from the rotating drum, an increased voltage was necessary to "stretch" the Taylor cone fibers formed from the needle tip onto the collector.

This higher applied voltage also prevented dripping at the needle tips. To complete the optimization process, the rotating drum was coupled to an additional motor and slide table which allowed the drum to axially slide back and forth, Figure 3-8.

Using this newly configured rotating drum with axial sliding, the coverage of the large membranes was more uniform, and did not contain "-bands-" of uncovered areas as previously seen (Figure 4.1-8). Figure 4.1-1B, shows one of the final Nylon-6 membrane standards used for aerosol capture and surface modification created using the rotating drum-coupled-axial sliding electrospinning configuration.

Figure 4.1-8 – Nylon-6 electrospun membrane produced from large scale rotating drum setup without final axial sliding table. Striped bands on the collector show inhomogeneity of fibers deposited.

Though the non-axial sliding configuration could produce membranes which did not contain bands, this was only possible if during the spinning process, the needle stands were moved perpendicularly from the drum every 30 – 45 minutes. Offsetting the needle stands in this manner redistributed the location of where the charged fibers could become attracted to the available metallic surfaces on the collector. With the axial sliding configuration, moving the stands is not necessary, and further eliminates a manual step in producing the large nanofiber membranes.

Three standard membranes of the same Nylon-6 concentration were produced to measure their filter capabilities within the assembled SBA (Simulated Breathing Apparatus). Their differences in measured fiber diameter are shown in, Table 4.1.3. Morphologically, all 3 standard membranes all appear to contain evenly distributed smooth, cylindrical fibers, without broken filaments, or spherical beads (Figure 4.1-9). The differences in the fiber diameters were statistically significant. Fibers spun with the shortest needle to collector distance and no sliding mechanism (#1 - 10CM NSM) were largest. Adding the sliding mechanism (#2 - 10CM SM) decreased the diameter by about 20nm, and increasing the needle to collector distance to 12cm (#3 - 12.5CM SM) further decreased the diameter by another 20nm.

Membrane	Needle-to-Collector Distance	Electrospinning Configuration	Fiber Diameter (nm)	95% Conf. Error (nm)
1	10 CM	NSM	140.37	13.21
2	10 CM	w/ SM	120.11	6.41
3	12.5 CM	w/ SM	98.92	5.53

Table 4.1.3 – Final 3 Nylon-6 (20wt%) electrospun standard membranes produced on the rotating drum at 2 distances (10 cm & 12.5cm) with 2 drum spinning configurations (NSM – No Sliding Mechanism, w/ SM – with Sliding Mechanism). These membranes will be used for aerosol capture and surface grafting experiments.

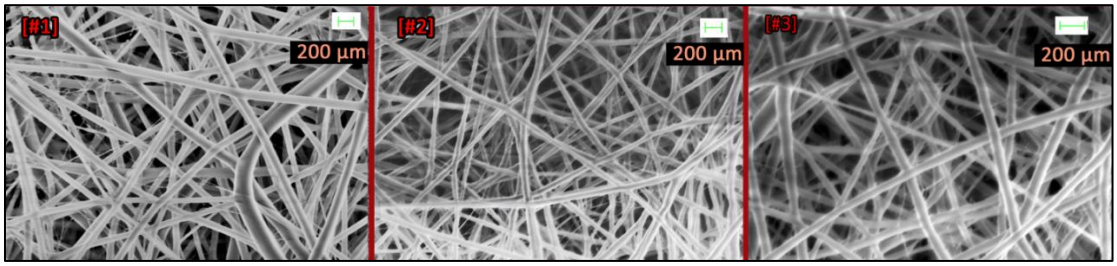

Figure 4.1-9 – FESEM images of final 3 electrospun membranes used for aerosol capture & surface modification experiments. Nylo-6 fiber membrane images [#1] – [#3] correspond to the types of membranes listed in Table 4.

4.1.3 – Characterizations of Electrospun Nanofiber Membranes Produced On Large Scale Modified Rotating Drum

4.1.3.1 – Tensile Strength & Macroscopic Observations

To determine the extent to which the 3 standard Nylon-6 nanofiber membranes (Figure 4.1-9) produced by rotating drum were uniformly distributed, random areas in both the horizontal and vertical axes of each membrane (diagram in Figure 3-11) were sampled for their tensile stress and strain properties. Figure 4.1-10, shows the breaking modulus results of Instron© tensile tension testing for the 3 (15cm by 96 cm) membranes electrospun using the different configurations listed in Table 4.1.3.

Figure 1 in the Appendix shows the raw stress versus strain horizontal and vertical axes data of 10 samples each from Membranes [#1] – [#3] (10CM NSM, 10CM SM, and 12.5CM SM, respectively). Table 4.1-11 shows the average corresponding breaking strain (mm/mm) and breaking stress (MPa) of each membrane in both the horizontal and vertical axes.

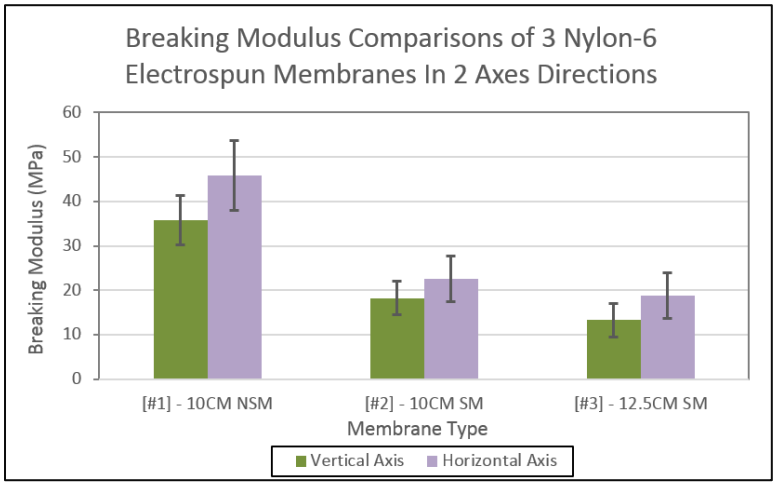

Figure 4.1-10 – Average breaking moduli for all three electrospun Nylon-6 membranes for both horizontal and vertical axes directions.

[#1] 10CM NSM	Avg. Strain @ Break (mm/mm)	Avg Stress @ Break (MPa)	Avg Break Modulus [N=10 each] (MPa)
Vertical Axis	0.13 ± 0.03	4.28 ± 0.65	35.74 ± 5.61
Horizontal Axis	0.13 ± 0.03	5.74 ± 1.06	45.90 ± 7.84

[#2] 10CM SM	Avg. Strain @ Break (mm/mm)	Avg Stress @ Break (MPa)	Avg Break Modulus [N=10 each] (MPa)
Vertical Axis	0.06 ± 0.03	1.15 ± 0.40	18.26 ± 3.70
Horizontal Axis	0.11 ± 0.03	2.52 ± 0.84	22.63 ± 5.15

[#3] 12.5CM SM	Avg. Strain @ Break (mm/mm)	Avg Stress @ Break (MPa)	Avg Break Modulus [N=10 each] (MPa)
Vertical Axis	0.06 ± 0.02	0.64 ± 0.10	13.27 ± 3.76
Horizontal Axis	0.11 ± 0.26	2.15 ± 1.07	18.87 ± 5.10

Figure 4.1-11 – Average stress and strain at break for the 3 standard electrospun Nylon-6 membranes compiled from Figure 1 in the Appendix. Average break modulus actual values are shown (these values are plotted in Figure 4.1-10) and differ from Young's Modulus[Θ].

The addition of the sliding mechanism to the rotating drum collector decreases the fiber mat tensile strength (measured by elastic modulus here) by roughly half in both the

[Θ] Young's Modulus calculates the stress/strain ratio of the textile membrane after 2% stretching (this region is still linear). Breaking Modulus is the final stress/strain ratio when the membrane breaks after full stretch.

horizontal and vertical directions. This is because the fiber membranes, even though they are spun using the same collector distance (as in [#1] and [#2]), are experiencing different interactions as they deposit on the collector. Membrane #2 was made using the axial slide. The drum is sliding back and forth which causes the electric field between the needle jets to shift laterally with the shifting drum. It's possible that this sideways shifting can further cause the individual spinning jets from the needles to elongate the fibers deposited, and cause a more even distribution of the fibers collected on the whole collector.

[#1] had no shifting drum collector, and was created by offsetting the needle stands on opposite ends of the drum so that deposited fibers would cover the entire drum length. The fibers produced from this method cover the collector in a denser way contributing to a higher weight shown in Figure 4.1-14 (red). More fiber deposition would lead to higher elastic strength shown in Figure 4.1-10.

As seen in Figure 4.1-11, each membrane's fractional strain in both the horizontal and vertical directions is similar. The maximum average stress each membrane experiences before breaking differs; [#1] ~4 - 5MPa, [#2] ~1 - 2MPa, and [#3] ~0.6 - 2MPa. Though this is due to the various collector configurations, maximum stress for all membranes in the Horizontal Axis direction is the highest. This means that there is slight machine directionality to the membranes created on the drum fibers collected on the rotating drum.

Also, since stress and strain values for the vertical axis are more similar, this implies that the membranes produced are elastic. Here, plastic deformation occurs for a period before final fracture which is not characteristic of brittle materials such as glass or concrete.[108] In general, all of the electrospun membranes exhibit a ductile character, which is expected for textiles, polymer plastics, and rubbers.[109] The stress/strain curves of all three membranes in both the horizontal and vertical directions are shown in the Appendix Figure 1.

[#1] - 10CM NSM shows the most elastic and strength with average break modulus at 35MPa - 45MPa. Also, increasing the distance of the needle to the collector [#3] - 12.5CM SM influences a further decrease in average break modulus. The sliding mechanism coupled to the rotating drum does have an effect of lowering the tensile properties of the membranes in both directions.

Elastic (Young's) Moduli for materials describe the maximum stress a material can withstand before undergoing non-elastic failure. In the tensile stress-strain plots above, this can be described as the Hookean linear region, which is typically seen for up to 2% of stretching in textile fibers.[110, 111] Young's Modulus can be calculated using Equation 4.1.1:

$$\mathbf{E} = \frac{\boldsymbol{\sigma}}{\boldsymbol{\varepsilon}} \qquad \textbf{(4.1.1)}$$

where σ and ε refer to the tensile stress (MPa), and the tensile fractional strain in (mm/mm) sustained, respectively. For all three membranes, the elastic moduli of both directional axes were averaged and compared using a hypothesis z-test for comparing the equivalence for two means.

This process was done to test if the average moduli from the horizontal and vertical axes of each membrane were statistically similar. Then conclusions as to whether each membrane electrospun was uniform in these 2 directions could be made. In other words, if for instance, the average elastic vertical modulus for [#1]-10CM NSM is found to be similar to its average elastic horizontal modulus, also from [#1]-10CM NSM, then we can conclude that the overall electrospun membrane [#1]-10CM NSM has uniform fiber coverage in both horizontal and vertical directions.

Figure 4.1-12 shows that the calculated 95% confidence z-test statistic for the two axes of each membrane fell within the "no rejection" range (green), and therefore, their Young's Moduli could be averaged to one value (orange). If the hypothesis that the average

moduli was: “not rejected”, then the axes averages could then be combined. Then, a clearer difference between the overall individual elastic strength of each membrane can be seen.

For both the initial deformation up to 2%, and deformation up to break, the membranes were found to be uniformly electrospun in both the horizontal and vertical directions using all of the rotating drum collector configurations.

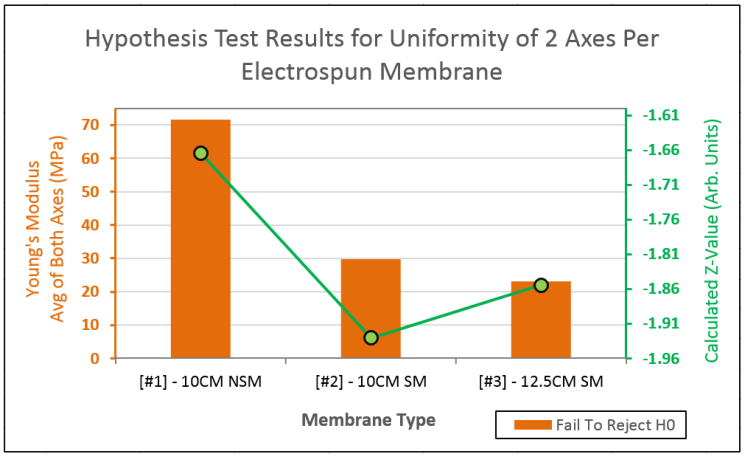

Figure 4.1-12 – The average Young Modulus values of both the horizontal and vertical axes within each electrospun membrane shown in orange. The green line represents each z-test statistic value calculated to determine if the horizontal and vertical axes were significantly different. Since the values fell between [-1.96,+1.96 – the 95% confidence range for testing] the horizontal and vertical axes were not found to be statistically different. (Table 2 in the Appendix shows Individual Axis Modulus Values & Hypotheses)

As mentioned before, differences in the moduli between each membrane are attributed to the different drum configurations of the electrospinning setup (even though the moduli within each membrane are found to be similar). The highest modulus for the membrane spun at 10cm without axial sliding is expected, even though the 2 axes have different max stress loads before break. This is because, during the deposition of fibers onto the spinning drum, the fibers do not undergo additional stretching, as they would if the drum were to slide back and forth.

Thus, while the axial sliding of the drum contributes to more uniformly distributed fibers covering larger surface areas of the collector; thinner fibers resulting from this process

lead to membranes with observable differences in fiber translucency and density, Figure 4.1-13 and Figure 4.1-14, respectively.

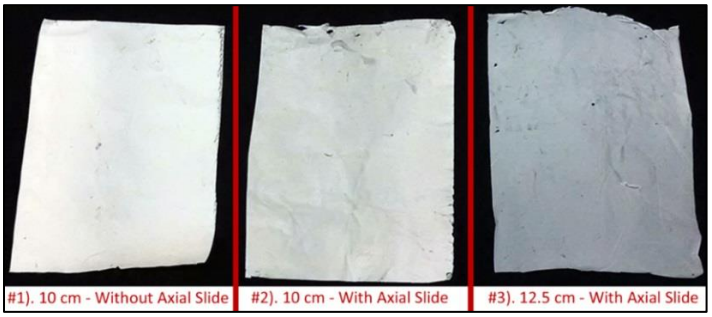

Figure 4.1-13 – Translucency level of the 3 standard membranes.

Fibers collected using the axial slide from a large distance will be the most translucent, show reduced modulus, the least fiber density [#3]. Three sample squares (2cm by 4cm) were cut from each membrane and weighed. Their respective densities are seen in Figure 4.1-14*. The membrane spun without the axial motion clearly has most fiber distribution.

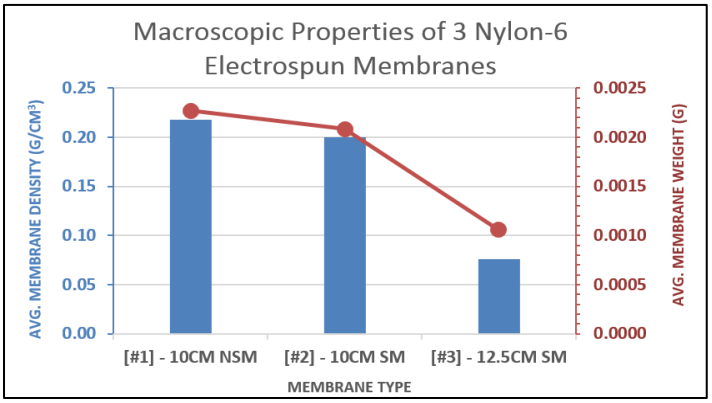

Figure 4.1-14 - Differences in weight (red) and calculated fiber membrane density (blue) for the 3 membranes. (Table 1 in the Appendix shows individual membrane densities & weights)

* The thickness of the membranes was estimated to be between 9µm - 13µm after measurements performed in the FESEM with a stage tilted mounted sample.

The combined effects of using the axial sliding mechanism during spinning will lead to decreased fiber distribution, [#2] & [#3]. Increased needle to collector distance will lead to the deposition of thinner fibers, [#3].

When placed over black fabric under incandescent light, the difference in nanofiber density for each membrane can be qualitatively seen. [#3] has the highest translucency of the three, which overall corresponds to the lowest measured density. Qualitatively, [#1] also shows a comparable coverage with [#2]. This suggests that the fibers in these nonwovens were distributed in a more interlocking manner, and overall thinner, than those fibers in [#3]. Physically, [#3] tore easily and there was also fiber loss from the membrane itself during spinning. The decrease in weight suggests that not all fibers were deposited onto the collector for the increased distance. This can be seen from the tiny holes around the membrane edge which occurred even after delicate handling, and also correspond with its low stress handling capability from Figure 4.1-11.

[#3] also performed the poorest under aerosol testing due to its inability to withstand the pressure cycles of the simulated breathing apparatus. Further results of the performance of all three nanofiber membranes during aerosol exposure will be discussed in Chapter 4.3. This poor performance overall resulted in the membrane rupturing during the aerosol loading cycle and allowing the most aerosol to pass into the waste collector.

Ultimately, for creating large uniform fiber membranes, using the rotating drum collector with or without the axial sliding mechanism is recommended. However, there is a processing disadvantage to contend with if no axial sliding is to be used with the rotating drum. Though using this method can potentially lead to more elastic, and higher strength fiber membranes, it requires extensive supervision (~ every 30-45 minutes) for creating a uniform membrane (a process which can last up to 4 hours).

4.1.3.2 – Porosity Measurements Using: Capillary Flow Porometry and Feret's Diameter

Capillary flow porometry uses a wetting liquid to determine how large the pores in a membrane, or fabric, are. The sample is loaded into the porometer, saturated with a wetting fluid of specific surface tension (here, 19.1dynes/cm SilWick^{TM} fluid was used), and pressurized under vacuum. The pore sizes of the membrane are measured by how much of the wetting fluid can be pushed through the membrane by a specific pressure of N_2 gas. The results of the capillary flow porometry analysis are shown in Figure 4.1-15.

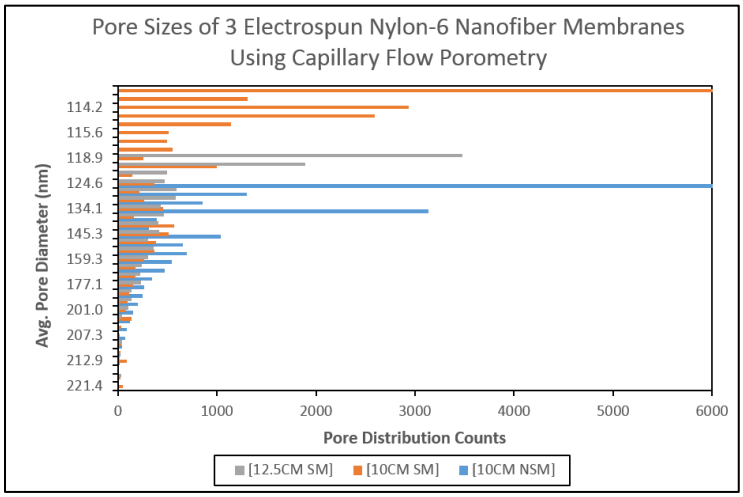

Figure 4.1-15 – Frequency histogram of average pore diameters for 3 standard membranes found using capillary flow porometry.

Porometer Area Mean Pore Diameter Ranges		
107.7 nm,	122.6 nm,	104.6 nm
10CM NSM,	10CM SM,	12.5CM SM

Figure 4.1-16 – Area mean pore diameters calculated (using Equation 3.3) from Capillary Flow Porometry pore diameter results. These values are weighted towards the larger pores in the membrane.

As shown, the majority of pore sizes calculated for all three membranes fall between 104nm – 122nm. The average of pore size diameter for all three membranes is shown in

Figure 4.1-16, with the lowest pore diameter seen for Membrane #3, as expected. Small fiber diameters will result in small pore sizes. Membrane #3 spun at the largest distance from the collector at 12.5cm, has the smallest diameter (104.6 nm). This makes sense because more fibers are deposited per unit area of the collector during the spinning process, even though these fibers are thinner, and lighter than those of the other 2 membranes.

Figure 4.1-17 shows a comparison between the nanofiber diameter and the porometer calculated pore diameters. Membrane #3 fiber diameters and pore sizes are almost equivalent, showing the increased fiber thinness (stretch), but similarly a large amount of deposition to make up for the small pore size. At most, there seems to be only a 40nm difference in the sizes of the two membrane features.

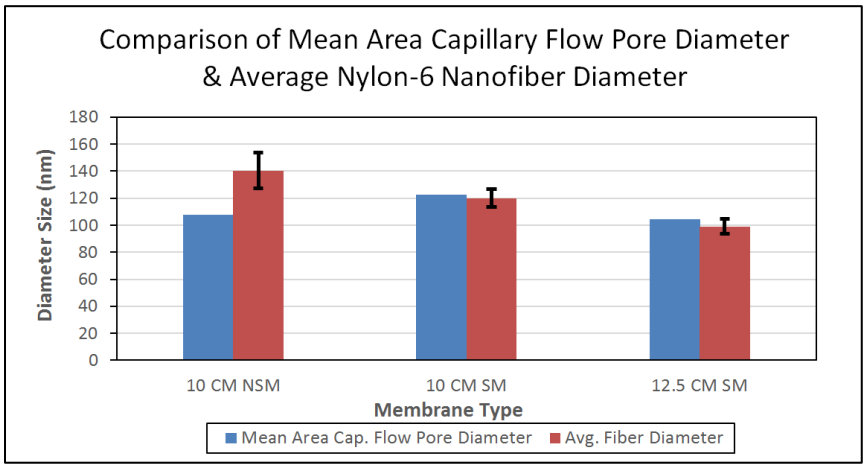

Figure 4.1-17 – Comparison of Mean Area Capillary Flow Pore Diameter with FESEM measured average fiber diameters for 3 electrospun membranes. Here, pore size strongly relates to fiber diameter size and also overall membrane weight. Even though the 12.5CM SM membrane has lowest weight, its fiber diameter and mean area pore diameter are very similar.

Furthermore, a comparison between the calculated numerical pore diameters from the porometer and the numerical mean pore diameters found through Feret's Diameter in Image J is shown in Figure 4.1-18.

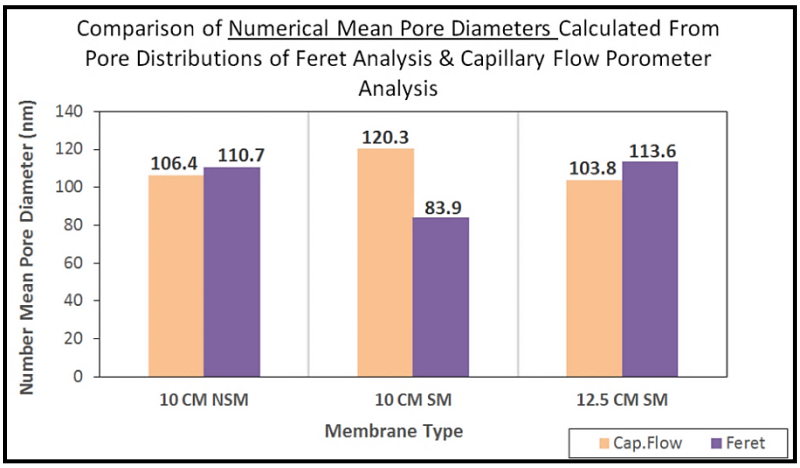

Figure 4.1-18 – Comparison of Capillary Flow Porometer numerical mean pore sizes and the FESEM Feret's Diameter numerical mean pore sizes (calculated using Equation 3.2).

Feret's diameter, in ImageJ, is calculated by approximating the pores in the SEM fiber membrane images as the size of a circular shape. It's calculated by measuring the distance from the center of that shape to the edge. A series of line distances (approximately 5 degrees apart) from the center to the edge are averaged. The average represents a numerical "pore" or "particle" size. This type of averaging for many lines also ensures a high degree of accuracy for giving the approximate size of the desired shape.

For finding the average pore sizes in nanofiber membranes, it's necessary to subtract the fiber features from each image by using a thresholding function in Image J. Two representative final images showing the subtraction of the fibers in the red threshold and their labeled count numbers are shown in Figure 4.1-19. Since Feret's diameter calculations on nanofiber images depend on the user's ability to perform a "fair" threshold, ("fair" – meaning that image pixels are not discriminated too much or too little from what the "pore" area would be) the pore sizes calculated can be subject to errors.

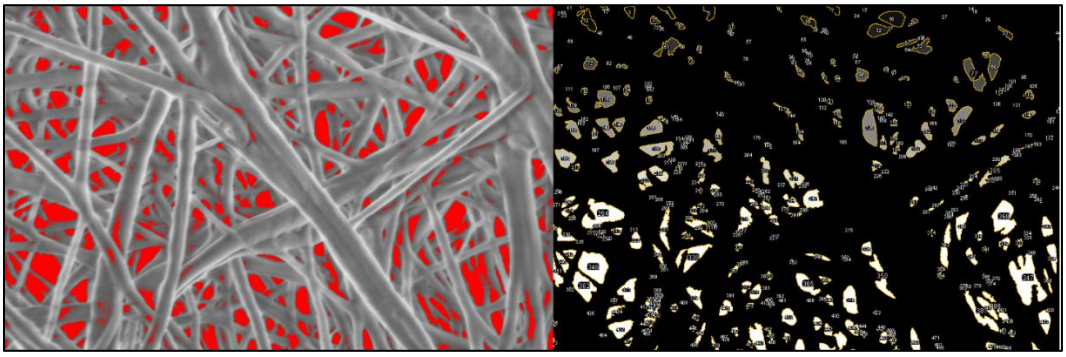

Figure 4.1-19 – Red threshold (left image) of an FESEM nanofiber image showing the pores to be counted and measured using Feret's Diameter function in ImageJ. The final binary image (right) shows the labeled "pores" counted in white.

However, from Figure 4.1-18, the Feret diameters calculated are on average not more than a ¼ size smaller than those obtained from the capillary flow porometer. At most, for all three membranes, there exists approximately a 30% difference with the two types of pore analysis performed, but this was not found to be statistically significant.

This is good because it shows three positive outcomes: first, the manual calculation of pore sizes using FESEM images is a valid method, and second, the 2 methods of pore analysis illustrate the presence of multiple nano-layers present in the membranes as a whole. Sub-layers in the membranes account for different types of pore sizes seen and contribute to the surface area. Third, it also shows that while macroscopically there may be large differences in the 3 different membranes (weight, density, and translucency), the nano-features (pore & fiber diameters) are all very similar.

Knowing this, the aerosol capture results for these membrane substrates should be similar, based on the fiber capture theory regarding slip flow at the fiber surface. However, results from the aerosol capture in Chapter 4.3 show that different capture results were influenced by mostly mechanical reasons.

Difference in Pore Analysis Methods

Overall, however, there is a significant difference in the theory for the two methods of pore analysis. Not only is the Feret's Diameter calculation dependent on threshold, and the FESEM image to give an accurate pore size, its results can only be used to calculate the numerical mean pore diameters of the membranes seen. It is unlike the capillary flow porometry method, which gives results that can be used to calculate both the numerical mean pore diameter and the mean area pore diameter. The advantage of knowing the mean area pore diameter is that this is the most representative pore size which can be used to judge how well the membrane can function in filtration applications.

Porometer pore sizes are based on fiber cross-sectional area as gas penetrates them, while Feret's diameter only assumes a 2-D fiber surface and that pore sizes are basically the average of distance lengths. As previously mentioned, though Feret's Diameter can be used to gain an accurate preliminary overview of the numerical mean diameter, it cannot account for the 3-D structure of the actual electrospun membrane pores like the porometer can. Therefore, the most accurate pore size results for the membranes can be seen in Figure 4.1-16, which rely on the shape, thickness and "throat" area of the pores themselves.

4.1.3.3 - BET Surface Area Analysis

Sample	BET Surface Area (m^2/g)
[#1] Espun @ 10CM, NSM	58.10 ± 1.48
[#2] Espun @ 10CM, SM	44.27 ± 0.71
[#3] Espun @ 12.5CM, SM	57.10 ± 1.87
Commercial Filter Paper	2.19 ± 0.02

Table 4.1.4 – BET surface area analysis of 3 electrospun Nylon-6 membranes and a commercial filter paper.

The surface area calculated for the three membranes, and for one sample of commercial filter paper, (Whatman brand) are shown in Table 4.1.4. Again, the differences between the area calculated for all three electrospun membranes are small (~20% difference from the highest and lowest values). This is expected. With smaller pore and fiber diameters, there is more area created per gram of sample for potential particle capture, or functionalization chemistry to occur.

The most significant difference is between the electrospun samples and the filter paper. While the commercial filter paper may be thicker in size, on the millimeter scale, and macroscopically appears more tightly packed as a nonwoven, the microscopic packing of the fibers is not as uniform as that of the nanofiber membranes. This, in turn, causes the irregular and large (on the micron scale) pore sizes seen for the filter paper. As such, the surface area is extremely low when compared to the electrospun membranes.

From the aerosol capture results presented in Chapter 4.3, we see that a major drawback to potentially using these stiff materials in wearable textiles for capturing exhaled aerosols is their ability to degrade once too much water is absorbed. Part of this problem is due the composition of these papers (cellulose / cotton), and the way their nonwoven structure was created.

4.1.3.4 – Wettability & DSC Crystallinity Results.

Wettability results of the three standard membranes are shown in Figure 4.1-20. Considering that between the first 0 – 100 seconds, the fraction of water absorbed was between 30% - 40%, the crystallinity of these electrospun membranes were determined to be quite high. DSC related crystallinity calculations shown in Figure 4.1-21 for two most cited Nylon-6 ΔH values (for 100% crystallinity) also show that the membranes are 30% - 40% crystalline. Raw DSC data is shown in Figure 2 of the Appendix.

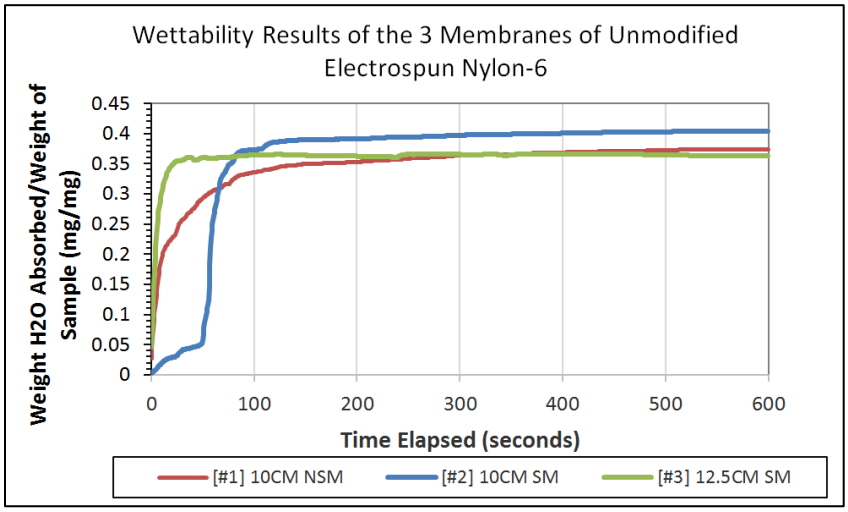

Figure 4.1-20 – Water moisture uptake (wettability) results of 3 Nylon-6 nanofiber membranes.

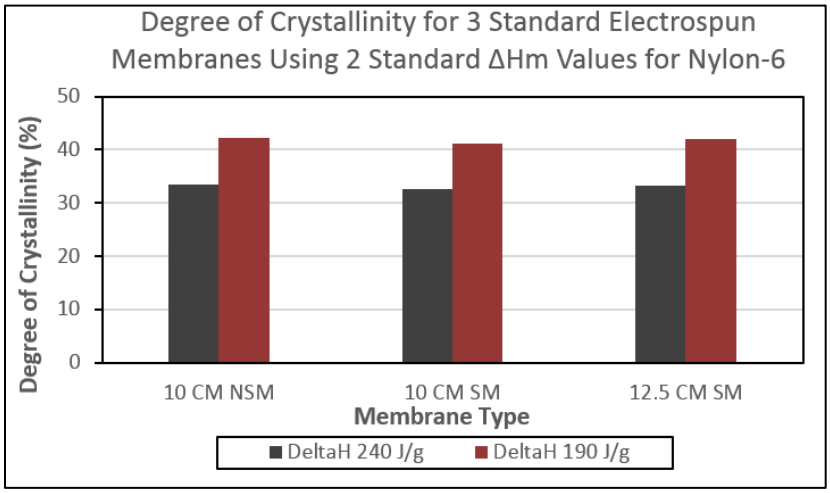

Figure 4.1-21 – Calculated % Crystallinity of 3 Electrospun Nylon-6 Membranes for 2 reference DeltaH (ΔH_m) values.

On average, most materials considered "wettable" or "moisture absorbent" absorb 80% to over 100% of moisture. Such materials are often powders or other highly hydrophilic compounds. For electrospun materials, it's even more unlikely to have a crystalline fiber membrane. Though alignment can occur in the fiber spinning direction, due to the tension produced between the charged fiber jet and the grounded collector, on average, crystallinity tends to be lower for electrospun materials than for films of the same composition.[112, 113]

A comparison in the DSC results of the membranes after surface treatment grafting with the hydrophilic acrylic acid monomer in Chapter 4.2, will show the changes in the observed ΔH values and how crystallinity was affected. These results for the grafted membranes showed a decrease in the overall wettability, though evidence of successful was grafting was present. Further characterizations of the surface modified electrospun Nylon-6 were performed using FESEM and FTIR analysis.

Surface modifications using gamma irradiation for the electrospun membranes, as opposed to chemical crosslinkers, were found to work much more successfully.

4.2 - Nylon-6 Nanofiber Surface Modification Using Acrylic Acid & Poly(Acrylic Acid) By Two Physicochemical Grafting Methods

All three of the 20wt% Nylon-6 nanofiber membranes standards seen in Chapter 4.1, Figure 4.1-9, electrospun at different needle tip-to collector distances (10 cm, and 12.5 cm), with two different rotating collector configurations (with axial sliding motion [SM], and without axial sliding motion [NSM]), were found to have similar fiber diameter sizes between 100 nm – 200 nm.

However, because membrane – 12.5CM SM, had the least fiber mat density and coverage (Figure 4.1-12 & Figure 4.1-13), the denser membranes, 10CM SM and 10CM NSM, were used for acrylic acid and poly(acrylic acid) grafting. Denser membranes should have an increased number of amine sites available for reaction and greater physical resistance to damage during the reaction process. The two methods for grafting used were: γ(gamma) irradiation and EDC [1-Ethyl-3-(3-dimethylaminopropyl)carbodiimide] coupling. Characterization results (FTIR, FESEM, TGA, DSC, and Wettability) were analyzed to determine which method yielded the most abundant, practical, and reproducible grafted product.

4.2.1 – Grafting by: Mutual Gamma Irradiation

4.2.1.1 – FTIR Results

The baseline corrected, and normalized, FTIR spectra of 4 random samples of untreated 10cm electrospun Nylon-6 are shown in Figure 4.2-1A. Figure 4.2-1B shows the comparison of one electrospun sample against those of 2 commercial Nylon samples (Titan3^{TM} Syringe Filters, Thermo Scientific).

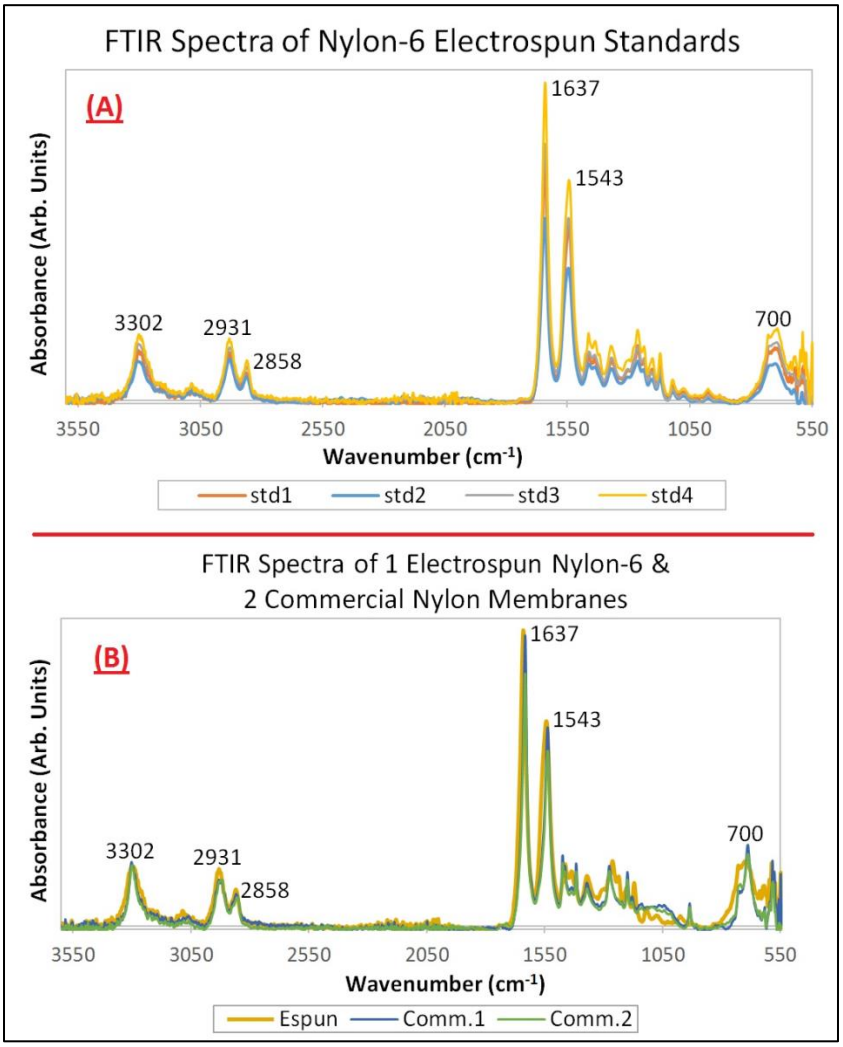

Figure 4.2-1 – FTIR spectra of Nylon-6 electrospun (A) and commercial [Comm.] (B) standards.

Both spectra show a good agreement for the main six absorbance peak values of Nylon cited in literature.[114, 115] This peak agreement also confirms that the electrospun samples were free from impurities that may have collected during the spinning process. The sharp peak at 3302 cm^{-1} corresponds to the amide [C-N] stretch. This peak cannot be mistaken for an alcohol stretch band because, unlike the [—OH] peak, it is not broad and does not expand into the 3400cm^{-1} region. The two peaks at 1637 cm^{-1} and 1543cm^{-1} are characteristic of Nylon because they indicate the presence of amide interactions as well; particularly, the [C=O] carbonyl group which is commonly seen at 1640cm^{-1}. The lower wavenumber of this peak in the commercial spectra is due to the possible overlap of the

[−NH] bending band also occurring at 1543cm^{-1}. Often, this bending peak is commonly seen within the 1540cm^{-1} – 1640 cm^{-1} range. This is because it shows both the stretching and bending interactions between all three atoms: carbon, nitrogen and hydrogen in the Nylon amide group. Furthermore, this observed interaction is subject to slight changes based on the sample type (solid pellet, solid film, liquid…etc) examined in the spectrometer. The peaks at 2931 cm^{-1} and 2858cm^{-1} are characteristic of the sp^3 hybridized symmetric and asymmetric [C–H] stretches present in the backbone. Finally, the broad peak at 700 cm^{-1} refers to the out-of-plane bending that the amide bond can undergo. The features of this peak (its broadness, sharpness…etc) are particularly sensitive to the crystalline structure of the Nylon chain, and can change depending on the polymorphism of Nylon.

Distinctions between the types of Nylon present (whether they are Nylon-6/6,6/6,10…etc) are generally difficult to make using FTIR analysis alone. According to Arimoto et al., transitions between the α, β and γ polycrystalline phases of Nylon-6 are observable through X-Ray Diffraction Spectroscopy (XRD).[116] Therefore, it is also possible that the minor differences in peak wavenumber values seen amongst the control samples can be due to slight differences in the amide polymorphic structure.[114] If necessary, the minor differences in these types of isomers can be further analyzed by observing the fingerprint region between 900cm^{-1} and 1300cm^{-1}, but this is beyond the scope of this work.[117]

For all three polymorphic structures of Nylon-6 possible (α, β and γ), there is no characteristic infrared absorbance peak present in the 1720cm^{-1} – 1730cm^{-1} region. After gamma irradiation♠ and exposure to the acrylic acid monomer, the FTIR spectra of the electrospun samples exhibited this new peak range in the mid-1700cm^{-1} region (Figure 4.2-2). This was also accompanied by a downward shift of the 6 characteristic Nylon standard peaks, and the appearance of new peaks within the fingerprint region.

♠ Exposure for 1 minute at 523rads/min.

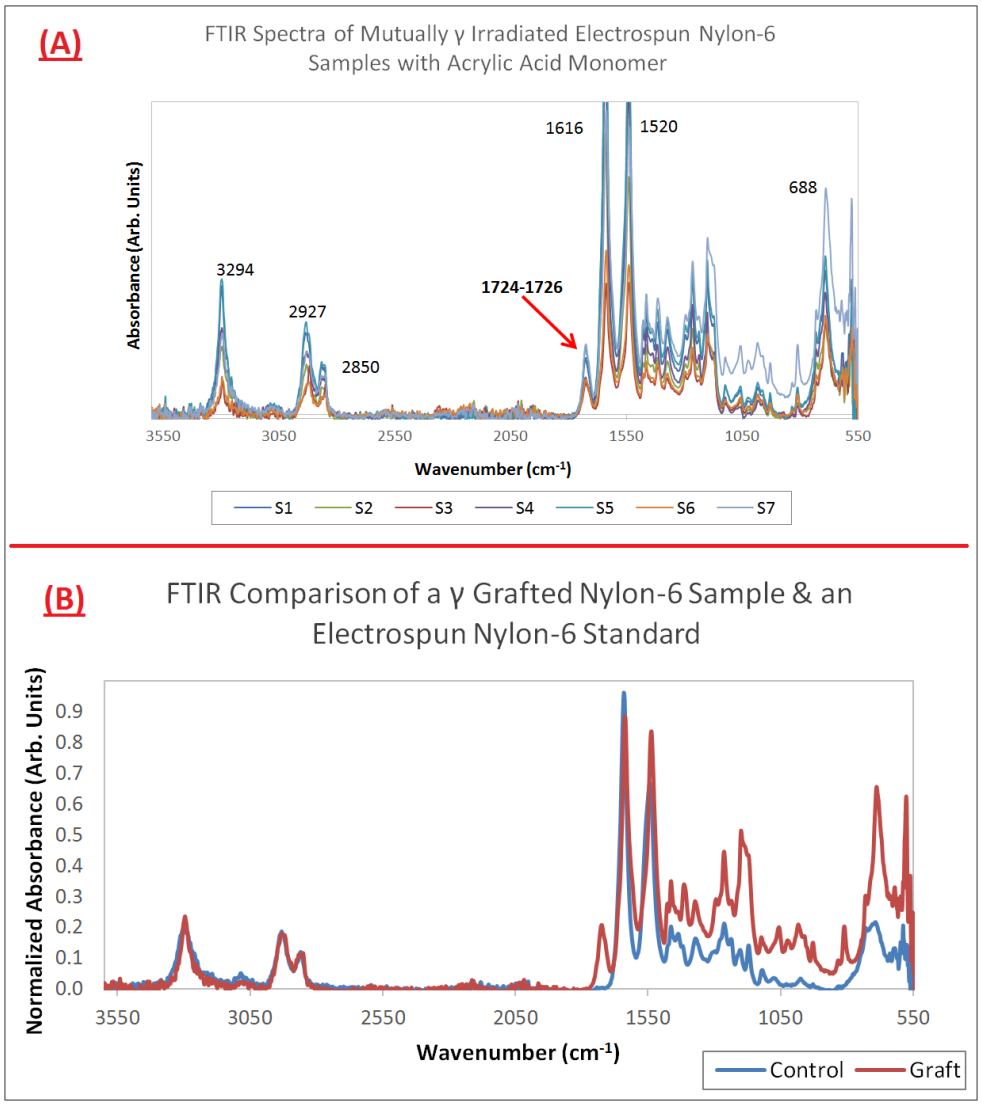

Figure 4.2-2 – FTIR spectra of mutually γ irradiated electrospun Nylon-6 samples in acrylic acid monomer solution. All grafted samples: (A). A representative grafted sample compared with an unmodified standard: (B).

According to Hummel and Scholl, strong absorption bands for the coupled vibrational modes: [C–N] and [N–H], from 1540cm^{-1} to 1600cm^{-1}, result from the presence of the very polar amide groups in Nylons.[114] The observed weakness for these usually strong bands in the electrospun membranes indicates that they have reduced polarity. This may have resulted from either: an attachment of a nonpolar chain to the group, during modification (i.e. polymerized acrylic acid), or chain scission occurring at the amide site. Figure 4.2-3 shows the possible reaction pathways that the acrylic acid monomer may have taken in order

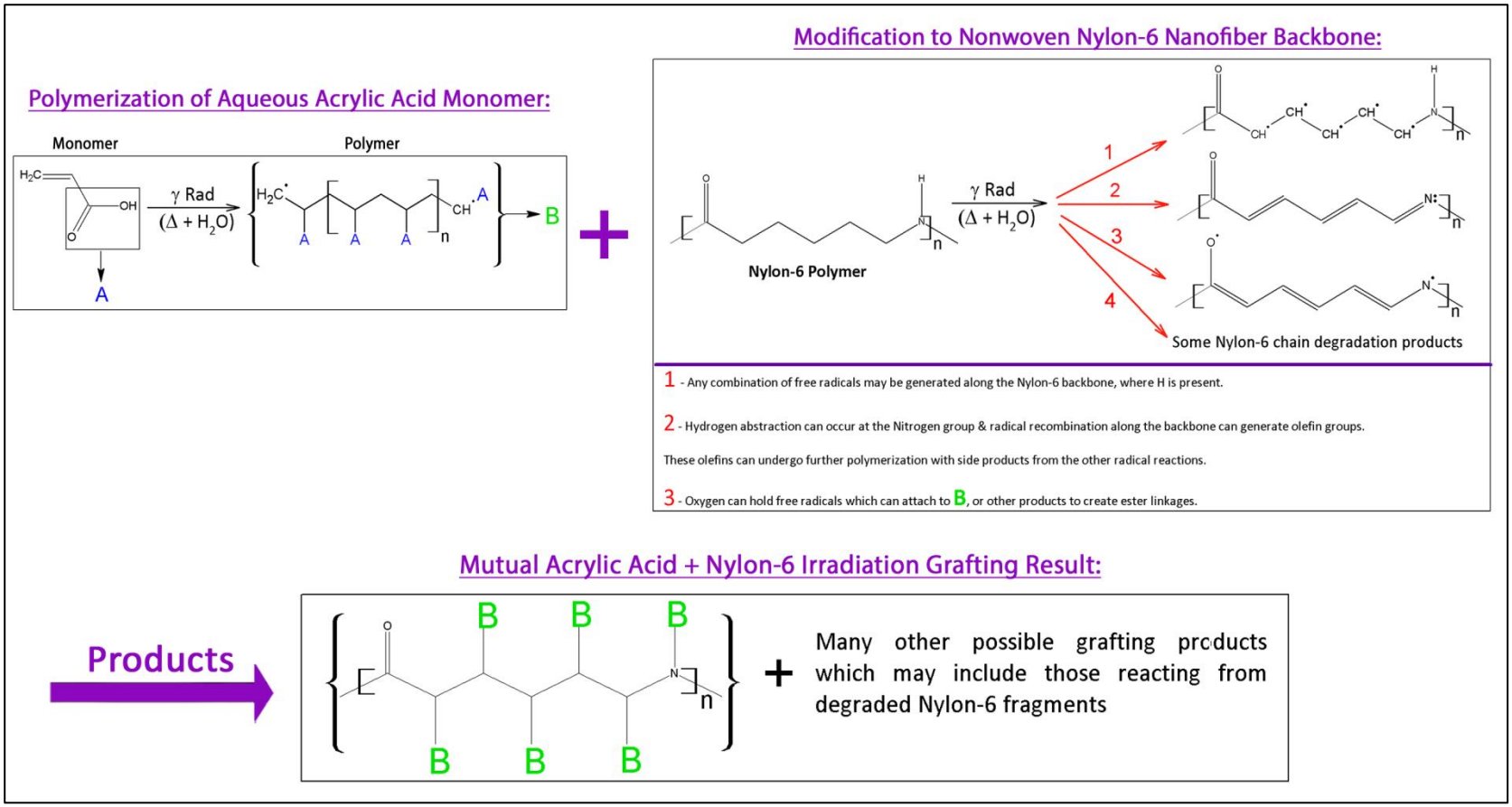

Figure 4.2-3 - Free radical polymerization reaction scheme detailing the possible routes (not intermediates, necessarily) for: acrylic acid polymerization, & acrylic acid polymer combination with Nylon-6 chanins in nanofibers after mutual gamma (γ) irradiation. Hydrogen abstraction will occur from the Nylon-6 backbone. This creates highly reactive alkene groups which may interact with polymerized acrylic acid (B) in various ways (Paths: 1 - 4). These interactive pathways can result in grafted products containing various degrees of acrylic acid chains. The carboxylic acid group [-CO2H] in acrylic acid favors side reactions as well.

to polymerize and graft onto the Nylon-6 backbone.

From the FTIR results seen above, it is likely that pathway #1 from Figure 4.2-3 occurred, with some transformations in the carboxylic acids. Infrared absorbance peaks within the 1715cm^{-1} to 1730cm^{-1} region are often indicative of esters in the sample. While carbonyls [R—C=O] from many carboxylic acid containing compounds, such as acrylic and poly(acrylic acid), are often observed in the 1740cm^{-1} region, the carbonyl groups from esters [R—O—C=O] appear in this region as well.[114, 118-121] They are usually towards the lower 1720cm^{-1} end due to resonance effects from the [R—O—C] bond.

Additionally, the baseline corrected ratio between the absorbance of this new 1724 cm^{-1} peak, and the absorbance of the carbonyl-amide [—N—C=O] stretch at 1637cm^{-1} averages at 16.8% $\pm$ 7.2% (α=0.05). In other words, the chance of radical induced grafting taking place as a result of exposing both the nanofiber membrane and the acrylic acid monomer to gamma irradiation for the same amount of time, is about 16%, based on the formation of this new ester peak at 1724cm^{-1}. Similarly, taking the ratio between the normalized absorbance heights at the 1700cm^{-1} peaks, and the normalized average absorbance height of the carbonyl –amide peaks from the control standards, there is a 20.1% $\pm$ 5.4% difference[♥] (α=0.05). This suggests that this new peak consistently absorbs at the same relative 20% height for every Nylon sample mutually gamma irradiated in a 10% acrylic acid solution. Table 4.2.1, and Table 4.2.2, shows the absorbency ratios for the normalized and base-line corrected standards and grafted samples.

[♥] When the errors associated with both the peak absorbance heights in the grafted samples & the control samples are propagated, the new error is 11.4%.

Comparison of 1700cm-1 Graft Peak Height with Carbonyl (C=O) Absorbance Heights within Sample					
# Sample	Graft Peak (Absorb.)	C=O Amide (Absorb.)	Ratio of Absorb.	Ratio (%) of Absorb.	
1	0.0145	0.1176	0.1233	12.330	
2	0.0093	0.0723	0.1286	12.863	
3	0.008	0.0335	0.2388	23.881	
4	0.0095	0.0947	0.1003	10.032	
5	0.0174	0.1261	0.1380	13.799	
6	0.009	0.0420	0.2143	21.429	
7	0.018	0.0778	0.2314	23.136	
				16.781	**Avg**
				7.205	**Err (95%)**
				5.802	**St.De**

Table 4.2.1 – Average ratio of new Graft Peak absorbance height at 1700cm^{-1} to Carbonyl Amide (C=O) peak height in grafted samples (pink box) with 95% confidence error and standard deviation.

Comparison of 1700cm-1 Graft Peak Height w/ Average Carbonyl (C=O) Absorbance Heights From Standards					
Avg. C=O Normalized Absorb. From Standards	# Sample	Normalized Graft Peak (Absorb.)	Ratio of Absorb.	Ratio (%) of Absorb.	
0.7313	1	0.1160	0.1586	15.863	
	2	0.1680	0.2297	22.974	
	3	0.1620	0.2215	22.154	
	4	0.1160	0.1586	15.863	
	5	0.0950	0.1299	12.991	
	6	0.1620	0.2215	22.154	
	7	0.2100	0.2872	28.718	
				20.103	**Avg**
				5.438	**Err (95%)**
				5.029	**St.De**

Table 4.2.2 – Average of ratio of new Graft Peak height to Average carbonyl amide peak height from standard unmodified samples (green box) with 95% confidence error and standard deviation.♣

Furthermore, Table 4.2.3 shows an increased 1:1 ratio between the carbonyl stretch (1635cm^{-1}) and the carbon-nitrogen-hydrogen bend (1520cm^{-1}) absorbencies. For the gamma grafted samples there was 88% equivalence in absorbency, as opposed to the spectra of the standard membranes which continuously had only a 70% similarity between their peak heights. In other words, a significant decrease in the ratio heights between the two main characteristic Nylon peaks at 1635cm^{-1} and 1520cm^{-1} occurred after grafting.

♣ Unlike the values in Table 4.2.1, these values were normalized to account for the fact that ratios were taken from 2 different sample types: the grafted samples, & the standard unmodified samples.

Ratio Between CO-NH Stretch (1635cm-1) & CN|NH Bend (1520cm-1) for Graft Samples				
# Sample	Stretch (1635cm-1) Absorb.	Bend (1520cm-1) Absorb.	Absorb. Ratio (%) of Bend/Stretch	
1	0.1180	0.0950	80.508	
2	0.0690	0.0610	88.406	
3	0.0330	0.0330	100.000	
4	0.0940	0.0790	84.043	
5	0.1260	0.1010	80.159	
6	0.0420	0.0380	90.476	
7	0.0780	0.0740	94.872	
(A)			88.352 7.782 7.415	Avg Err (95%) St.De

Ratio Between CO-NH Stretch (1637cm-1) & CN|NH Bend (1543cm-1) for Unmodified Standards				
# Sample	Stretch (1637cm-1) Absorb.	Bend (1520cm-1) Absorb.	Absorb. Ratio (%) of Bend/Stretch	
1	0.7620	0.5170	67.848	
2	0.5430	0.3940	72.560	
3	0.7730	0.5470	70.763	
4	0.9530	0.6600	69.255	
5	0.9240	0.6440	69.697	
6	0.8060	0.5690	70.596	
(B)			70.120 1.671 1.593	Avg Err (95%) St.De

Table 4.2.3 – Change in ratio of Carbonyl-Amide Stretch (1635cm^{-1}) to Carbon-Nitrogen-Hydrogen Bend (1520cm^{-1}) for the grafted samples (A) compared to the ratio in the standard controls (B).

Photo-oxidative degradation of Nylons from exposure to UV radiation alone has the effect of increasing the 167cm^{-1} stretch absorbance significantly.[122, 123] This is due to the formation of [-CH=CH$_2$-] groups after cleavage from the amide in the Nylon backbone. While it appears as though both the 1520cm^{-1} and 1635cm^{-1} peaks in Figure 4.2-1 and Figure 4.2-2, and in Table 4.2.3 are increasing, the formed ester peak at 1724cm^{-1} may be causing the reduction of the original 1635cm^{-1} carbonyl-amide stretch. The resonance effects from the added oxygen of the acrylic acid's carboxylate group, and the possible products generated (Figure 4.2-3), could be enough to decrease the absorbency in this carbonyl region. This would account for the resulting 1635cm^{-1} stretch and 1520cm^{-1} bends to increase in equivalency. Figure 4.2-4 shows the new 1635cm^{-1} shifted stretches and 1520cm^{-1} shifted bends in the grafted Nylon-6.

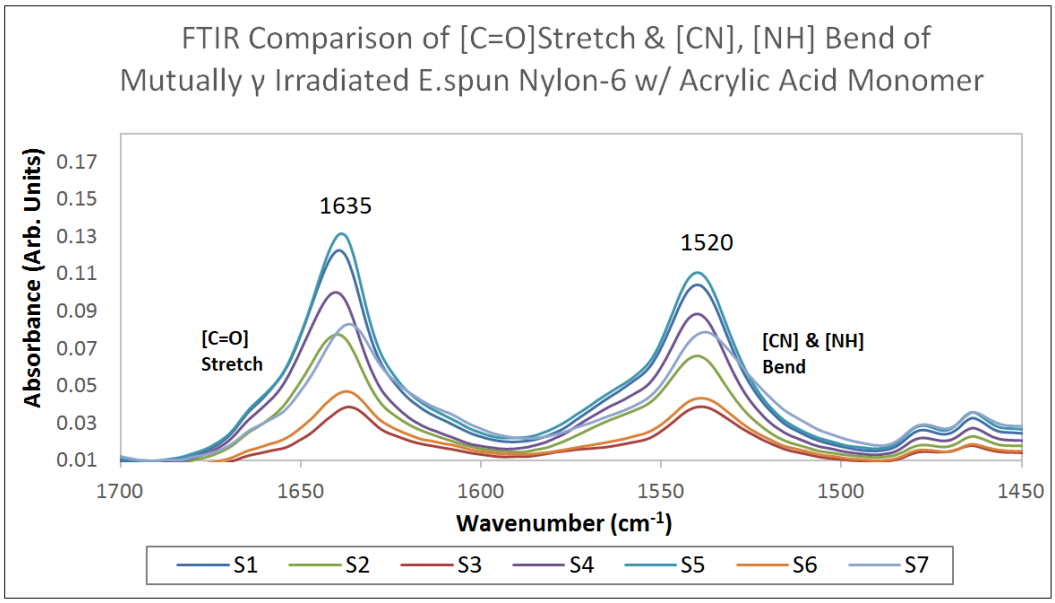

Figure 4.2-4 – Increase in peak height equivalency for the [C=O] Stretch & [CN] &[NH] bends in the grafted samples.

Changes within the fingerprint regions are shown in Figures 4.2-5. Compared to the electrospun and commercial Nylon, the mutually irradiated Nylon grafted samples show a new peak at 808cm^{-1}, sharpening of original peaks at: 1265cm^{-1}, 1199cm^{-1}, 700cm^{-1}, and a shift plus increase of the stretch at 1051cm^{-1}. From literature, it's known that full incorporation of acrylic acid usually results in a sharp new absorbance at 1051cm^{-1} for the copolymer blend.[124, 125] Another characteristic of pure acrylic and poly(acrylic acid) in this region is the alkene vibrations [—CH=CH—] near 980cm^{-1}.[125]

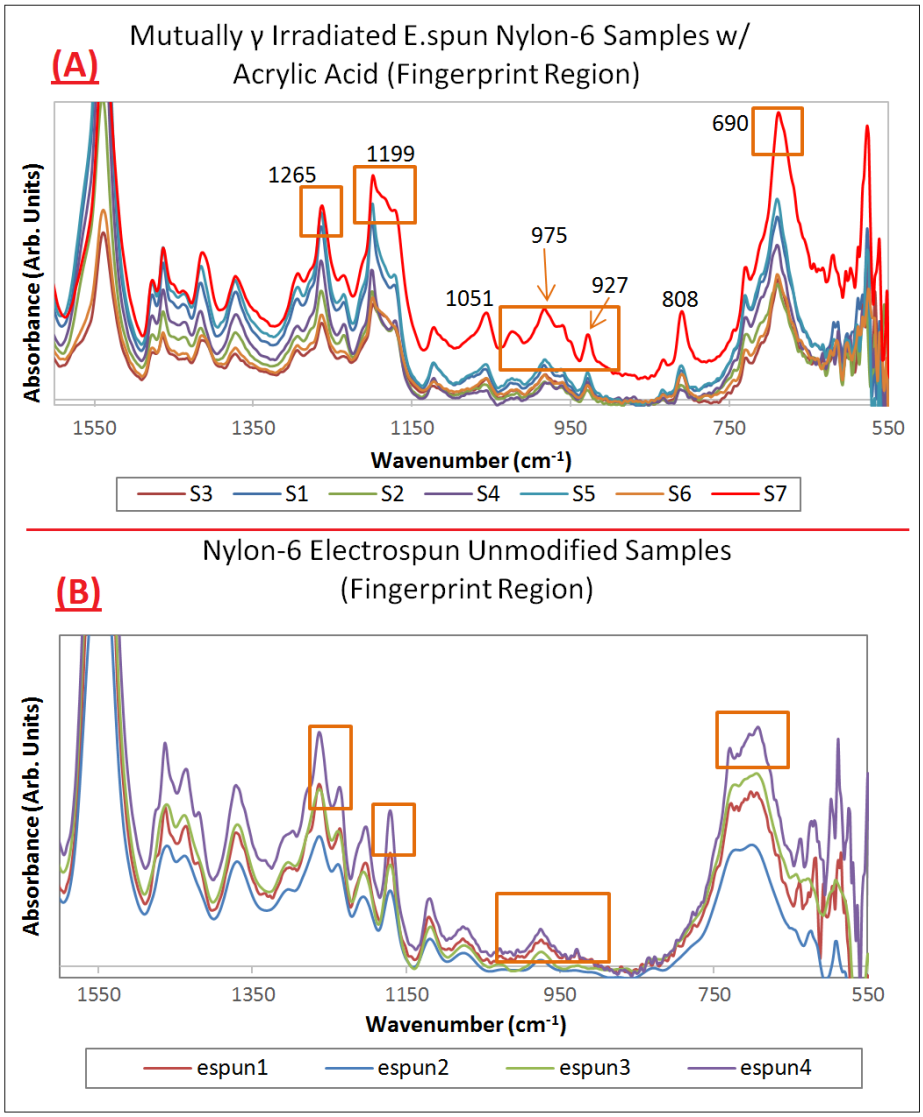

Figure 4.2-5 – Comparison of changes in the fingerprint region for the gamma irradiated grafted Nylon-6 (A), and unmodified electrospun Nylon-6 (B). The orange boxes indicate the peaks which changed in morphological shape & height.

Even though the FTIR data conclusively confirms poly(acrylic acid) addition at the free radical sites along the Nylon-6 carbon backbone, because the peaks at 1199cm^{-1} and at 1265cm^{-1} are still present in the grafted samples, we can conclude that the acrylic acid monomer was only added onto the surface on the Nylon-6 membranes. Had the peaks at 1199cm^{-1} and at 1265cm^{-1} reduced, or disappeared, this would have indicated that a fully integrated copolymer blend of Nylon-6 and acrylic acid formed, rather than just surface grafting. However, since surface grafting did occur, the peak at 1051cm^{-1} (which is ester

related) shows grafting was favored as well.

4.2.1.2 – FESEM Results

The FESEM image in Figure 4.2-6 shows the polymerized acrylic acid in monodisperse colloid spheres, and a film layer adhered to the fiber surfaces. Spheres average between 330.88nm – 447.36nm $\pm$ 42.46 (α=0.05/n=76) in size. The relationship between spherical size and acrylic acid monomer concentration or molecular weight was not examined. However, studies focusing on colloid formation (PMMA & silica) have suggested that a proportional relationship between the two can exist.[98]

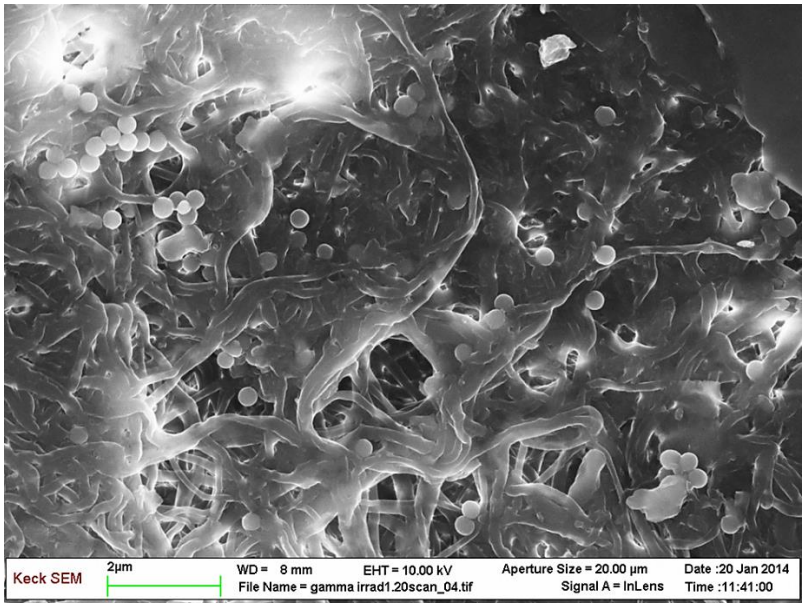

Figure 4.2-6 – Monodisperse polymerized colloid spheres of acrylic acid adhered on Nylon-6 fiber surface as a result of gamma irradiation exposure.

As controls, Nylon-6 was irradiated with no acrylic acid monomer present, and Nylon-6 with acrylic acid monomer were mixed without exposure to gamma irradiation. No change in the Nylon-6 membrane occurred in either of these cases. Figure 4.2-7A shows the results of the electrospun Nylon-6 membrane after exposure to only gamma irradiation, while Figure 4.2-7B shows the membrane after only acrylic acid solution exposure, for the same period of time. No bead formation or fiber alterations occur after exposure to just

monomer or just irradiation alone. No evidence of fiber breakage, change in surface morphology or change in fiber diameter was observed after these procedures.

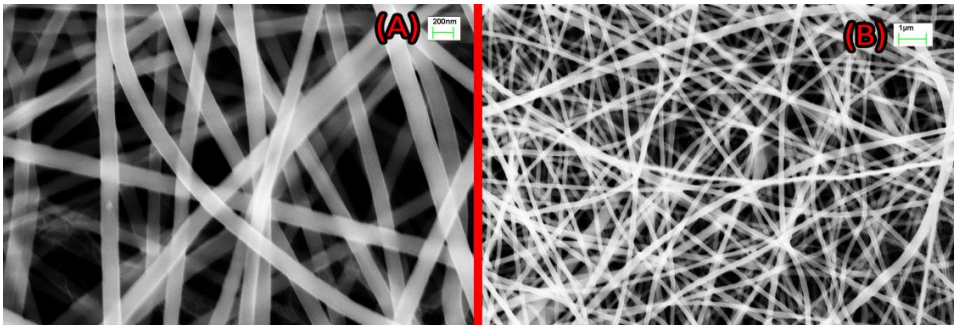

Figure 4.2-7 – No significant changes in fiber morphology after Nylon-6 exposure to only: gamma irradiation (A), and acrylic acid monomer (B). Irradiation exposure time is for 1 minute (i.e. the same amount of time that the Nylon nanofiber membranes with acrylic acid in Figures 4.2-6, & Figures 4.2-8 were exposed to).

Figure 4.2-8 A through Figure 4.2-8 I show the total scope of material transformations that the electrospun Nylon material withstood as a result of the gamma irradiation grafting process. Coagulation and gelation of the fibers was accompanied with the formation of a film-like structure over the surface (Figure 4.2-8 C, G, H, I). The integration of the monodisperse spheres within the fiber pores can be seen in Figure 4.2-8 D, E, F. While it's evident that pore sizes of the fiber membrane are reduced from the original unmodified membrane due to the coagulation, the question remains as to how much of the new film structures and the coagulated fibers seen is actually acrylic acid or Nylon-6.

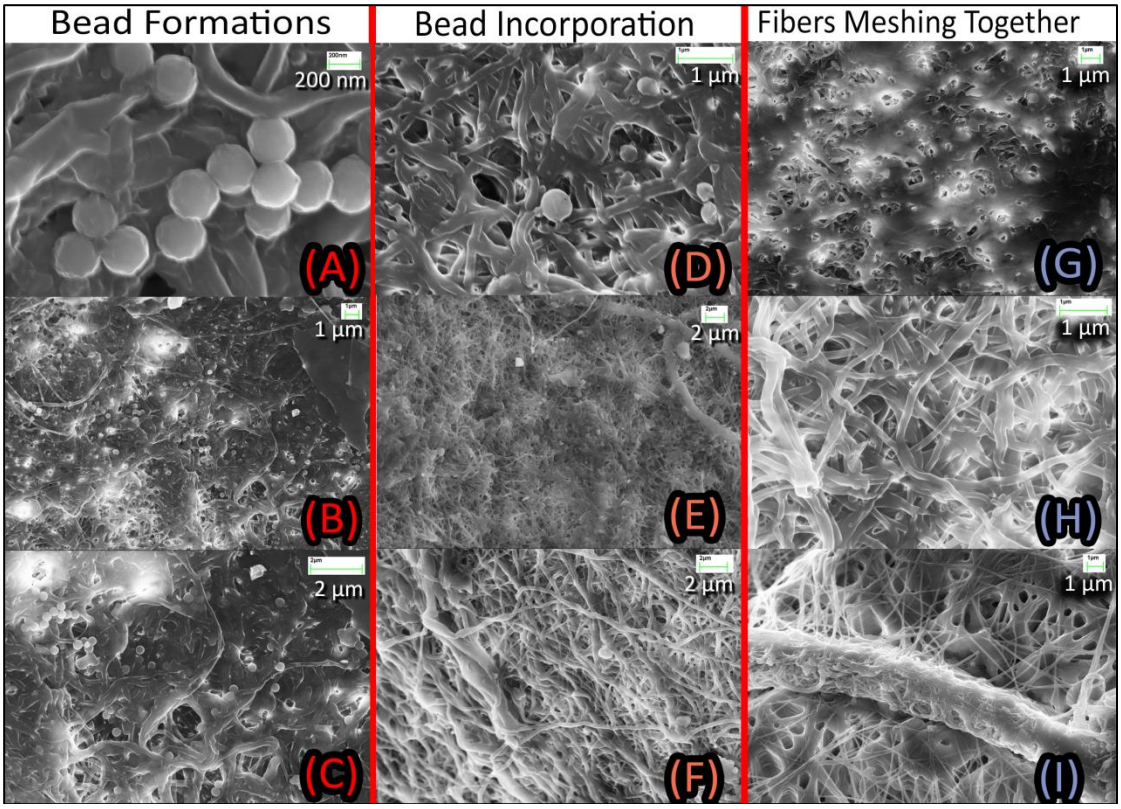

Figure 4.2-8 (A-I) – Three sets of morphological changes seen in the gamma irradiated grafted membranes using FESEM. (A-C): Formation of mono-disperse acrylic acid bead, (D-F): Integration of these beads in the fibers as films and other large chunks, (G-I): Fibers loosing shape and meshing.

4.2.1.3 – Membrane Weight Change & Increased Gamma Irradiation Exposure Results

To estimate the add-on of poly(acrylic acid) to the Nylon-6 membranes, calculations of weight percent increase and decrease after grafting are shown in Table 4.2.4. On average there is an overall 9.41% $\pm$ 4.76% weight increase for the gamma irradiated grafted samples. There was also shrinkage in the length and width of the samples post treatment by 4cm – 7cm.

Mutual Gamma Irradiation Grafting Method (Change in Wts. & Macroscopic Morph.)				Dimensional Loss in Length (cm)	
Irradiation Time (Min)	**Initial Wt (g)**	**Final Wt (g)**	**Graft Wt. Change (% Change)**	**Length**	**Width**
1 (No Monomer)	0.0053	0.0051	-3.77	0.01	0.00
1	0.0119	0.0124	4.20	-4.00	-0.50
1	0.0122	0.0131	7.38	**-7.00**	0.10
1	0.0123	0.0129	4.88	-4.00	-0.50
1	0.0126	0.0144	14.29	-3.00	-1.00
1	0.012	0.0137	14.17	-4.00	-1.50
1	0.013	0.0145	11.54	-3.00	-1.00
		Avg	**9.41**	**4.17**	**0.77**
		Error	**4.76**	**1.54**	**0.52**
		StDev	**4.53**	**1.47**	**0.50**
Extra Samples					
5 Min (No Monomer)	0.0065	0.0068	**4.62**	**-10.0**	**0.0**
20 Min (W/ Monomer)	0.0049	0.0052	**6.12**	**-11.0**	**-1.5**

Table 4.2.4 – Nylon-6 membrane weight % increases after mutual gamma irradiation grafting (light blue). Average shrinkage in Length (cm) & Width (cm) is shown (light blue). Original Length & Width: 15cm x 2.5 cm.

For the 1st sample in Table 4.2.4, without monomer exposure, there was a slight weight decrease observed, but without significant changes in the fiber morphology. Here, the short period of irradiation exposure without any other molecular interaction present may have just resulted in a cleaning/sterilization of the fibers. Gamma and UV irradiation are often used to sterilize nanofibers used for tissue scaffolds to promote biological cell growth. Though UV and gamma irradiation can result in weight loss of fibers, and a reduction in nanofiber diameter, the overall membrane morphology can remain unchanged.[144]

Contrary to expectation, for the most extreme case – the 20 minute irradiated sample with monomer exposure, revealed no dramatic weight increase in the final product (only a 6% increase). These two outcomes suggest that competing reactions occurred during the mutual irradiation process. As irradiation dosage increased, the rate of nanofiber disassembly competed with the rate of acrylic acid monomer attachment to the membrane.

After 5 minutes of gamma exposure, without monomer, the Nylon showed increased webbing between the fibers in Figure 4.2-10; this suggests onset of fiber disassembly. With acrylic acid, the process may be accelerated so that for a shorter period of irradiation time, the membrane forms areas such as Figure 4.2-8 I. Then for increased exposure with acrylic acid present, both monomer integration within the fiber strands (not just monomer attached spheres), and morphological changes result, Figure 4.2-9. Since free radicals could have induced any number of reaction combinations resulting in both grafting and degradation of the membrane, the results of these two competing processes may have only just become apparent after longer gamma exposure times.

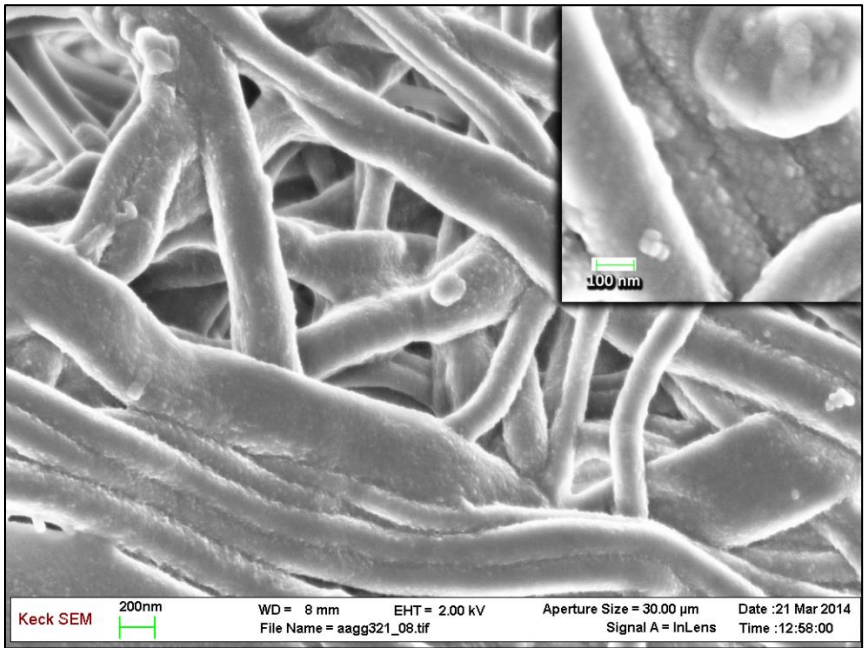

Figure 4.2-9 – Textured fiber surfaces and deeper integration of acrylic acid after 20 minute Nylon-6 membrane with acrylic acid gamma radiation exposure.

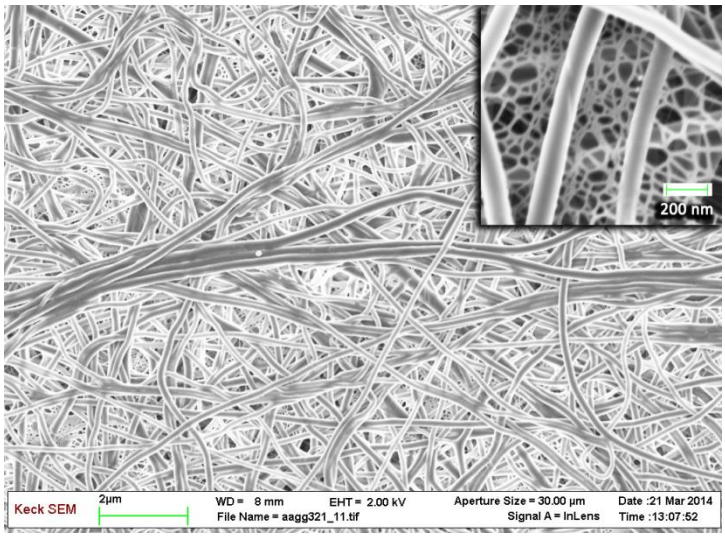

Figure 4.2-10 – Only gamma irradiation exposure to Nylon-6 membrane for 5 minutes.

Though there is a 16% acrylic acid ratio peak increase from the FTIR spectra of the grafted material, and a 9% weight increase from the gravimetric results, both types of measurements are not directly related. However, it is interesting that both share an increasing trend with similar orders in magnitude.

4.2.1.4 – BET Results

As previously mentioned, the pore sizes of the grafted samples also appeared to decrease dramatically from the unmodified electrospun Nylon (Figures 4.2-8C, D & Figure 4.2-9). BET analysis for the gamma irradiated grafted samples showed an overall surface area decrease, and also shrinkage of pore sizes.

Figure 4.2-11 shows the isotherm adsorption trend results for the gamma irradiated grafted Nylon-6 compared to the isotherm of the unmodified Nylon membrane with the same dimensions (2cm x 2cm). Though both sample curves appear to follow a similar BET Type II isotherm trend, the grafted sample shows a significantly lower adsorption concentration with a steeper incline near relative pressure equal 1. This lowered adsorption and flatter plateau suggest that adsorptive properties of the grafted sample are approaching the Type I isotherm. The difference in both Type II and Type I isotherms relate to a difference in pore sizes within the surface of a sample.[126, 127]

Type I isotherms tend to describe microporous materials with surface pore diameters less than $\leq$ 2nm. These materials are not multilayered and have small pores which can be quickly occupied by the adsorbate. Thus, once the pores of a Type I are filled, there is usually no remaining surface area for further adsorption to take place. The Type II isotherm, seen for the control unmodified electrospun sample, indicates that multiple layers of the material are exposed to the surface and that adsorption on these many levels can occur. Thus, these materials are mesoporous with exposed surface pore diameters between 2nm – 50nm.

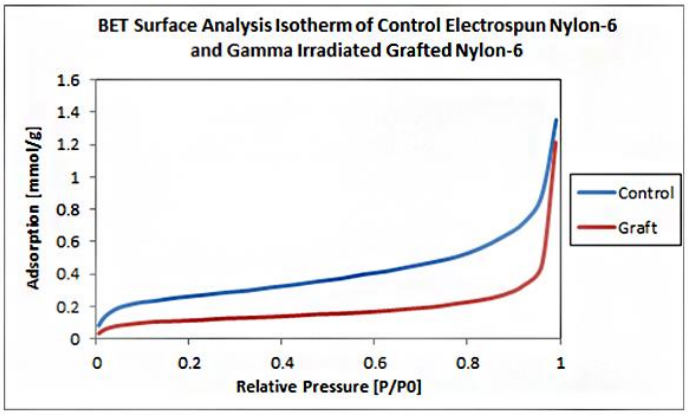

Figure 4.2-11 – BET adsorption isotherms of a gamma grafted Nylon-6 sample, and an electrospun control. The isotherm of the grafted sample mimics the Type I BET isotherm type. This indicates that the material surface is very flat, microporous and has no multiple layers.

The Type I, monolayer-like small pore size and small surface area characteristics of the grafted sample are further confirmed in Figure 4.2-12, Figure 4.2-13, which show the decreases in pore volume and area sizes, respectively. Table 4.2.5 also shows decreased surface area for the grafted sample, as a result of smaller pore area and volume sizes.

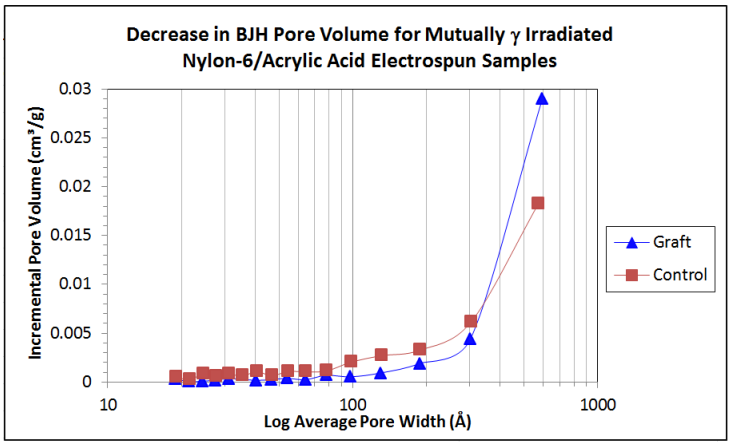

Figure 4.2-12 – Decrease in pore volume for gamma grafted samples.

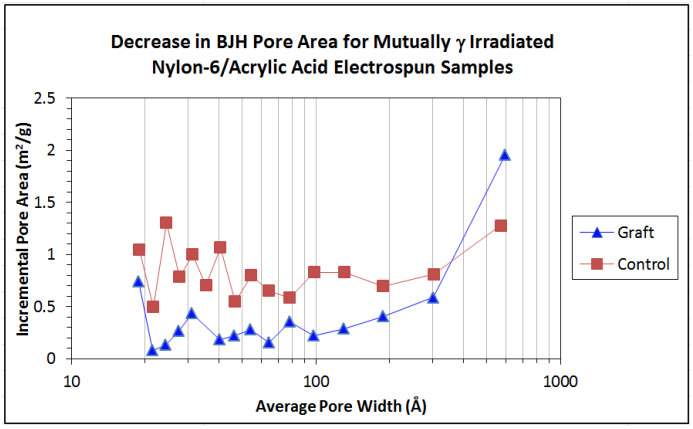

Figure 4.2-13 – Decrease in pore area for gamma grafted samples.

Sample	BET Surface Area (m^2/g)
Control Electrospun Nylon-6	20.92 ± 0.104
γ Acrylic Acid Grafted Electrospun Nylon-6	9.15 ± 0.212

Table 4.2.5 – Surface area of control nanofiber membrane versus that of a gamma grafted membrane.

Although, it was expected that the overall surface area of the grafted electrospun membranes would increase, due to the presence of acrylic acid monomer on the membrane surface (Figure 4.2-8 A, B, C), this did not occur because of a combination of the reaction conditions (monomer and irradiation exposure) and the film layer formed over the surface. The pH of the reaction between acrylic acid monomer and Nylon-6 membrane was 2, and so,

combined with the gamma radiation exposure; this may have caused some fiber coagulation. Thereby further reducing surface area in addition to the acrylic acid loading as a film. More areas like this present in the final membrane led to a reduction in surface area because there were no longer as many intertwined individual fibers able to contribute to the N_2 adsorption during the BET analysis. The congealed and flattened fibers with acrylic acid coating the surface also transformed the membrane into a monolayer-like material.

4.2.1.5 – DSC Results

Figure 4.2-14, the DSC thermogram of the grafted sample, shows a new broad transition near 125℃–130℃ which was not previously seen in the original unmodified Nylon-6 electrospun membrane DSC results.

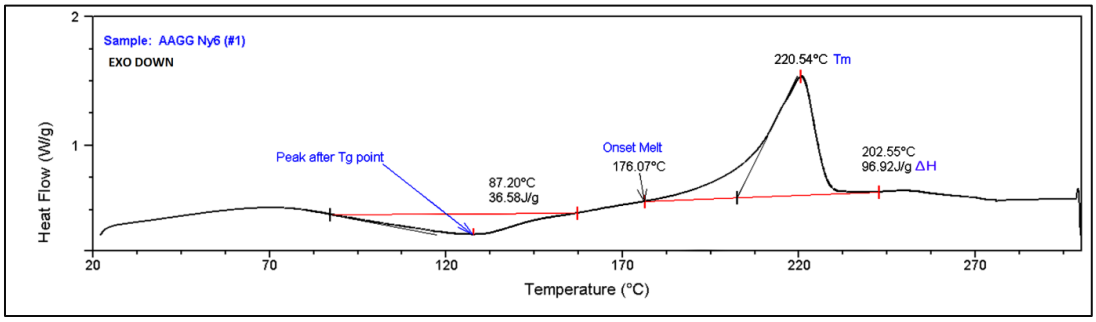

Figure 4.2-14 – DSC thermogram of gamma grafted Nylon-6 membranes showing a cold crystallization peak (~87℃), onset melt temp, melting temp (Tm), and its ΔH.

With increasing sample size, this transition increases in both depth and broadness. Increasing sample size does not affect the melting temperature of the membrane, nor does it increase the heat of enthalpy (ΔH). This transition beginning at 87.2℃ appears to be evidence of a cold crystallization. Initially, this feature can be mistaken for a glass transition step, but when this thermogram is compared to those of the standard, un-modified electrospun Nylon-6 membranes, the feature does not slope down and level off instantly. For the unmodified Nylon membranes this glass transition step occurs between 60℃–80℃. A thermogram of the unmodified Nylon membrane is compared against the thermogram of the

grafted sample in Figure 4.2-15.

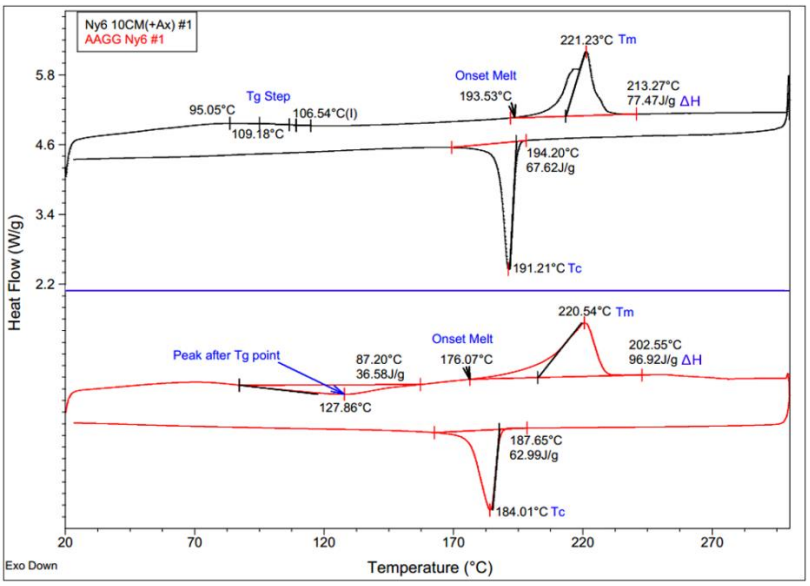

Figure 4.2-15 – Comparison of DSC thermograms for an unmodified Nylon-6 electrospun membrane (black) and a gamma acrylic acid grafted membrane (red).

It is still unclear whether this peak with minimum at 127°C is indicative of an emerging glass transition for the acrylic acid grafted on the membrane, or if it signifies the onset of partial Nylon crystallization. Literature with results of grafted acrylic acid and poly(acrylic acid) on materials have reported a similar broad DSC peak near 82°C–86°C as seen in Figure 4.2-14.[128] Though the melting temperature (T_m) of the grafted Nylon membrane remained the same, melting began 17 degrees sooner (176°C) and the ΔH necessary for melting was 19 J/g higher. Earlier T_m onset can indicate the presence of an additional component in the sample, as the new component can prevent the original polymer's crystallization and chain entanglement behaviors.

However, glass transition steps for polymers are known to vary based on sample history (previous material processing conditions), and surrounding humidity. Therefore, it's also possible that these factors may have also influenced the formation of the questionable minimum peak seen in the DSC of the grafted sample.

It is for certain, however, that structural changes within the crystalline phases of the Nylon polymer occurred. The thermograms of the unmodified Nylon-6 membranes, showed only glass transition and melting peaks, regardless of sample size used. Another characteristic of the unmodified membranes is that in all DSC thermograms, the poly-crystalline nature of Nylon-6 can be seen at the top of the T_m curve. For the grafted membranes, this split peak disappears entirely (Figure 4.2-15). This shows that the Nylon-6 fibers, as a result of the reaction conditions in the gamma irradiation grafting process, had all transformed into a single, more stable, crystalline phase that required more heat (higher ΔH) to melt.

4.2.1.6 – TGA Results

TGA was performed to examine any possible intermediate degradation in the grafted membranes, before main Nylon-6 degradation at 450℃. Intermediate degradation would indicate the presence of another polymer, or molecule within the nanofiber membrane. These results are shown in a representative TGA spectrum in Figure 4.2-16. Overall there were no significant differences between the degradation pattern of these grafted samples, and those of the unmodified Nylon-6. The first degradation drop at 100.43℃ is due to excess water. The degradation range for poly(acrylic acid) is 200℃ – 500℃, and there were no intermediate losses here observed.

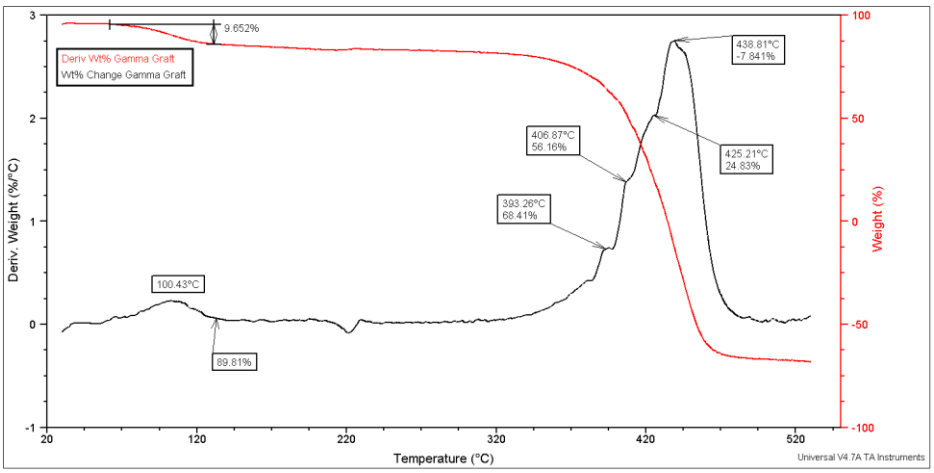

Figure 4.2-16 – TGA spectra of the gamma acrylic acid grafted Nylon-6 sample. Derivative weight change (red) is plotted against the % weight loss (black). Boxes with percents in % weight loss curve indicate how much weight % remains in the sample at certain temperature points.

All membranes show a final degradation step for roughly 90% of the sample mass near 438°C, which belongs to the Nylon. Other than the decrease in degradation temperature, from the original 450°C to now 438°C, there are some small intermediate degradation features near this final degradation maximum. However, these are not significant enough in intensity to assign to a completely separate polymer fragment. Because of the close proximity of these "bumps" at 393°C, 406°C and 425°C to the main degradation at 438°C, it's likely that these "bumps" indicate the degradation of specific crystalline phases that formed during the gamma reaction. Alternatively, if degradation of specific phases occurred, we would expect melting peaks of various Nylon-6 crystalline phases in the aforementioned DSC results. For the grafted samples, the split peak indicting this in the T_m was not present.

4.2.1.7 – Wettability Results

Wettability tests for the grafted membranes were done to see if the moisture absorbance of the electrospun Nylon-6 was affected by either the acrylic acid monomer loading, or the reaction conditions experienced. Changes in wetting would significantly affect how these membranes perform in the salt/water aerosol respiration loading trials. Figure

4.2-17 shows that the gamma grafted membranes were not able to consistently absorb water through capillary action. The mass increase versus time graphs, show primarily noise. This may be consistent with the allover film layer seen in the membrane FESEM images, and the lower measured surface area.

From qualitative observations, the submerged samples absorbed water initially for the first 20 seconds, but decreased rapidly for the next 4 minutes (~250 seconds). The water line that should have increased throughout the length of the sample as water was absorbed instead stalled for those next 4 minutes, before continuing. This trend of initial water absorption, then abrupt stalling, caused the decreasing trend in water absorbance mass seen in Figure 4.2-17. At the stalled points, the water absorbed evaporated giving a negative mass value.

Overall, the gamma irradiation with acidic monomer exposure had the effect of decreasing moisture absorbance in the membranes significantly. Rearrangement of the Nylon-6 crystalline structure explains these results, as well as those of the DSC thermograms.

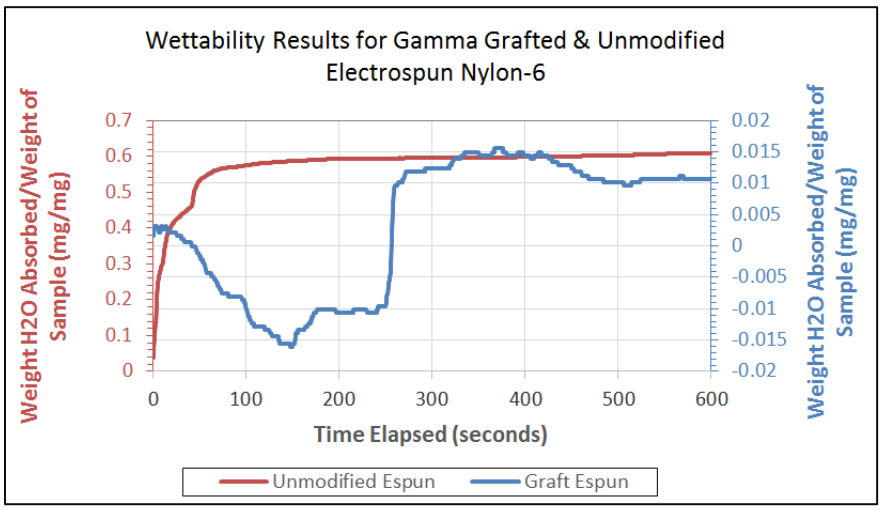

Figure 4.2-17 – Water absorbance wettability tests for an unmodified electrospun Nylon-6 membrane (red) and a gamma acrylic acid grafted membrane (blue).

4.2.2 – Grafting by: EDC [1-Ethyl-3-(3-dimethylaminopropyl)carbodiimide] Coupled Poly(Acrylic-Acid) to Nylon-6 Amine End Reaction

4.2.2.1 – FTIR, FESEM & Macroscopic Results

Polymerized acrylic acid (Mw: 130kD) was coupled with the amine-to-carboxylic acid group linker: EDC [1-Ethyl-3-(3-dimethylaminopropyl)carbodiimide], and reacted with samples of electrospun Nylon-6 membrane. The detailed process of this reaction is shown in Chapter 2, Figure 2-10. Unlike the aforementioned method, which only utilized gamma radiation as the initiation source for activating the acrylic acid monomer, this method used 3 additional components for activation: 1. EDC linker, 2. Sulfo-NHS [N-Hydroxysulfosuccinimide sodium salt], and 3. KH_2PO_4/NaOH buffer solution (pH: 4.7). The roles of Sulfo-NHS and the phosphate buffer were for stabilizing the EDC-carboxylic intermediates to facilitate bonding the Nylon-6 membrane.

The surface modifications of Nylon-6 via EDC/Sulfo-NHS reaction were not found to give neither consistent, nor reliable results showing that effective grafting of poly(acrylic acid) had occurred. The Nylon membranes after EDC treatment sometimes dried too brittle, and at other times, adhered to external surfaces during the drying process. Both situations made their handling difficult for characterization, as can be seen in Figure 4.2-18. Only 3 membranes were characterized for this procedure.

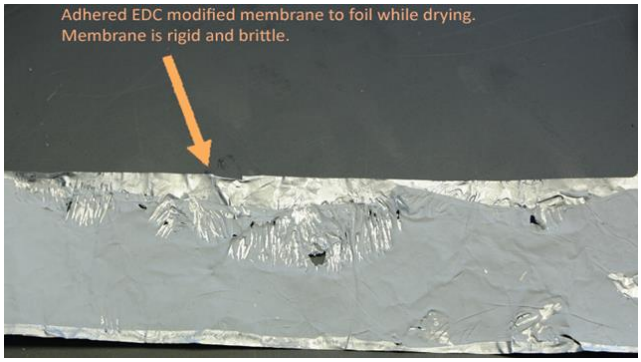

Figure 4.2-18 – Dried Nylon-6 on aluminum foil after modification by EDC reaction. Significant flaking, brittleness, and tearing occurs when removing from foil for characterization.

While the FTIR spectra of the membranes shown in Figure 4.2-19 also exhibit new peaks in the 1700cm^{-1} region, similar to those found in the γ irradiated grafted samples, there are considerable differences in the peak positions and overall absorbance heights. In these results, the new 1700cm^{-1} peak has shifted down from ~1725cm^{-1} (in the γ irradiation data) to 1700cm^{-1}—1714cm^{-1}.

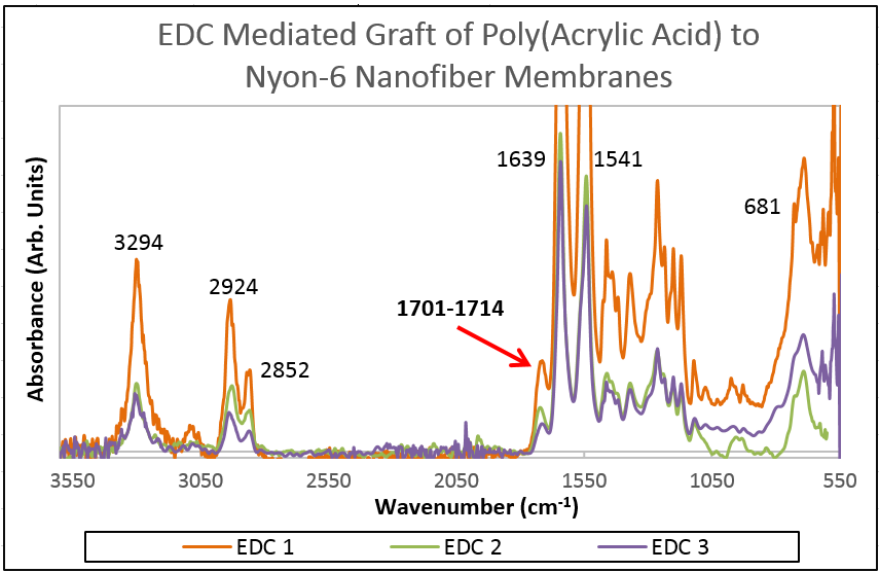

Figure 4.2-19 – FTIR spectra of EDC mediated grafting of Nylon-6 nanofiber membranes with lower wavenumber peak (1701cm^{-1} – 1714cm^{-1}) than expected.

While peaks in the mid 1700cm^{-1} range denote carbonyl stretches from esters and carboxylic acids, peaks in the lower 1700cm^{-1} region are also indicative of conjugated acid groups. However, this wavenumber region is also usually more commonly associated with unsaturated ketones and amides, rather than carboxylic acids or esters.[114, 121] It's unlikely that the shift in the Nylon membranes was due to the formation of α,β unsaturated ketones during the grafting process, but it's possible that intermediate impurities containing various carbonyl and unsaturated groups influenced the downward wavenumber shift. EDC itself is a carboiimide structure with form shown in Figure 4.2-20. After binding to a carboxylic acid group, and exposure to Sulfo-NHS, a new stable intermediate is formed.

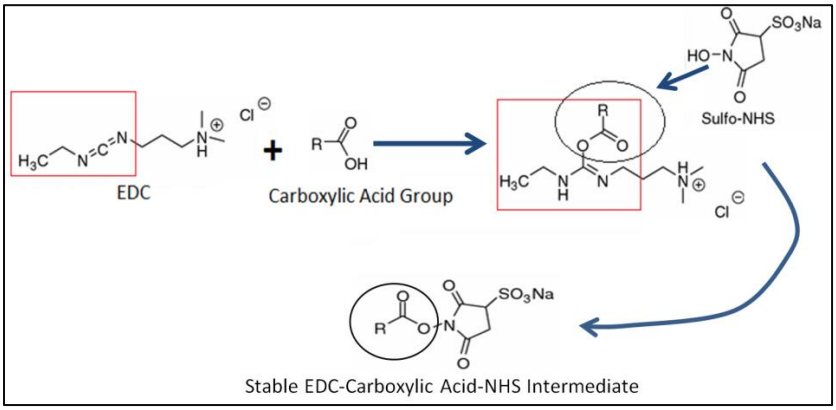

Figure 4.2-20 – Conversion of EDC-Carboxylic Acid Complex to Stable NHS Intermediate before grafting to amine (Nylon-6).

This process occurs before the introduction of the amine containing compound, in this case, the electrospun Nylon-6. In this grafting approach, intermediate molecules are not removed, and it's assumed that all intermediates will either be successfully grafted to the target amine, or re-dissolved into their original forms (trace EDC, NHS, and carboxylate ions) to be removed by thorough membrane washing. As will be discussed further, from FESEM and TGA analysis performed, the removal of impurities from the membranes through deionized water washings was not a guaranteed process.

However, another reason explaining the inconsistent absorbance heights, Figure 4.2-21, and shifted ester/carboxylic acid peaks for the FTIR spectra of EDC reacted membranes, comes from the nature of the reaction mechanism itself. EDC mediated grafting almost exclusively occurs with primary amine groups. In Nylon-6, these groups would only occur at the end chains of the polymer. Thus, reaction sites for this type of addition are far more limited than they would be for a free radical based reaction, as the one occurring for the γ radiation process, for instance.

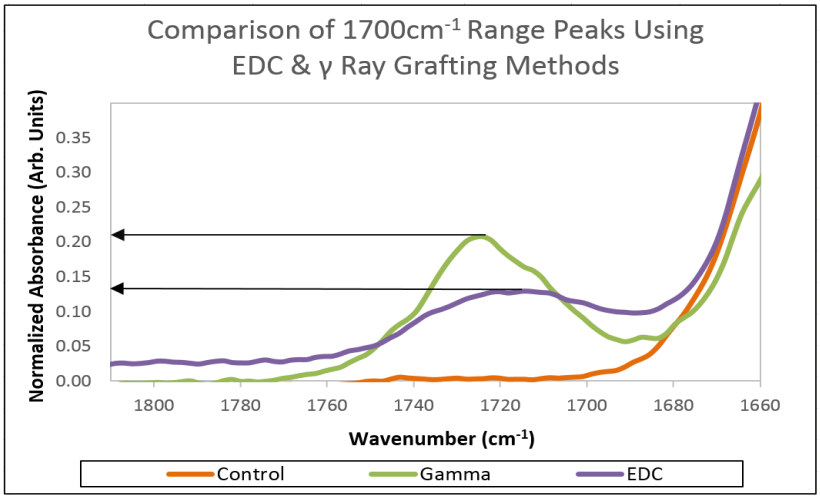

Figure 4.2-21 – Comparison of normalized absorbance heights of grafted electrospun Nylon-6 membranes using 2 methods: EDC mediated & gamma radiation induced, against an unmodified control sample.

Furthermore, in electrospun Nylon-6, there is already a preferred orientation of the polymer chains along the nanofiber length.[106] This suggests that amine end groups would only be most abundant at the ends of the fibers. However, since electrospun membranes are comprised of continuous filaments originating from the needle tip source, the number of actual filament ends containing the polymer chain ends would also be reduced again, unless the filaments are broken. Macroscopic images of the Nylon membranes while in the EDC/Sulfo-NHS reaction vials show that tiny white fibrils of possible poly(acrylic acid) only attach to the corner edges of the nanofiber membranes, Figure 4.2-22, and not the center top or bottom surfaces.

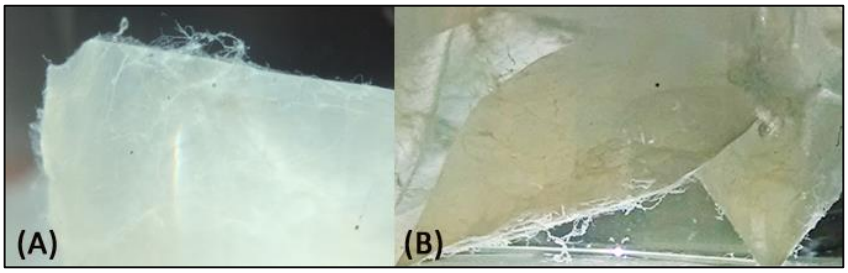

Figure 4.2-22 – Macroscopic view of developed fibrils on the corners of membranes (top edge – A; bottom edge – B) undergoing EDC amine-carboxylic reaction grafting.

A comparison of the FTIR peak heights for the 1700cm^{-1} carboxylic acid, against the carbonyl-amide peak is shown in Table 4.2.6A. Additionally, the normalized comparison of

the 1700cm^{-1} peak to the average amide height in the standard control samples is shown in Table 4.2.6B. For the EDC mediated grafted reaction, there is roughly 10.1% $\pm$ 4.2% chance of new ester/carboxylic acid peak formation in the 1700cm^{-1} region. As expected, from the decrease in graft sites available for this method, it is about 6.7% less likely to occur than for the γ mediated reaction from above. In comparing the increase in new peak formation to the original heights of the carbonyl-amides in the control samples, there is 14.2% peak increase possible. The error is larger than the average, indicating that this method produces inconsistent absorbance heights for this 1700cm^{-1} peak range, unlike the γ method. Overall, the EDC method shows less likelihood for new FTIR peak formation from grafting to take place.

Comparison of 1700cm-1 Graft Peak Height with Carbonyl (C=O) Absorbance Heights within Sample					
# Sample	Graft Peak (Absorb.)	C=O Amide (Absorb.)	Ratio of Absorb.	Ratio (%) of Absorb.	
1	0.004	0.0420	0.0952	9.524	
2	0.0127	0.1063	0.1195	11.947	
3	0.004	0.0460	0.0870	8.696	
(A).				10.056	Avg
				4.198	Err (95%)
				1.690	St.De

Comparison of 1700cm-1 Graft Peak Height w/ Average Carbonyl (C=O) Absorbance Heights From Standards					
Avg. C=O Normalized Absorb. From Standards	# Sample	Normalized Graft Peak (Absorb.)	Ratio of Absorb.	Ratio (%) of Absorb.	
0.7313	1	0.1260	0.1723	17.230	
	2	0.0510	0.0697	6.974	
	3	0.1340	0.1832	18.324	
(B).				14.176	Avg
				15.553	Err (95%)
				6.261	St.De

Tables 4.2.6 – Ratio of new graft peak height at 1700cm-1 to carbonyl amide peak height in the EDC grafted sample (A) (pink box), and the ratio of the new graft peak height to the standard average Carbonyl Amide height (B) (green box). The chance of grafting is ~10%, and the probable new graft peak height increase is ~14% (but is highly variable).

Representative FESEM images of the EDC grafted Nylon-6 membranes are shown in Figure 4.2-23. Despite having been washed and soaked in deionized water to remove excess trace amounts of unreacted EDC, Sulfo-NHS salt, monopotassium phosphate (KH_2PO_4)/NaOH buffer, and unattached poly(acrylic acid), the samples still dried containing a large amount of

impurities. Though there was still a significant amount of charging from the sample during SEM imaging, even after carbon coating, the impurities are directional needle-like crystal shards distributed throughout the membrane surface seen as far as 20 µm - 100µm away. The brittle-like nature of the membranes and the altered glossy, shiny appearance post drying can be attributed to these residues that remain. Figure 44 shows that the shards can be as large as 4µm in width, but much longer than 40 µm in length. The shards appear to be attached to single Nylon nanofibers, and look as if they grew from the center of the membrane surface.

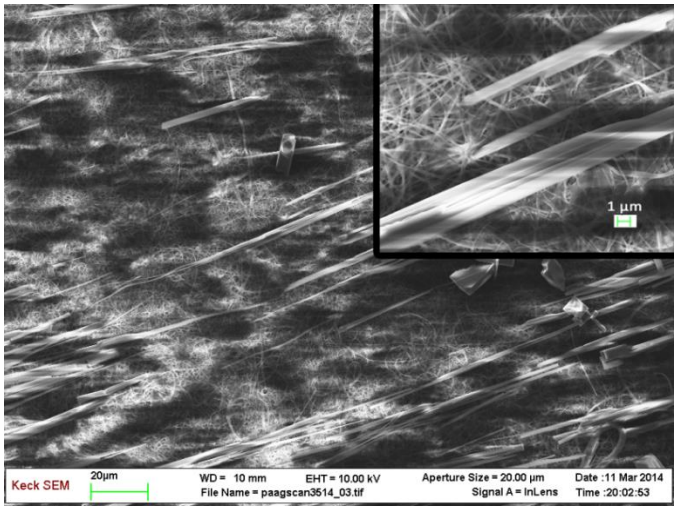

Figure 4.2-23 – FESEM images showing crystal residue on EDC/Poly(acrylic acid) grafted membranes post washing.

EDX analysis on the membranes confirms that they still contain potassium residue from the buffer solution, Figure 4.2-24. No energy counts indicating sulfur compounds were detected, therefore, extraneous residues of Sulfo-NHS were likely washed off.

4.2.2.2 – TGA Results

Considering that potassium phosphate is a basic crystal salt at room temperature, and that it recrystallizes quickly after melting to form a dense solid, from the TGA graph in Figure 4.2-25, these crystal shards in the SEM images are the likely the origin of the

potassium energy counts seen in the EDX spectra. Poly(acrylic acid) does not, and neither does its sodium salt, crystallize into rigid, brittle needle-like solids. Furthermore, in aqueous solutions, poly(acrylic acid) easily dissolves, increasing the solution's viscosity to a gel-like consistency.[129]

Hydrogels and other gel-like solutions from poly(acrylic acid) can be easily made due to its high moisture regain properties. This can be one reason why some of the poly(acrylic acid) EDC grafted Nylon membranes also adhered to the foil they were drying on post washing.

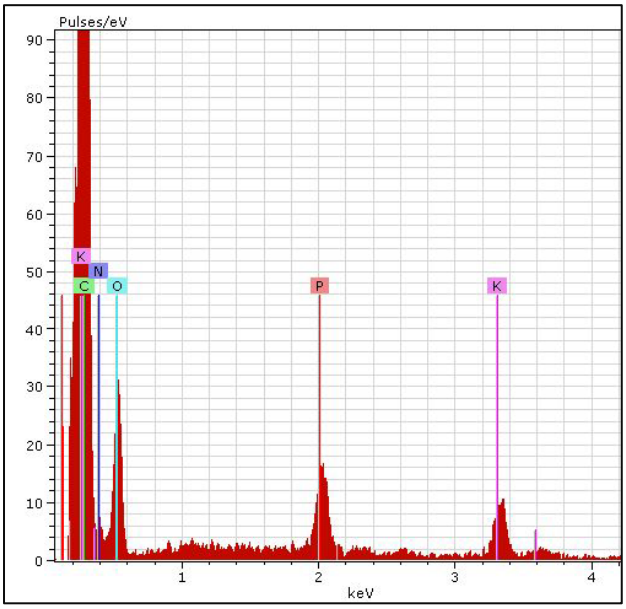

Figure 4.2-24 – EDX spectra of potassium phosphate salt (KH_2PO_4) residue remaining on washed EDC-Poly(acrylic acid) reacted nanofiber membranes. Markers for potassium & phosphorous elements are shown in purple & red, respectively.

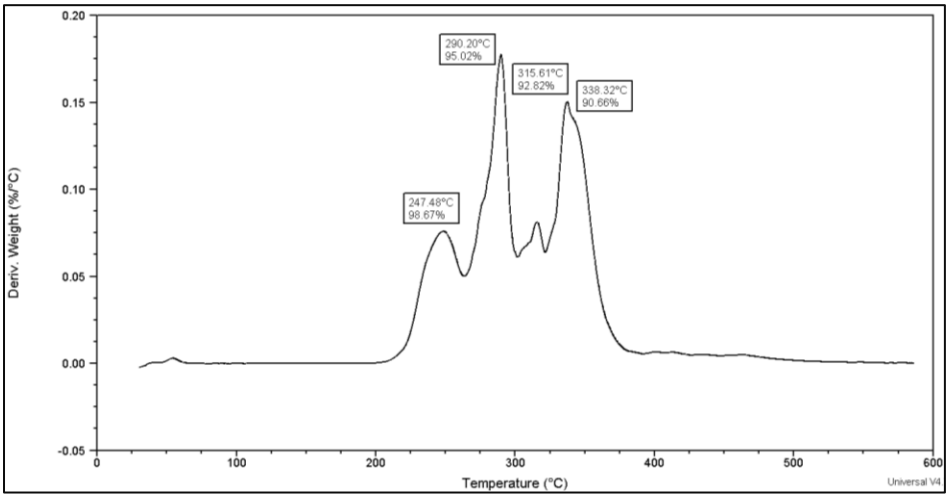

Figure 4.2-25 – TGA derivative weight % loss spectra of KH2PO4 pure crystal. Weight loss is shown in the boxes at specified temperatures.

The TGA thermograms of the washed and unwashed membranes are shown in Figure 4.2-26. From the TGA spectrum of KH_2PO_4 crystal alone, Figure 4.2-25, there are significant degradation points between 200℃-400℃ which account for some of the stray peaks seen in the unwashed EDC reacted samples in Figure 4.2-26. To also complicate matters, the degradation region of poly(acrylic acid) begins near 220℃.[130] Once the sample is washed, the stray degradation at 188℃ disappears entirely, and only weight losses near 400℃ are present. It's possible these small peaks are due to Nylon fragmentation.

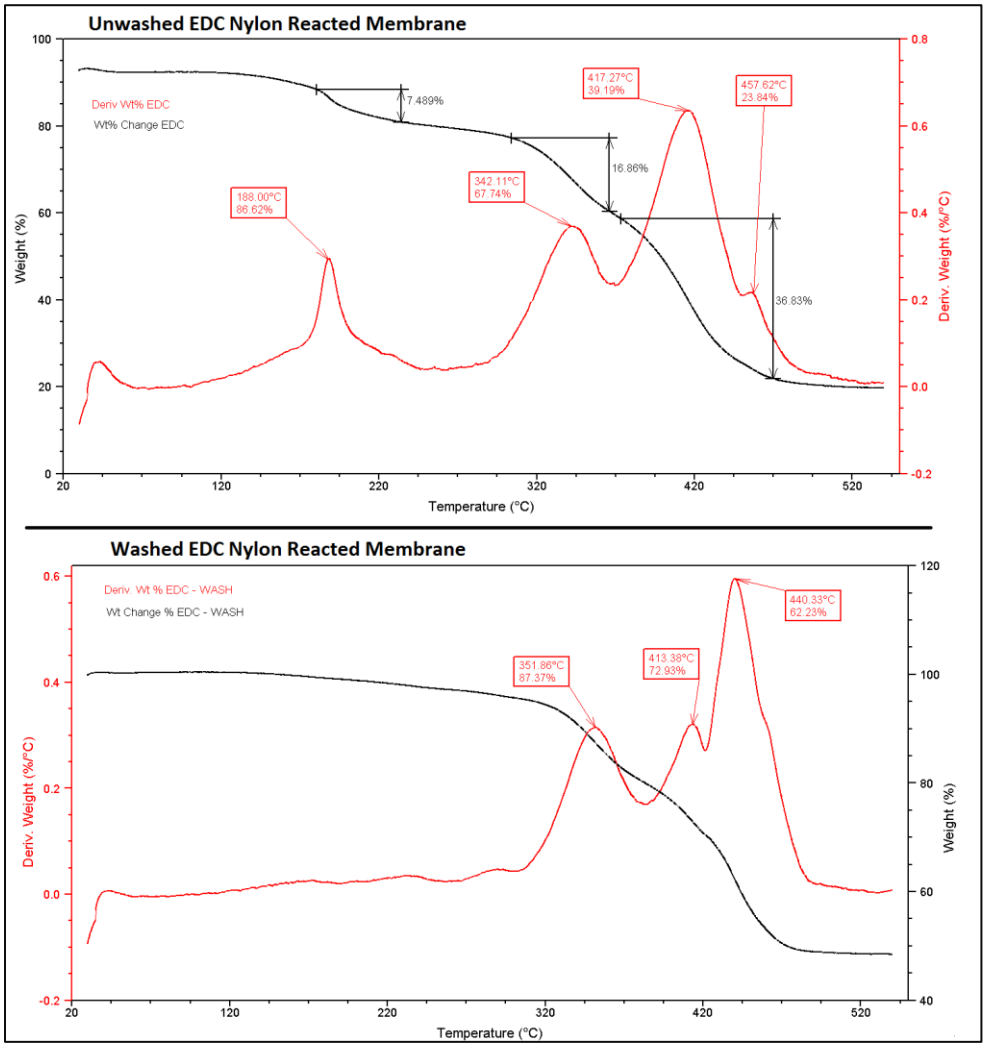

Figure 4.2-26 – TGA spectra of EDC/Poly(acrylic acid) reacted Nylon-6 electrospun membranes that were unwashed (top) and washed (bottom).

4.2.3 – Conclusions for Both Physicochemical Grafting Methods

The conclusions of the EDC chemical mediated & mutual gamma irradiation exposure methods for facilitating polymer grafting and surface modification of already electrospun Nylon-6 nanofibers is shown in Table 4.2.7.

Some final recommendations would be that: Gamma irradiation for grafting polymers is best for applications needing membranes with increased surface functionality/texture, and small pore sizes. Thermal properties of the Nylon-6, seen through

DSC also show increased heat tolerance (ΔH).

EDC is best used for exclusively reacting films or membranes, known to contain a precise number of amine end groups, with a carboxylic acid containing polymer. Or, it is also good for creating an intermediate layer connecting a membrane with a carboxylic containing compound directly with zero additional monomer length in between.

Gamma Irradiation for Nylon-6 Nanofiber Membrane Grafting or Surface Modification	
ADVANTAGES	**DISADVANTAGES**
1. Ease of process. Requires only loading sample in irradiation chamber and setting time desired for exposure. Radioactive isotope degrades 1 unit per 1 – 1 ½ years. Increased time exposure can make up for lowered initial gamma ray intensity (Requires source of gamma irradiation, which can be difficult to obtain.♦)	**1. Competing reactions exist.** Rate of grafting/polymer attachment process to nanofiber membrane vs. Rate of de-polymerization of the nanofiber membrane for prolonged gamma exposure times (≥20minutes at high intensity units)
2. Shows significant results of visible and quantitative grafting/polymerization via SEM & FTIR spectroscopy. FTIR spectra show consistent amount of grafting is possible per membrane (17%-20% chance of new carbonyl peak formation & overall 9% membrane weight increase.)	**2. Samples are sensitive to water vapor.** After a prolonged time (~1 month), FTIR spectra show loss of acrylic acid peak. This may just be a consequence of the polymer chosen for grafting, however.
3. Samples can be easily handled post irradiation. Fiber membranes maintain their structure; are not brittle, too thin, or greasy.	**3. Shrinkage of membranes post irradiation.** Smaller pore size in membrane, and meshing of fibers occurs.
4. More sites for attachment on the backbone chain are possible (due to radical polymerization). This process can enhance the membrane structure for attaching multiple functionalities (other polymer types). Crosslinking capabilities can also be explored.	
5. Due to pore shrinkage increased capture is possible, from results of the Cascade Impactor aerosol dispersal trials.	

♦ However, irradiators are becoming increasingly common in vet schools/biochemistry related fields for studies involving tumor growth in animals. On the Cornell University campus, there are 3.

EDC (Coupled Sulfo-NHS) Crosslinking Molecules for Amine End Group Grafting	
ADVANTAGES	**DISADVANTAGES**
1. No membrane shrinkage post washing or drying. No fiber coagulation.	**1. Minimal & inconsistent loading.** 5% - 6% less loading of poly(acrylic acid) possible than for gamma irradiation grafting process (based on FTIR). Absorbance peak heights for poly(acrylic acid) seen are largely variable per sample.
2. Membranes are not water moisture/humidity sensitive after prolonged periods of time.	**2. Costly EDC reagent. EDC - $46/10mg** (Although, only 1-3mg of EDC are used But multiple trials can get expensive)
	3. Must maintain reaction conditions & store reagents in regulated conditions to avoid degradation. (EDC: -20°C ; Sulfo-NHS: 4°C; reaction must be done in inert atmosphere to avoid moisture)
	4. Requires two-step grafting process. (A): React EDC with Sulfo-NHS in buffer solution with polymer to be grafted. (B): React (A) with the amine containing polymer/substrate.
	5. Requires creation of buffer solution that contains no carboxylic acid or amine/amide components at pH≅4.6 – for EDC-carboxylic acid complex to form. (Often potassium phosphate buffer is used)
	6. Phosphate buffer leaves brittle salt residue on fiber membrane even after repeated H_2O & MeOH washings.
	7. Process is only exclusively for carboxylic acid group-to-amine group reaction.

Table 4.2.7 - Advantage and Disadvantages to both surface modifications: gamma grafting & EDC grafting processes, on nanofiber membranes.

4.3 – AEROSOL CAPTURE RESULTS

An aerosol of NaCl was generated, and dispersed by the simulated breathing apparatus (SBA) (Figure 3-9), towards various membrane filter types to measure their capacities for capturing the aerosol droplets. Three distinct modes of operation for the SBA were used to disperse and capture the aerosol. These three modes of operation are shown in Figures 4.3-1A,B and Figure 4.3-2.

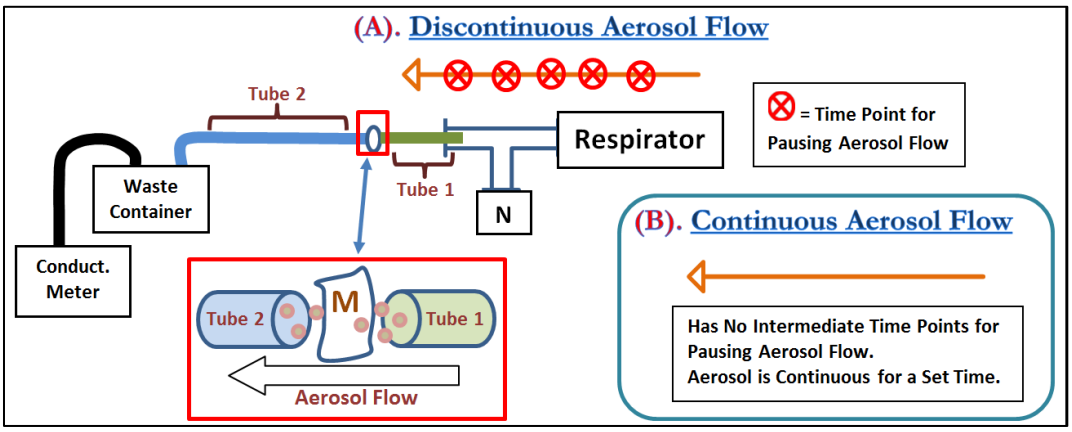

Figure 4.3-1A,B – Discontinuous and Continuous aerosol flow operating modes for the SBA. A membrane to be used for capture is placed between Tubes 1 and 2. The end of Tube 1 leads into a waste container containing deionized water, and a conductivity probe attached to a meter. The discontinuous aerosol dispersal mode means that the apparatus will be stopped at various time intervals to monitor the change in conductivity of the waste container. The continuous dispersal mode does not stop the aerosol flow at specific time intervals.

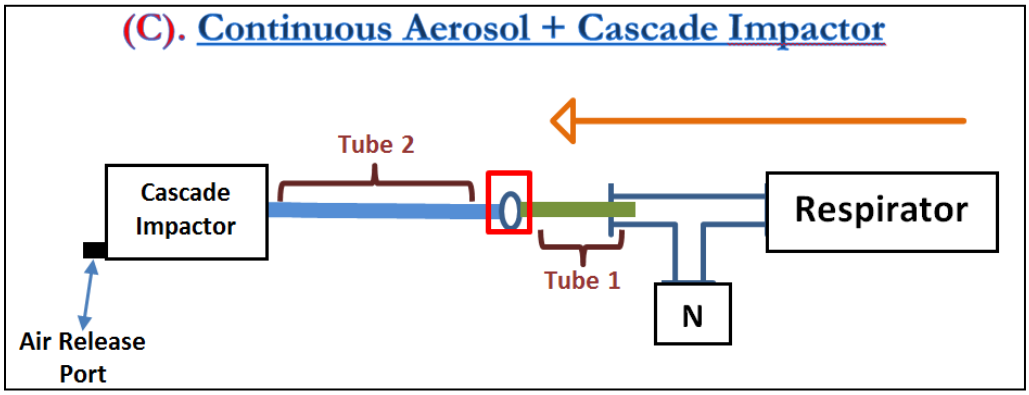

Figure 4.3-2 – Continuous air flow scheme with cascade impactor attachment at the end. The aerosol is dispersed for 25 minutes, and allowed to run continuously for membrane capture (red box). The waste droplets are collected, by size, between 21μm – 0.5μm, and concentration.

These first two modes of operation (Figure 4.3-1A,B) rely on the principle of conductivity changes as the aerosol droplets are absorbed by the membranes. The third mode of operation (Figure 4.3-2) measures a change in the particulate weights captured, and relies on the use of an 8-stage cascade impactor.

4.3.1 – Descriptions of the 3 Aerosol Dispersal Modes for the SBA [Mode 1: 45 Minute Discontinuous Aerosol Loading, Mode 2: Varied Time Continuous Aerosol Loading, Mode 3: 25 Minute Continuous Aerosol Loading with Cascade Impactor]

In the 1st mode of operation, Figure 4.3-1A, the dispersal of aerosol is "discontinuous". Each membrane for these experiments was exposed to a salt aerosol for a total of 45 minutes discontinuously. To document the waste container conductivity change at specific time points within this time frame, the compressor and respirator were paused, and any aerosolized particles allowed to settle in the waste container until the conductivity meter signaled "Ready" (usually after 30 seconds). The conductivity measurement was taken, and the apparatus was resumed until the next measurement point. Measurements were taken at 5 time points: 5, 15, 25, 35, and 45 minutes. This process was repeated at least three times per membrane to determine how the changes in pressure (due to pausing the breathing apparatus), and various aerosol exposure time intervals, would affect the total amount of aerosol captured onto the membranes, as well the amount of aerosol passing through the membrane to the waste container.

The hypothesis here is that for the electrospun membranes, with small pore size, and large surface area, most of the salt aerosol will be captured on the membranes and very small or no changes in the waste conductivity will be observed. For the filter membranes with large pores, such as a sample of polyester chiffon fabric (Figure 4.3.-4), more salt would pass through and larger increases in the conductivity of the waste water would be observed.

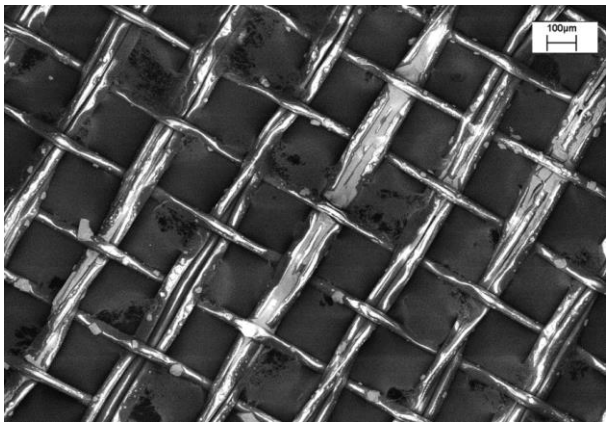

Figure 4.3-4 – Greater than 100μm sized pores for a membrane sample of woven polyester chiffon fabric used in aerosol capture studies.

For the 2nd mode of operation, seen in Figure 4.3-1B, the dispersal of aerosol is "continuous". Each membrane for these experiments was exposed to a continuous amount of aerosol generated from the nebulizer for various set periods of time (15 minutes, 45 minutes, or 90 minutes) without pausing the breathing apparatus. Here, rather than observing the aerosol capture between time intervals, the aerosol capture for a membrane, for a specified long duration of time was observed. This mode of operation was used to examine the ultimate capacities for membrane aerosol loading, and to see if any membrane deterioration occurred in the process.

The membranes from these trials were analyzed using EDX spectroscopy for increasing salt particle content. One hypothesis was that increasing time periods of continuous aerosol exposure would result in larger salt particle concentrations detected on the surface. These EDX results are discussed further within this chapter.

In the 3rd mode of operation, Figure 4.3-2, the dispersal of aerosol is "-continuous-" with the 8-stage cascade impactor attachment introduced in Figure 3-2. The cascade impactor serves two analysis functions. First, its use was for capturing the remaining aerosol passing through membranes so that a concentration of particles lost, and relative size range of these particles lost could be determined.

The substrates in the cascade impactor are different from the main capture testing membrane in the center of the SBA. This is to facilitate non-turbulent flow of the aerosol droplets in a cascade motion throughout each stage evenly. Eight substrates, laser-cut from laboratory grade ParafilmTM, were each fitted to the eight stages in the impactor (Figure 3-2).

The aerosol passing through the main membrane, held at the junction between Tube 1 and Tube 2, Figure 4.3-2, enters the impactor. From there, the aerosol droplets would be separated based on size and accumulate on their corresponding stages. The stages range from 21.3 μm to 0.52 μm (520 nm), with the 0.52 μm stage being the last stage in the series.

Figure 4.3-3 in the Appendix shows an example data table worksheet from the manufacturer for how each substrate weight change relates to the particle size captured for the designated cut-point stage. It relies on Stoke's Number relations and the Cunningham Slip Correction Factor considerations for small particles flowing through fluids.[131, 132]

All three modes of the SBA operation, however, were subject to the same nebulizing parameter conditions. These conditions are outlined in Table 4.3.1.

SBA Chosen Operating Parameters for All Nebulizations				
Pressure:	6 - 7 PSI	(Respirator + Compressor)		
Initial Nebulizing Solution	Conductivity:	231.1 µS/cm	Concentration:	64.1 mg/mL
Respirator:	10 Breaths/Min			
	150 mL Air Volume			
	50 : 50 (Inhalation : Exhalation)			

Table 4.3.1 – The operating conditions for the SBA. It shows the amount of pressure the aerosol is dispersed at, the respiration exhalation breaths/min, and total air volume parameters. The initial nebulizing solution conductivity was measured at 231.1μS/cm which is equivalent to 64.1mg/mL of salt concentration using the conductivity vs. concentration curve. This calculated concentration value was equivalent to the total stock concentration value from which the nebulizing solution was taken. It shows that concentration vs. conductivity curve is valid.

The optimization process for deciding which final nebulizing conditions to use, were based on the performance of the 3 Nylon-6 standard membranes electrospun exposed to

various pressures of aerosol from the apparatus.[β] If the nebulizing parameter chosen, for instance, breathing rate: 40 breaths/min at 150cc tidal breath volume, caused the membrane to immediately break during the exhaled aerosol capture, a parameter was reduced, (example: breathing rate was too fast), until the membrane did not instantly rupture. In this way, the capacity for loading each membrane filter type with the aerosol could be fairly assessed, starting with the thinnest materials first: the electrospun membranes.

4.3.2 – Relationship between Salt Conductivity & Concentration for the Aerosol Conductivity Capture Results

To convert from aerosol conductivity to aerosol concentration, a standardized NaCl conductivity to concentration curve was compiled. These curves are shown below in Figures 4.3-5 and Figure 4.3-6. Normally, increasing conductivities of ionic solutions do not follow a linear trend with increasing content concentration.[133, 134] Non-Linear concentration/conductivity trends occur with alcohols and strong acids because their ions dissociate in water quite easily.[134]

Initially, the conductivity measured will increase with increasing salt concentration. However, at maximum concentrations, the measurements eventually reach a plateau point. Before this, the conductivity begins to fluctuate because the large quantities of ions dissociated in water are not all able to migrate between the probes of the conductivity meter at once. This can lead to conductivity responses that erratically increase, or decrease. Therefore, a linear relation between conductivity and concentration cannot be accurately made. Eventually after the solution becomes super-saturated with ions, the conductivity

[β] This membrane was: Standard Espun Membrane #1 (10CM NSM) shown in Chapter 4.1, Figure 4.1-9. For reference, the three unmodified electrospun Nylon-6 nanofiber membranes were spun on the rotating drum with the following distinctive features: #1. 10CM Distance, No Sliding Mechanism (10CM NSM), #2. 10CM Distance, With Sliding Mechanism (10CM SM), and #3. 12.5CM Distance, With Sliding Mechanism (12.5CM SM).

response will flat line. The same phenomenon occurs when conductive nanoparticles, such as carbon nanotubes, are inserted into various polymer composites as well.[135]

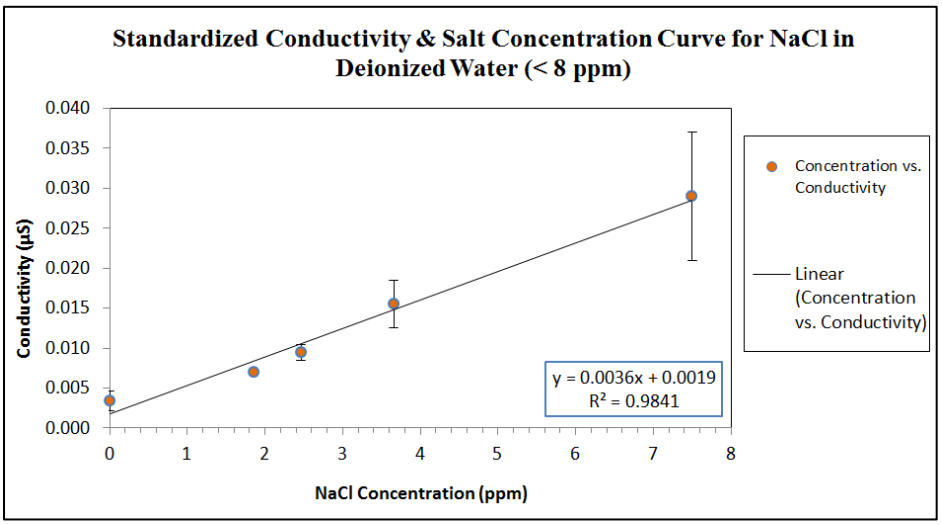

Figure 4.1-5 – Linear trend of conductivity increasing with salt (NaCl) concentration for salt concentrations less than 8ppm in deionized water.

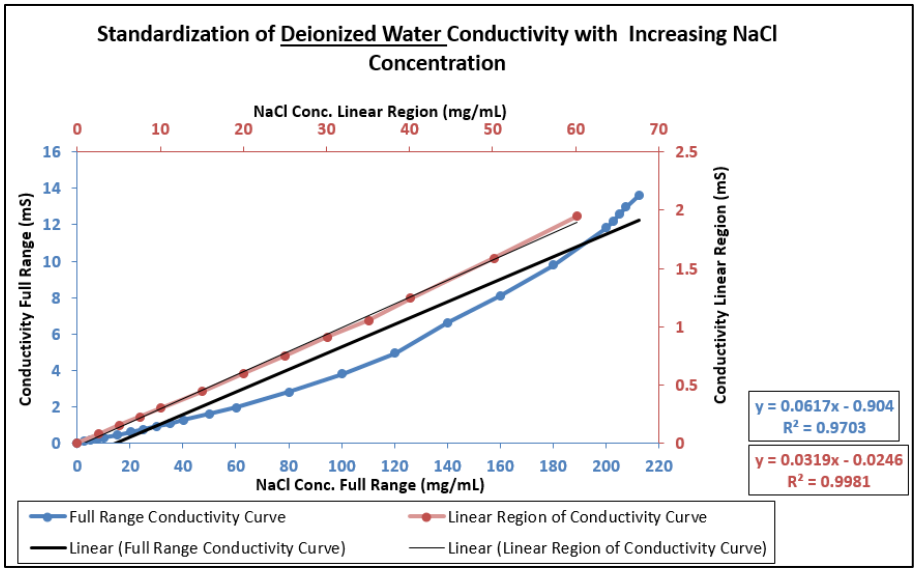

Figure 4.3-6 – Approaching non-linear trend of conductivity increasing with salt concentration once salt concentrations reach 10^5 ppm (or, 100mg/mL) [blue line]. The linear relationship still holds at 10^4 ppm (or, 60mg/mL) [red line].

However, in this study, for small changes in simple NaCl solution concentrations, less than 8 ppm (8.0×10^{-3} mg/mL), and those increasing towards 110 ppm (0.10 mg/mL) when in

deionized water, a linear trend is observed, Figure 4.3-5. Even when the concentrations of salt are increased to 6.0 x 10^4 ppm (60 mg/mL), the linear conductivity trend still holds (Figure 4.3-6). As expected, for a relatively weak electrolyte such as NaCl, the linearity only begins to decrease when 10^5 ppm (100 mg/mL) concentration in the solution is met.

For NaCl ionic solutions in distilled water, the conductivity measured begins to deviate from linearity almost instantaneously at 100 ppm (0.10 mg/mL) (Figure 4.3-7). This is due to the interactions between other types of ions present from even distilled water.

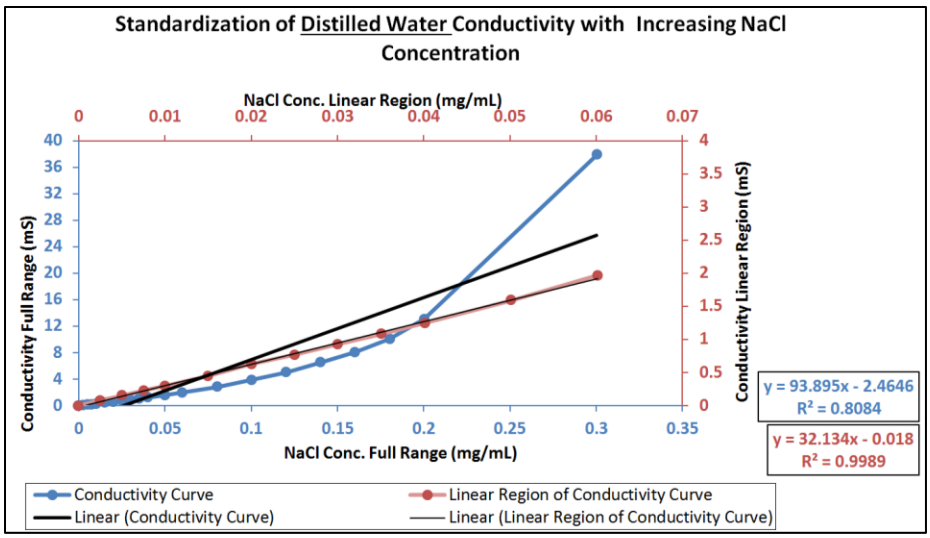

Figure 4.3-7 – Extreme deviation from linearity for conductivity versus concentration curve when salt is dissolved in distilled water. This deviation from linearity occurs before the super-saturation plateau point.

4.3.3 – Calculations for Concentration of Aerosol Captured by Membranes in SBA

For this study, since only small amounts of aerosol were captured in the waste container at the end of the SBA trials, Figure 4.3-5 was the only trend used for converting concentration to conductivity. Relative aerosol droplet sizes were determined to be mostly between 500nm – 14µm in size, from aerosol collection trials using the cascade impactor. The equations used for calculating the concentration of aerosol capture in the center of the membranes held in the SBA were as follows:

$$x_{NConc.} = X_{WConc.} = \left(\frac{Y_{Conduct.} - 0.0019}{0.0036}\right)/p, \ \{\text{where } p = 10001.14 \text{ ppm per 1 mg/mL}\} \quad (4.3.1)$$

$$M_{Capture} = X_{NConc.} - X_{WConc.} - E_{SBA} \quad (4.3.2)$$

$X_{NConc.}$ and $X_{WConc.}$ of Equation 4.3.1 refer to the calculated salt concentration in the nebulizing bulb, and the waste container of the SBA seen in Figure 3-4C and Figure 3-10, respectively. $X_{NConc.}$ and X_{WConc} are made equivalent in Equation 4.3.1 because they are calculated using the same equation. X_{NConc} had an average NaCl concentration of 64.1mg/mL for all aerosol nebulizing trials performed. Equation 4.3.1 is determined using the linear fit curve derived from Figure 4.3-5, solving for concentration in ppm of salt solution. To make the values more conceptually intuitive, the concentration values are divided by the conversion constant "p"; where "p" converts ppm to mg/mL.

To indirectly determine how much aerosol concentration was captured by the membrane placed in the center of the SBA, Equation 4.3.2 is used. Here, the amount of aerosol potentially captured ($M_{Capture}$) is the difference between the initial starting concentration of nebulized aerosol ($X_{NConc.}$), and the new concentration of aerosol accumulated in the waste container ($X_{WConc.}$). The additional error factor (E_{SBA}) is also subtracted from the final calculation of membrane aerosol capture. E_{SBA} accounts for the potential loss of aerosol mist concentration within the simulated breathing apparatus tube manifold itself before reaching the water in the waste container. This error is approximately 15.01mg/mL ($\pm$3.09mg/mL). It was found by nebulizing aerosol without the membranes for capture inserted into the SBA.

4.3.4 - Aerosol Capture on Membranes from SBA Dispersal Mode 1 (45 Minute Discontinuous) & Conductivity Change Measurements

Figure (4.3-10) shows the final set of membrane filters used for capture in the SBA. It includes the mutually gamma irradiated samples of Nylon-6 with acrylic acid grafted on the

surface, the commercial cellulose filter paper, and the polyester chiffon fabric with large pores.

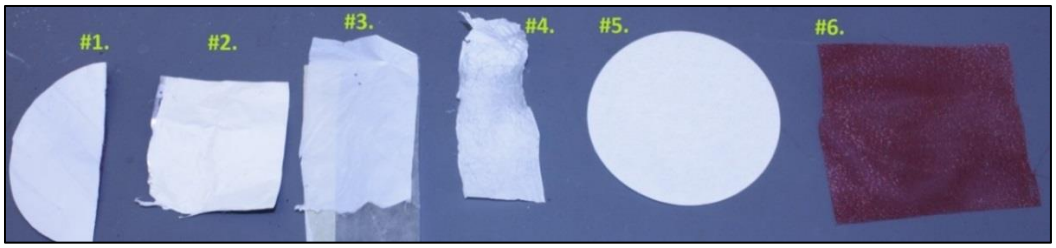

Figure 4.3-10 – The final 6 membrane types used for aerosol capture experiments: #1). E.Spun 10CM NSM (No Slide Mech); #2). E.Spun 10CM SM (With Slide Mech); #3). E.Spun 12.5CM SM (With Slide Mech); #4). γ-Gamma Acrylic Graft; #5). Commercial Filter Paper (Cellulose); #6). Chiffon Fabric (Polyester).

Figure 4.3-8 shows an example of the conductivity data accumulated for the 45minute interval trial runs using the commercial cellulose filter paper. Here, the conductivity is documented for each interval and the total conductivity change collected in the waste container is converted to a concentration which is then put through Equation 4.3.2 for the final salt concentration per membrane captured. For the commercial filter paper, which does not rupture during the aerosol capture process, up to 54mg/mL of salt aerosol can be collected, if the errors of the apparatus function are not factored in. Figure 4.3-9 and Figure 4.3-11 compare the performance of the commercial cellulose in the SBA to that of the electrospun membranes and the chiffon fabric, in terms of how much waste aerosol is observed.

	Time Elapsed (Min)	TRIAL 1 ΔConduct. (μS)	TRIAL 2 ΔConduct. (μS)	TRIAL 3 ΔConduct. (μS)	Avg. Broken ΔConduct. (μS)
	0	0	0	0	0
	5	0.003	0.016	0.026	0.021
	15	0.009	0.032	0.042	0.037
	25	0.011	0.017	0.029	0.023
	35	0.008	0.044	0.043	0.0435
	45	0.007	0.058	0.036	0.047
	Observations	No Break	Break	Break	
Final Conduct. In Waste (μS)		0.038	0.167	0.176	0.172
Final Conc. in Waste (mg/mL)		10.028	45.861	48.361	47.111
Memb.Conc. Captured (mg/mL)		54.082	18.248	15.748	16.998

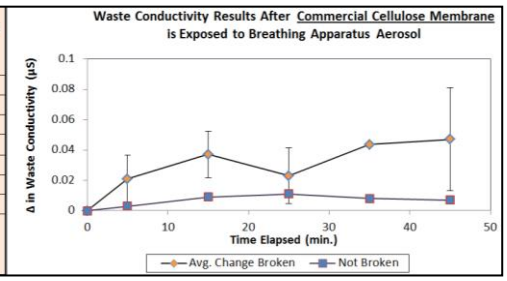

Figure 4.3-8 – Example of data compilation gathered from one 45 minute trial run of dispersed salt aerosol through the SBA using the commercial filter membrane as a capture device. Change (Δ) in measured conductivity from the waste container is shown in the tables. The observations for whether the membrane broke, or not, during aerosol capture is listed. Conversions of waste final conductivity change to concentration, and associated concentration captured on membrane are

listed (yellow highlight). Graphs of average conductivity waste change for the broken and unbroken membranes are separately shown.

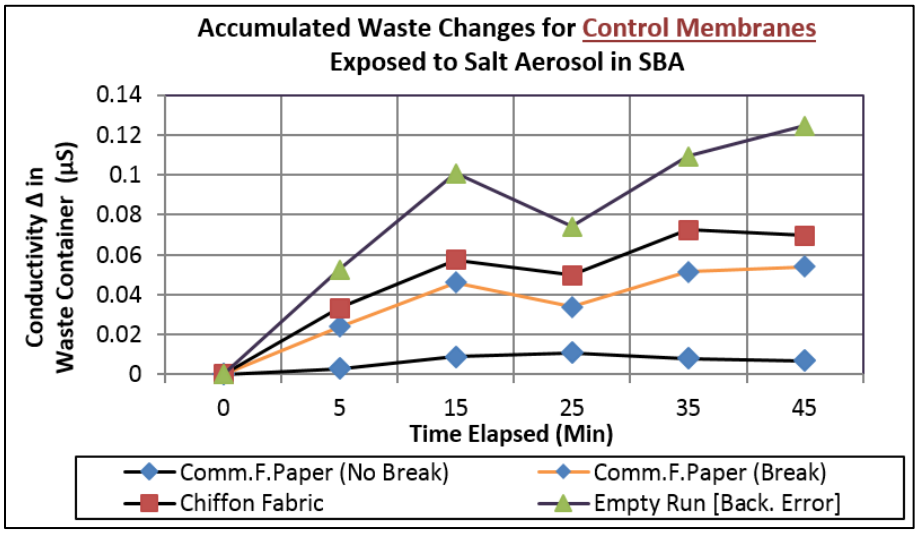

Figure 4.3-9 – Graphs showing all conductivity waste change averages for the control membranes and no membrane in SBA during 45 minute trial discontinuous aerosol dispersal. Separate graphs for membranes which broke and did not break during aerosol capture were accounted for.

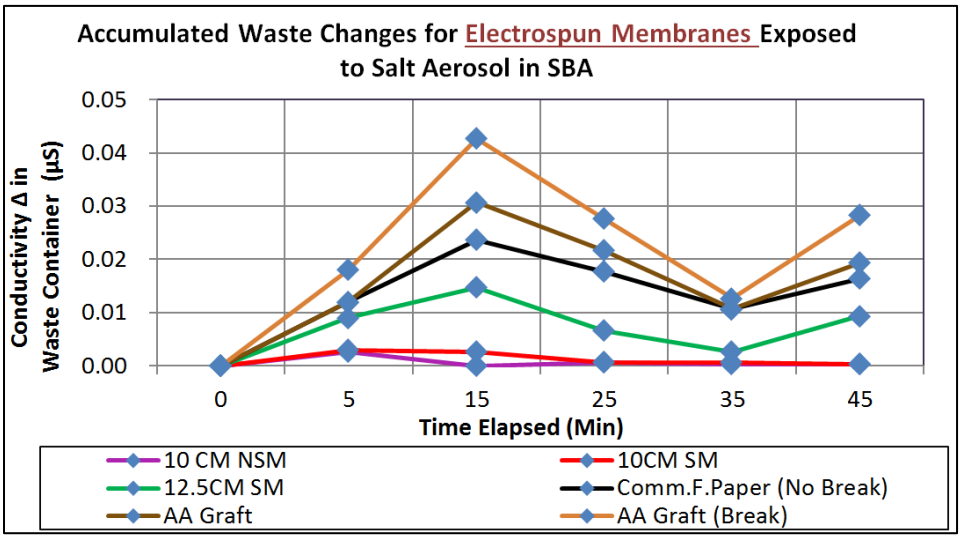

Figure 4.3-11 – Graphs showing all conductivity waste change averages for the electrospun membranes and gamma irradiation grafted electrospun membranes (AA – Acrylic Acid graft) during 45 minute trial discontinuous aerosol dispersal. Separate graphs for membranes which broke and did not break during aerosol capture were accounted for. A comparison to the commercial filter paper trial, which did not break, is shown in black.

One significant observation in Figures 4.3-9 is that while the commercial filter paper does show less aerosol loss than the chiffon fabric, the filter paper is highly susceptible to

rupture during the capture process (orange line). When it does rupture, its capture efficiency decreases, and the amount of aerosol lost to the waste container becomes similar to the amount lost for the chiffon fabric. The commercial filter papers, on average, rupture more than half of the time during the aerosol capture experiments.

Compared to the electrospun membranes in Figure 4.3-11, even the unbroken commercial filter paper shows higher aerosol loss. Electrospun membranes spun on the drum at 10cm with and without the axial sliding mechanism (SM & NSM – purple and red) show little or no lost aerosol throughput into the waste container at the end of the discontinuous trial runs. Like the commercial filter papers, the grafted samples, too, are susceptible to breakage. However, even when these grafted membranes remain intact after the 45minutes, at best they can only capture aerosol as best as the commercial filter papers, and their aerosol lost to the waste container is similar.

The possible aerosol concentrations captured onto the membranes, factoring errors from the breathing apparatus, are shown in Figure (4.3-12). All 3 unmodified electrospun membranes, on average, can capture up to 50mg/mL of salt aerosol.[ϕ] The commercial filter paper, when it does not rupture, can capture up to 40mg/mL. The chiffon fabric, at best, can capture up to 30mg/mL. The total average amount of aerosol throughput possible using the 45minute discontinuous dispersal operating scheme for the SBA was: 64.1mg/mL. Therefore, the 3 unmodified electrospun membranes could capture ~78% of all aerosol droplets nebulized by the apparatus, and transmitted to the waste container.

[ϕ] The units of salt capture concentration: “mg/mL”, refer to the mass of salt in “mg” per “mL” of water in the aerosol.

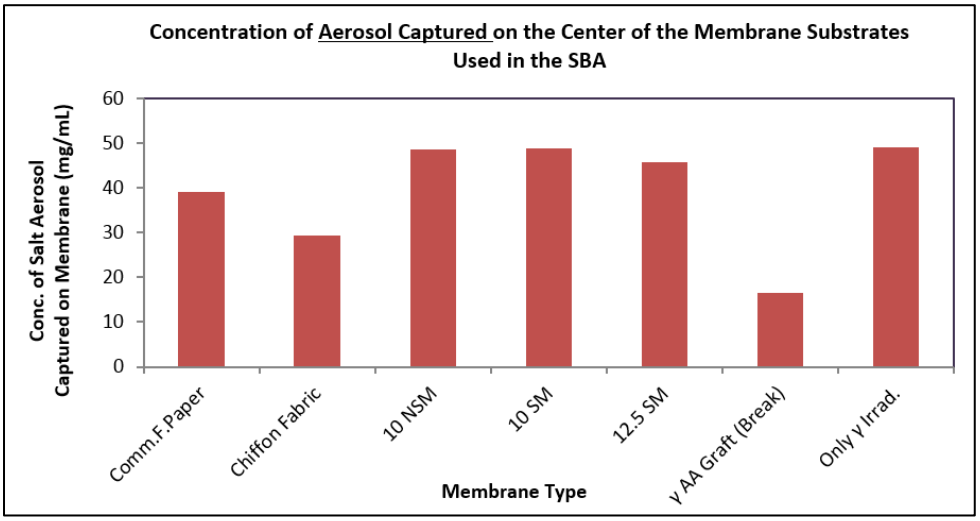

Figure 4.3-12 – Final estimated average concentrations of the salt aerosol captured on the various membranes for the 45 minute discontinuous aerosol capture mode. These values were calculated after factoring in possibility of aerosol loss in the SBA.

In most instances when the gamma-grafted acrylic acid sample was tested under this 45 minute discontinuous aerosol loading scheme, it broke. Because of the significant tearing and rupture, these grafted membranes captured less than ½ (namely, only 15mg/mL – 20mg/mL) of what the unmodified electrospun membranes could. The exposure to the acrylic acid, combined with the effects of the irradiation, caused a decrease in the overall robustness of the membrane leading to its premature rupture in the SBA. For reference, a sample of only gamma irradiated electrospun membrane was tested for aerosol capture as well. Because this sample performed very similarly to the unmodified membranes, this further indicates that the acrylic acid exposure had the effect of compromising the overall electrospun membrane breaking strength.

Figure 4.3-13 shows sample images of how each membrane performed after being subjected to 45minutes of discontinuous aerosol exposure in the SBA. Shown in the lower left corner (γ graft), the grafted electrospun samples rupture quite extensively in the center and on the sides where the membrane is tied. This accounts for the poor performance of the grafted membranes in comparison to the commercial filter paper shown in Figure 4.3-11. Overall, while the membranes for both 10CM SM and 10CM NSM seem to be indented in the

center, in response to the SBA pressure changes, they do not rupture during the aerosol loading. Furthermore, even though the commercial filter paper's tear in the center is less extensive as that of the grafted sample, it is enough to reduce its capture ability.

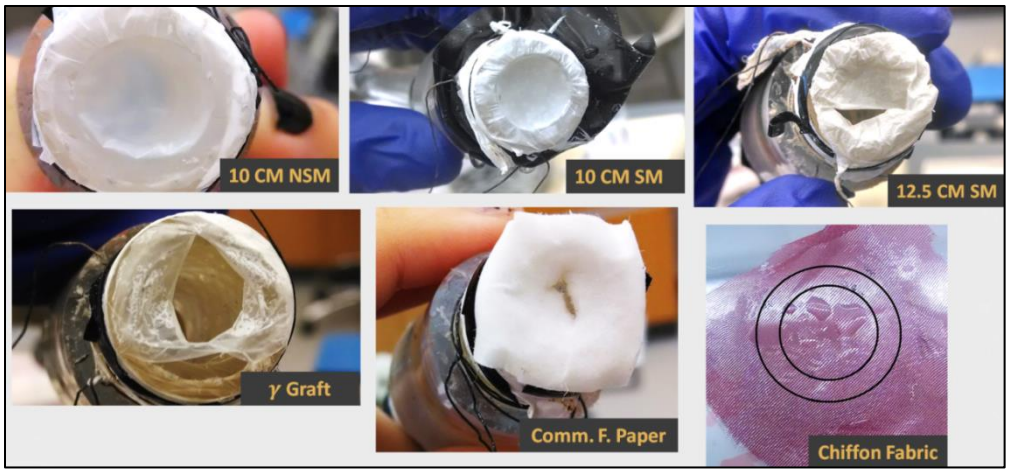

Figure 4.3-13 – Images of the wet membranes just after completing a 45 minute discontinuous aerosol capture trial. Membranes: γ Graft, 12.5CM SM, and Comm.F.Paper have all ruptured in the center of the aerosol capture region.

If the variability of the commercial filter paper performance is taken into account (i.e. it's susceptibility to rupture during aerosol loading), it captures 39% significantly less particle concentration than the electrospun membranes. An example of the z-test used (α=0.05) to compare the results of the membrane capture is shown in Figure 3 of the Appendix.

However, if the breaking variability of the commercial filter membrane is not considered, then there is no statistical difference between the aerosol capture capability for the commercial filter and the electrospun membranes according to the z-test used.

Although this implies that the electrospun nanofiber membranes do not always capture more aerosol than the commercial filter paper, unless the filter paper breaks, it does not mean that the electrospun membranes perform more poorly than the commercial papers. The nanofiber membranes can achieve the same performance with thinner membrane, and fewer tendencies to rupture. Nanofiber membranes are ~20μm thick, compared to the millimeter scale thickness of the commercial papers.

Overall, the maximum calculated concentrations which all membranes can capture, if the errors in the simulated breathing apparatus are neglected, are shown in Table 4.3.2, for the 45 minute discontinuous aerosol dispersion method.

#	Membrane Type	Average Conc. (mg/mL)
1	10CM NSM	63.53
2	10CM SM	63.34
3	12.5CM SM	57.83
4	Chiffon Fabric	44.36
5	Comm.F.Paper	29.36
6	AA Graft	31.95

Table 4.3.2 – The maximum throughput of aerosol which could be collected using the conductivity meter attachment to the SBA was 64.1mg/mL. The table above shows the average maximum amount of aerosol concentration which could get captured onto the membranes if errors such as apparatus aerosol loss aren't taken into account.[α]

4.3.5 – FESEM Images of Salt Aerosol Precipitated on Membranes Used in SBA Capture Studies

There are also significant differences in the way accumulated salt on the membranes precipitate from the aerosol after drying. Figure 4.3-14, -15, and -16 show types of sodium chloride deposition patterns on the electrospun membranes. These patterns are not observed on the control membranes (filter paper, or fabric) used in in this study regardless of exposure time to the aerosol. Such types of dendritic crystal growths, or fractals, would otherwise only occur on extremely smooth surfaces such as metals or glass. Harvard researchers have examined how both flat and curved surfaces contribute to crystal growth patterns.[143] They found that crystals can be subject to more elastic stress when the space they are confined in is more curved, or non-flat, and fractal formation is inhibited.

Ultimately, these crystal patterns and uniform cube formations on the electrospun membranes show that the membranes are highly smooth and symmetric enough for patterned crystallization to occur. Figure 4.3-17 shows an EDX map of how the aerosol

[α] See Figure 4.3-12 for concentrations after factoring in error.

precipitates on the commercial filter papers – it is not uniformly distributed, without crystalline order, and appears as a residue.

Since the surface area for the commercial membrane was found to be much smaller than that of the electrospun membranes, (commercial: ~2m^2/g, electrospun: ~44-58m^2/g) the amount of particle accumulation possible area of the filter paper is smaller. The commercial filter membranes do not have a uniform distribution of fibers in their compact structure, and so, pore sizes are largely variable. Per area there are overall less pores because the actual pore sizes can span diameters of up to 50μm (Figure 4.3-17). Therefore, based on the surface area of the membrane structure alone, we would expect smaller amounts of capture, and higher amounts of aerosol loss to occur for the commercial membrane.

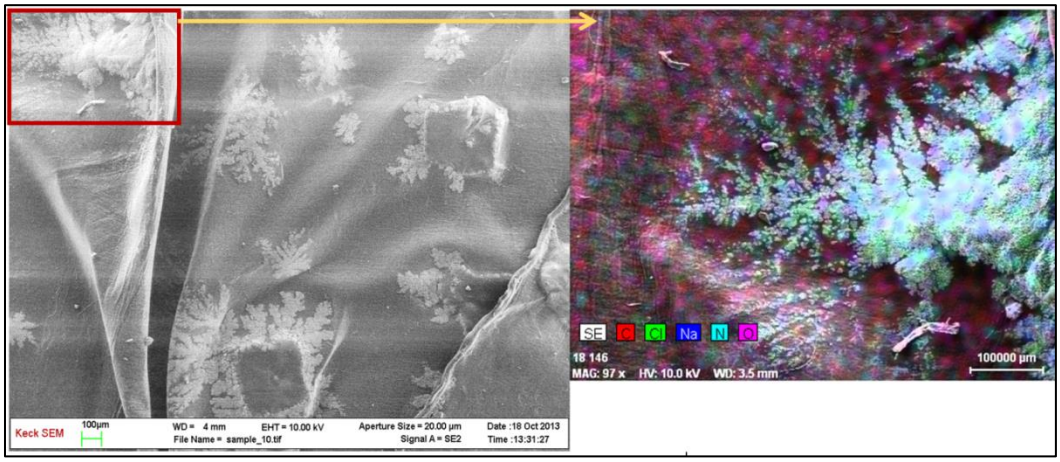

Figure 4.3-14 – Fractal formation of captured salt aerosol on electrospun membrane. Right Image shows EDX Element map (showing NaCl presence) for Mandelbrot-like pattern indicated in Red.

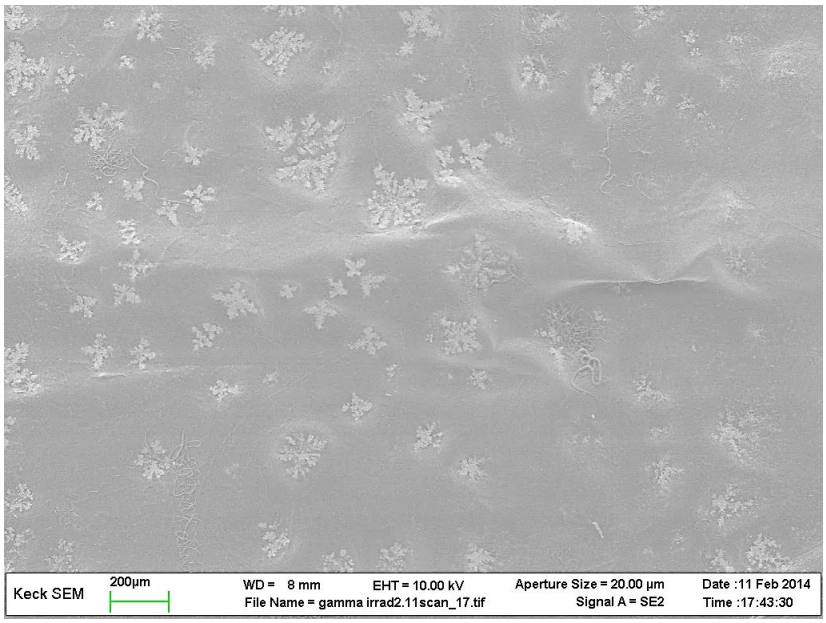

Figure 4.3-15 – Wide range of distribution of fractal precipitates formed on electrospun membrane. Uniform distribution of pattern is also seen.

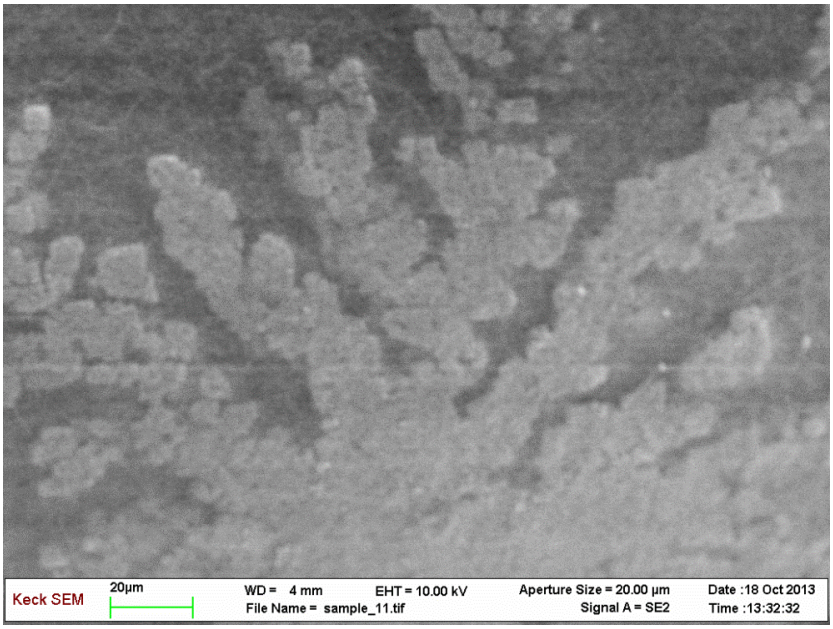

Figure 4.3-16 – Close-up texture of salt aerosol precipitate dendrite edges. This image shows that most aerosol salt precipitated at the membrane surface, and the fractal precipitate "sits" over the nanofiber mesh, instead of penetrating through it.

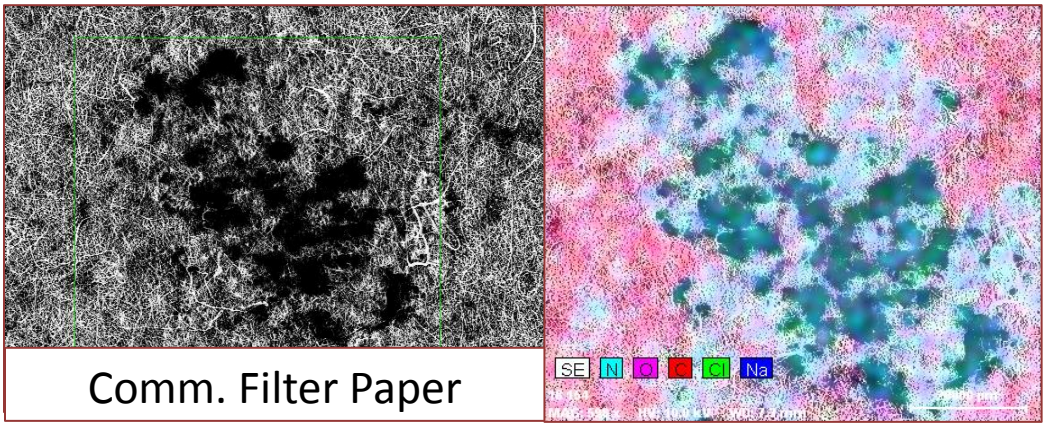

Figure 4.3-17 – FESEM image (left) and EDX Element Map (Right) of a commercial filter paper with salt particle residue precipitated from aerosol capture. Residue at ~200µm is largely undetectable in FESEM image. In the EDX Map, the Cl and Na presence is scattered in a general circular pattern with no precisely shaped boundaries.

Furthermore, Figure 4.3-18 shows that crystal precipitation on the nanofiber membranes is highly defined in structure for these fractal areas, whereas for the commercial filter papers it is not. Most precipitate crystals on the membranes ranged from 150nm – 500nm in size.

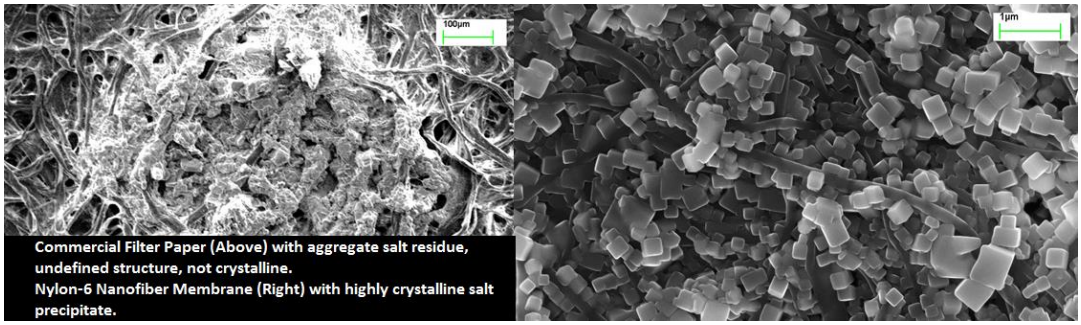

Figure 4.3-18 – Close-up differences in the precipitated salt crystallinity found in the fractals and clusters of salt particles collected on the commercial filter paper (right) and nanofiber membranes (left) after aerosol dispersal.

4.3.6 – Salt Aerosol Particle Concentration and Particle Sizes Captured by the Cascade Impactor (SBA Dispersal Mode 3) and Differences in Observed Membrane Weight

Particles which can be easily inhaled typically range from nanometers up to 6µm in dimension.[24-27] After using the cascade impactor as a waste collection vessel to collect the particle droplets not captured by the filter membrane placed in between in the SBA, the

maximum percent of fine size to coarse sized particles which could be collected on the membrane were found in Figure 4.3-19.

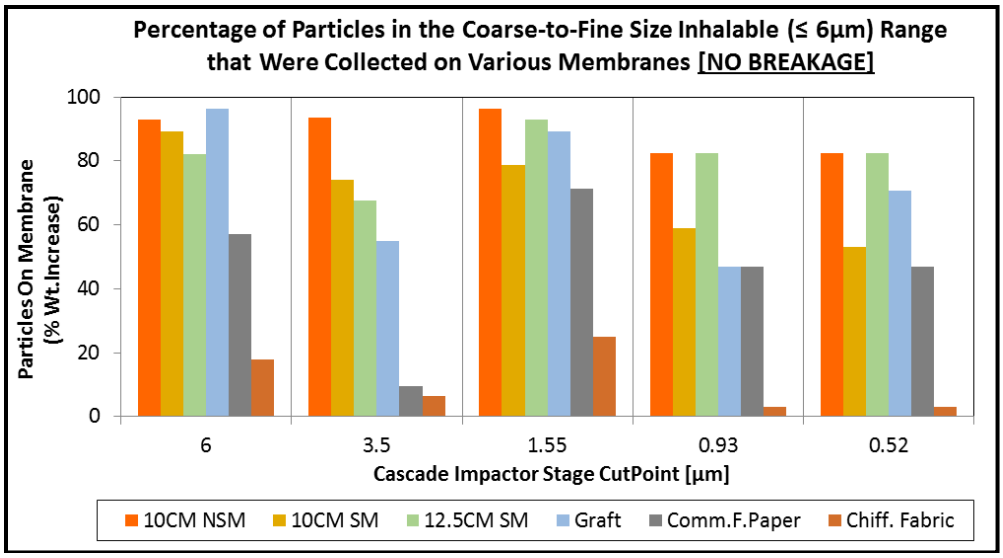

Figure 4.3-19 – Estimated % weight increase of salt aerosol particles present on the membranes between 0.52µm – 6.00µm in size, from the 25 minute continuous aerosol dispersal using a cascade impactor as the final waste capture. [ε]

Overall, the electrospun membrane: 10CM NSM and 12.5CM SM perform the best for capturing this range size of aerosol droplets. Since this aerosol dispersal scheme was not paused at set time intervals, there were less abrupt pressure changes throughout the system which could have affected the membrane integrity. Here, we see that capture for the thinnest membrane (12.5CM SM) and structurally modified membrane (Graft) can be high if it remains intact. This can be due to the reduced pore sizes and meshed fibers which occurred as a result of the gamma irradiation grafting process with acrylic acid shown in Chapter 4.2, for the grafted membrane. Although the surface area is higher for the grafted membrane compared to the commercial filter paper, the difference is not very drastic (graft: 9.15m^2/g, Comm.F.Paper: 2.19m^2/g). Therefore, the differences between the particle

[ε] The original measurements of particle concentrations captured per substrate stage in (mg/mL) are shown in Figure 4.3-20 below for the range: 0.52µm – 6.00µm. Figure 4.3-23 in the Appendix shows the calculated concentration of particles per membrane from using the data in Figure 4.3-20.

capture ability for these two membranes, especially for the <1µm particle size range, are not significant.

Membranes 10CM NSM and 10CM SM cannot perform better for capturing particles in the 1μm – 0.52μm range, but still can perform up to 40% better than the commercial filter paper for particles between 3.5μm - 6μm in size.

High losses of particle concentrations onto the separate cascade impactor size cutpoint stages occurred for the commercial filter paper at 21.3μm, and at 6μm, shown in Figure 4.3-20. As expected, the chiffon fabric tends to lose most particles which begin to decrease in size starting at 6μm through to 0.52μm. This can be explained by the large pore sizes that the fabric has in comparison to the electrospun materials and commercial filter paper.

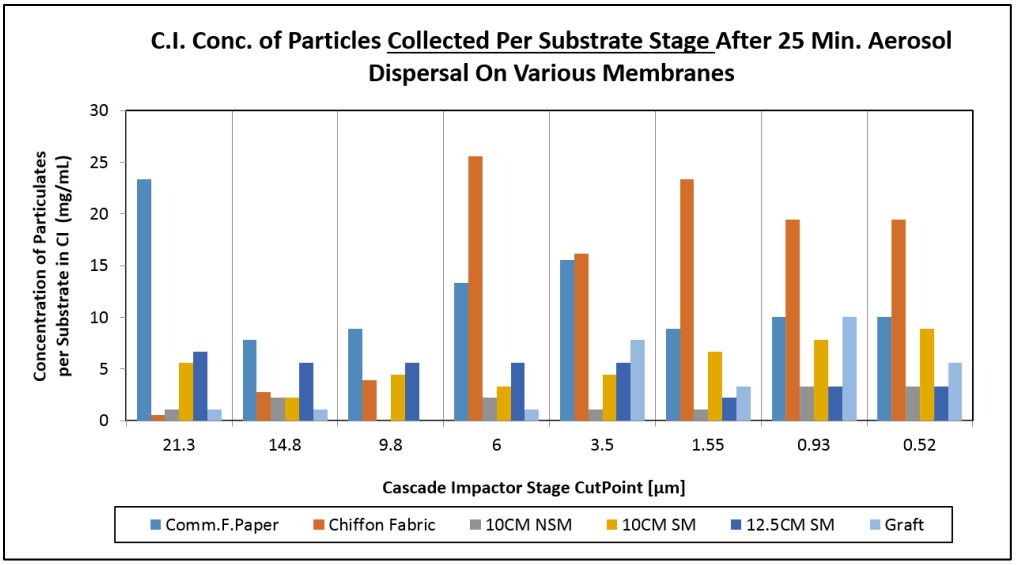

Figure 4.3-20 – Concentration of particles collected on substrates from the cascade impactor after 25 minutes aerosol capture using various filter membranes.

Once the membranes were dried, the precipitated particle weight percent increase, and the absolute weight increase for the membranes were compiled below in Figures 4.3-21 and Figure 4.3-22. Up to 100% of the original weight can be collected onto the electrospun membranes, as opposed to only 20% for the chiffon fabric and the commercial filter papers,

Figure 4.3-21. This shows that the nanofibers can be absorbent materials, and from their resistance to rupture when wet (especially membranes: 10CM NSM, and 10CM SM) can remain largely unchanged in fiber morphology from the process.

Although the absolute weight increase for the electrospun membranes does not surpass that of the commercial filter paper and chiffon fabric, Figure 4.3-22, these irregularities in mass balance are due to the natural differences in the way which salt crystals precipitate on the membranes.

In observing the total absolute weight increase, we rely on the assumption that all of the wet aerosol collected on the membranes will precipitate out 100% of the salt which was collected in the droplet form. We also assume that none of the wet aerosol is lost from the moment the membranes are removed from the SBA to the moment when they begin to dry on the petri dishes for storage. Since there is already an observed difference in the precipitation pattern, from the FESEM images shown in Section 4.3.4, we can estimate that there is a significant amount of precipitated salt loss as the electrospun membranes are drying due to sublimation. Since the particles appear to form on the surface of the nanofiber membranes, particle loss due to handling after drying is also highly possible.

Furthermore, since the patterned salt precipitates on the electrospun membranes were shown to be just on the overall fiber top surfaces, rather than integrated within the fibrils (as the precipitate in the commercial filter papers was), it shows that sublimation of the salt crystals would have been much more likely to occur. The self-assembly of crystals and other colloids into organized fractals is highly dependent on the surface they are exposed to, but also on the atmospheric conditions of the crystals in solution.[136-138] For instance, before dendritic formation of snowflakes, or frost patterns on windows can occur, the surface of the material must be supersaturated with the solution (in this case, the collected wet aerosol of water and salt). The rate of solution evaporation and precipitation is

in constant flux throughout the material, and this process leads to the formation of patterned crystals as seen in the Figures above.

Thus, though it would not appear as though the absolute collected salt weight for the nanofiber membranes is significantly higher and different from that collected on the commercial filters, it's more likely that more aerosol droplets adhered to the membrane surface from the formation of the patterns observed.

Future studies for aerosol capture onto nanofiber membranes would benefit from using another type of aerosol suspension for dispersal which can both mimic the nano- "viral particle" sizes difficult to capture, and not be as sensitive to humidity and atmospheric conditions, like the salt aerosol was. Monitoring the actual amount of particles captured using gravimetric weight change methods could then be more easily performed, and subject to less error.

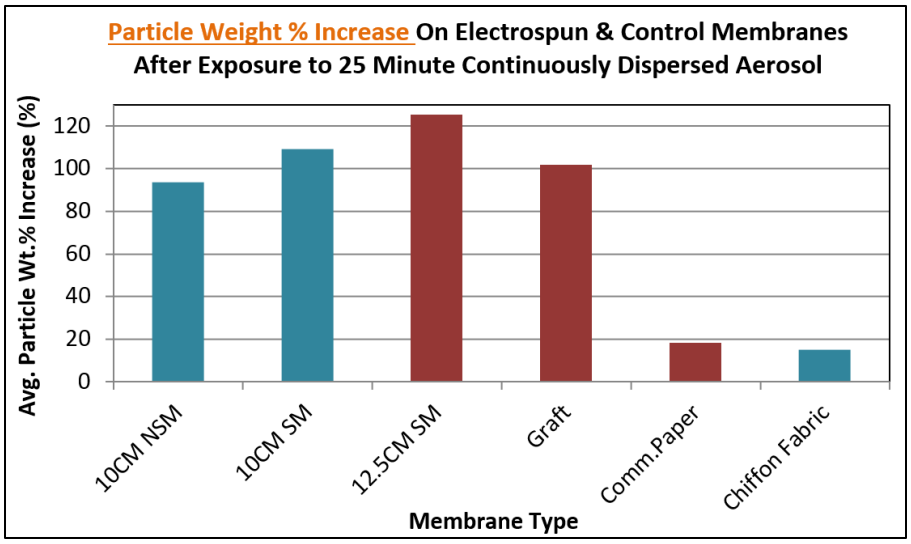

Figure 4.3-21 – Particle weight % increases observed on the electrospun and control membranes after 25 minutes aerosol capture using the cascade impactor. Red bars indicate breakage of the membrane during aerosol capture.

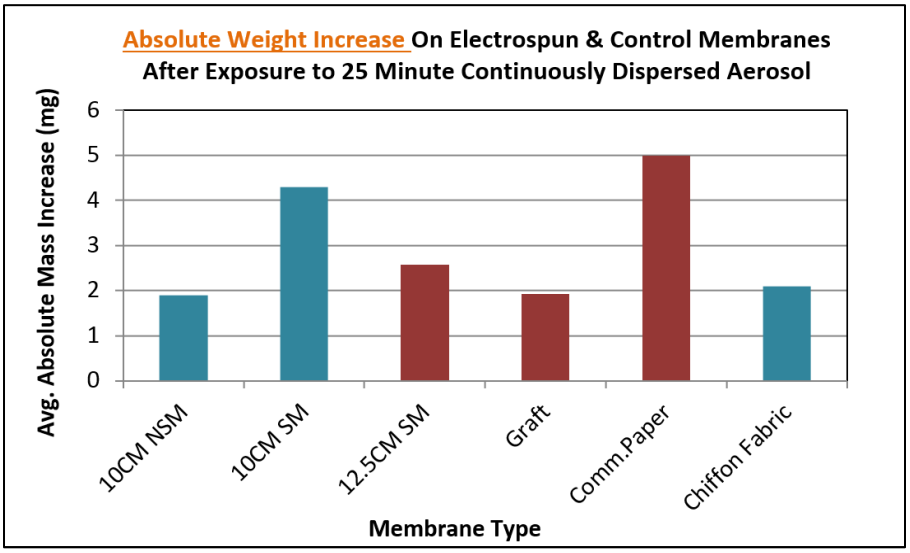

Figure 4.3-22 – Absolute particle weight increases observed on the electrospun and control membranes after 25 minutes aerosol capture using the cascade impactor. Red bars indicate breakage of the membrane during aerosol capture.

5 – CONCLUSIONS

The ultimate goal of this research was to evaluate the extent to which electrospun Nylon-6 nanofiber membranes could be used as wearable textiles for capturing exhaled viral particle aerosols from human breath. Since researchers have theoretically modeled how small diameter nanofibers can capture large sub-micron to micron sized particles in air, three large scale (1/2ft. x 1yd.) electrospun nanofiber sheets were created with targeted small diameters and uniform fiber coverage.

The three sheets were electrospun membranes: #1). 10cm distance without slide mechanism to rotating drum collector (10CM NSM), #2). 10cm distance with slide mechanism (10CM SM), and #3). 12.5cm distance with slide mechanism (12.5CM SM). From these sheets, smaller membranes were extracted, and put in a Simulated Breathing Apparatus (SBA). The SBA simulated the "human exhaled breath" necessary for transmitting aerosols of nanoparticle droplets toward the nanofiber membranes for capture.

Here, the transmitted nano-viral particles were simulated by an aerosol of sodium chloride salt in water. To show a broad range of capture results, two control membranes in the apparatus were compared against the electrospun membranes: commercial cellulose filter paper, and chiffon polyester fabric. Three types of operating mechanisms for the SBA system were employed – 1. discontinuous aerosol dispersal for 45 minutes, 2. continuous aerosol dispersal for varying times, and 3. continuous aerosol dispersal for 25 minutes with cascade impactor capture.

Additionally, two methods of electrospun membrane surface functionalization were explored to examine if surface treatments to the membranes would alter aerosol capture. These were: EDC [1-Ethyl-3-(3-dimethylaminopropyl)carbodiimide] mediated grafting, and mutual gamma irradiation mediated grafting. Poly(acrylic) and acrylic acid were used for attachment to the Nylon-6 nanofiber membranes, respectively for each method.

Some key facts and ideas which emerged from the entire study – from using large scale electrospinning to capturing sub-micron particle aerosols, and altering the electrospun membrane surface, are discussed below.

5.1 - Generation of Large Scale Electrospun Membranes

Electrospinning onto a rotating drum collector with 12 needle setup, and axial slide produces large scale (1/2 ft. x 1 yd.), uniformly covered sheets of Nylon-6 membrane material up to 40MPa in elastic modulus. Fiber diameters for all membranes range from 98nm – 140nm, and contain similar mean area pore sizes (104nm - 122nm). These membranes can be made with as little as 7mL of Nylon-6 20wt% polymer solution in formic acid, and one membrane takes between 2-4 hours to complete. The membranes can be easily peeled from their collectors, and various collectors types (aluminum to open-network woven fabrics) can be used to collect nanofiber membranes on. PAN (poly(acrylonitrile)) and PVA (poly(vinyl alchohol)) solutions of similar concentrations can also be electrospun on the drum. This improved electrospinning apparatus shows that large scale, intact, uniform electrospun membranes which can be textile grade for handling can be produced.

5.2 - Surface Modification of Electrospun Membranes

The Nylon-6 electrospun membranes were successfully surface modified using 523 rads/min gamma irradiation dosage. After as little as 1 minute of exposure, acrylic acid monomer polymerization occurred, and the polymer attached to the membrane via radical polymerization. This produced membranes with smaller surface area, polymerized acrylic acid beads on the surface, and reduced pore sizes. Based on the FTIR spectra, there is 17% - 20% chance of surface grafting occurring using irradiation and acrylic acid alone. Increasing irradiation exposure time (5 minutes - 20 minutes) increases acrylic acid incorporation into

individual fibrils. The Nylon structure is modified to have a more stable crystalline phase (a higher heat of enthalpy for melting is seen).

These results are significant in that gamma irradiation low dosages (523 rads, or 5.23 grays) with other molecular species present with nanofiber membranes can be used to quickly modify the membranes structure both chemically and physically. Quick surface grafting of nanofiber membranes may be possible without compromising the structure and handling of the nonwoven nanofiber mat. This modified textile can be then incorporated into another textile garment for added functional capabilities.

5.3 - Membrane Aerosol Capture SBA

The commercial filter paper (Whatman Brand), electrospun membrane 12.5CM SM, and gamma irradiation grafted membrane perform variably in the SBA for the 45 minute aerosol capture trials. Decreased mechanical strength during the pressure changes from aerosol wetting leads to breaks and tears in the membranes about 50% of time they were used for capture.

Electrospun samples: 10CM NSM, and 10CM SM, do not suffer from mechanical strength loss and remain intact after aerosol loading.

Discontinuous Aerosol Dispersal

Compared to the commercial filter paper capture trials for the 45 minute discontinuous dispersal of aerosol, the electrospun membranes captured statistically equivalent amounts of aerosol (between 40mg/mL to 50mg/mL). If the variability of the commercial filter paper performance is considered, then the electrospun membranes are able to capture 39% statistically higher amount of salt aerosol concentration.

This is significant because although the 10CM NSM, and 10CM SM electrospun membranes may not outperform the commercial filter papers in capture, they are much more flexible to the pressure changes and do not break during wetting. They are on average

20μm thick, while the filter paper is on the millimeter thickness scale. It is possible that one membrane can perform as well as one commercial Whatman sample, and with further layering using electrospun membranes, the capture may be improved.

On average, significant capture amounts can be up to: 29.4mg/mL, 48.5mg/mL, and 48.7mg/mL, for the commercial filter paper, 10CM NSM and 10CM SM, respectively. The total amount of aerosol throughput for this dispersal method is 64.1mg/mL.

Continuous Aerosol Dispersal with Cascade Impactor

From the cascade impactor results: the highest percent of particles between 0.52um - 6um in size are captured most consistently by the electrospun 10CM NSM membranes. The commercial and chiffon fabric control samples capture most droplets in the large size ranges.

The grafted and 12.5cm spun membranes are still susceptible to break, but because of less pressure changes using this aerosol dispersal method (25 minutes continuous), these membranes are able to capture the smaller size particles. This shows that the two membranes with smallest pores used in this study, can capture the smallest rage of particle sizes.

Membrane Weight Change & Salt Precipitation Patterns after Aerosol Capture

Particle weight percent increase was highest for all three electrospun unmodified membranes. The weight can increase up to 100% even though the membranes are thinner than the fabric and commercial filter paper. Weight percent change for the commercial papers and fabric go up to 20%, at most. However, absolute weight changes for the membranes are not greater than those for the commercial filter paper and chiffon fabric. At best, the actual accumulated precipitated weight of salt particles on the membranes can be between 2mg - 4.5mg; a similar amount measured for the filter paper and fabric.

While much larger particle weights for the electrospun materials were expected, the mass balance disparity is due to differences in the salt particle precipitation on each given membrane. Electrospun membranes precipitate salt particles in uniformly packed,

fractal crystal patterns, whereas on the filter paper, and fabric, the salt precipitates as a residue. On the filter papers, there is no symmetric, uniform crystal growth and salt residue embeds within the paper fibers. For the electrospun membranes, salt residue crystalizes on the fiber surface, in the fractal patterns. Since the salt captured precipitates uniformly only on the top, it's possible that much of the collected salt may have sublimed off the surface, contributing to less absolute weight change.

The emergence of these salt fractal patterns on the electrospun membranes further show that electrospun materials may be used to crystallize, or help precipitate other types of inorganic salts/minerals which could serve other purposes. Studies for using electrospun materials as substrates for inducing reactions are still currently being explored.

~*~*~

These simulated breath aerosol capture and surface modification experiments for the electrospun Nylon-6 membranes show that while these materials may be extremely thin, and lightweight, compared to normal filter papers, they can be created in yard size dimensions, with specific properties (fiber diameters, pore size range), and maintain durable when wet. The membranes can be surface modified using irradiation techniques, and be combined with other polymers post electrospinning. These attributes make Nylon nanofiber membranes potentially useful in wearable textiles aimed towards capturing aerosols of nano- and submicron sized particles.

6 – FUTURE WORK

In order to incorporate these nanofiber membranes into wearable textiles, such as surgical masks, and other garments/devices which can detect and prevent the transmission of exhaled aerosol viral particles, the electrospun membranes should undergo further aerosol capture trials beyond those presented in this study.

6.1 – Quantum Dot & Influenza Vaccine Solutions for Aerosol Capture

While a nebulized salt solution transmitted in the simulated breathing apparatus can mimic the characteristic of a wet aerosol, and the concentrations which could probably be exhaled from a contagious individual, particles in a salt solution cannot entirely mimic the behavior of viral particles in air. Individual Influenza viral particles that do not cluster can be only as large as 6nm - 10nm, and those which do cluster, can aggregate up to 600nm in size.

In order to model this broader range of particle sizes, nebulized solutions of quantum dots can be used in future aerosol capture experiments. Here, a study examining how well the nanofiber membranes capture particles of a smaller, unchanged size range can be performed without the consideration of how the particles precipitate on the membranes. Unlike the salt ionic particles in solution, which are not of a defined size, and can precipitate into random size clusters depending on the surface they were captured on, and atmospheric conditions, the quantum dots nebulized will always have a constant diameter, and are not humidity dependent.

Quantum dots can be synthesized to have a wide range of particle sizes from 2nm to 50nm, and it would be interesting to see how the capture results for a continuous nebulization using the cascade impactor, change with increasing particle diameter per solution. The results could potentially show a more precise threshold point of when the most particles, of a certain size, would be captured onto the nanofibers. Since quantum dots in aqueous solutions vary in emitted fluorescence wavelengths based on their size, Figure 6.1-1,

their concentration collected on the membranes can be a function of their observed emitted wavelengths using a fluorescence microscope.[139, 140]

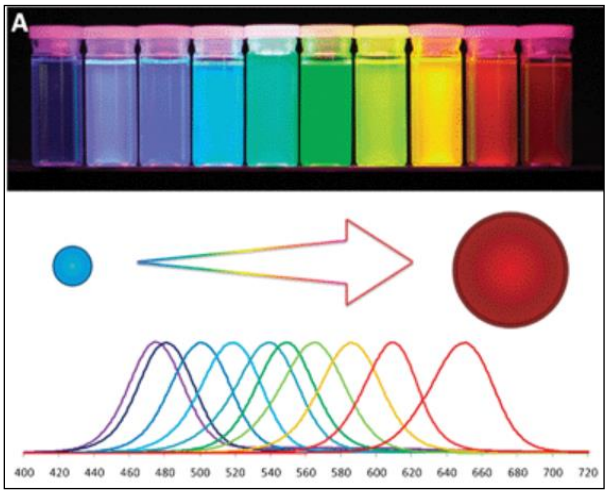

Figure 6.1-1 – Quantum Dot size ranges from: 2nm – 10nm. With increasing size range, emission wavelengths detected using fluorescent confocal microscopy, change from 400nm to 700nm (violet to red).[141]

With further reinforcements to the simulated breathing apparatus, such as quick locking tube clamps to prevent air leakage, and improvements to the filter membrane holders, it could be possible to nebulize an aqueous solution of Influenza flu vaccine for capture onto the membranes.

6.2 – Modification of Nanofiber Membranes & Integration with Sensor Assay Devices

It is known that the large scale Nylon-6 nanofiber membranes electrospun using the rotating drum collector from this study are:

- Highly Flexible (able to fold and easily conform to the tube holders in the aerosol apparatus),
- Very Lightweight (~25x lighter than commercial filter paper),
- Smooth & with Soft Hand (nanofiber diameters, low crystallinity)
- Strong and Durable (unbreakable after long periods of wet salt aerosol loading and

capture)

Additionally, the surfaces of these membranes could be modified by using gamma irradiation to:

- Decrease overall pore size,
- Add texture to the individual fibrils in the membrane,
- Attach other monomers/polymers to the surface

Considering these unique attributes, the creation of stackable Nylon-6 nanofiber membranes with integrated functionalities can be possible [Figure 6.2-1]. This could potentially lead to the creation of a single stacked thin membrane which can be used as a potential surgical mask integrated with sensors. These sensors may be 3-D printed onto thin and flexible polymer films, such as was done recently monitoring heart activity and stimulations, and be used to detect when aerosol concentrations (of a specified type, either viral or chemical) collected on the membrane reach a critical level.[142]

Additionally, there is the possibility of coupling the nanofiber membranes with a microfluidic assay "lab-on-a-chip" device, seen in Figure 6.2-2. This "lab-on-a-chip" device can be used by individuals to monitor the presence of Influenza exhaled. The nanofiber membrane containing a sample of the captured exhaled aerosol can be used on a lateral flow assay sensor strip (LFA). The LFA can be customized to distinguish viral presence based on the antibody types detected from the exhaled breath sample. Positive indication of Influenza virus present will result in both the "Test Line" and "Control Line" markers appearing on the strip.

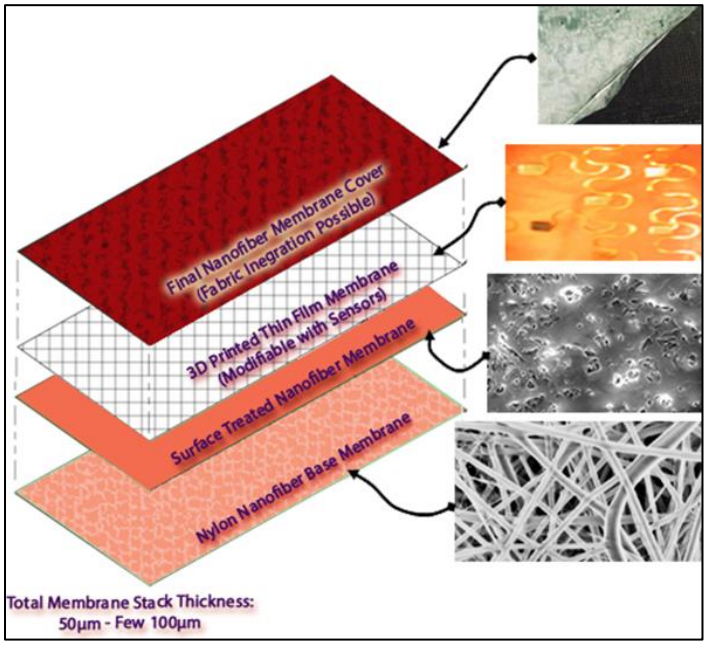

Figure 6.2-1 – Layered nanofiber membrane stack with each membrane layer containing different functionalities, and tailored properties. Layers can include membranes which have surface modified textures (reduced pore sizes, grafted areas), as well as thin polymer films which may contain sensor units for detection. The natural static charge the thin nanofiber membranes have after being electrospun can be exploited to bind the layers together in order to make a stacked membrane. Ultrasonic sonobonding of layers can also be employed.

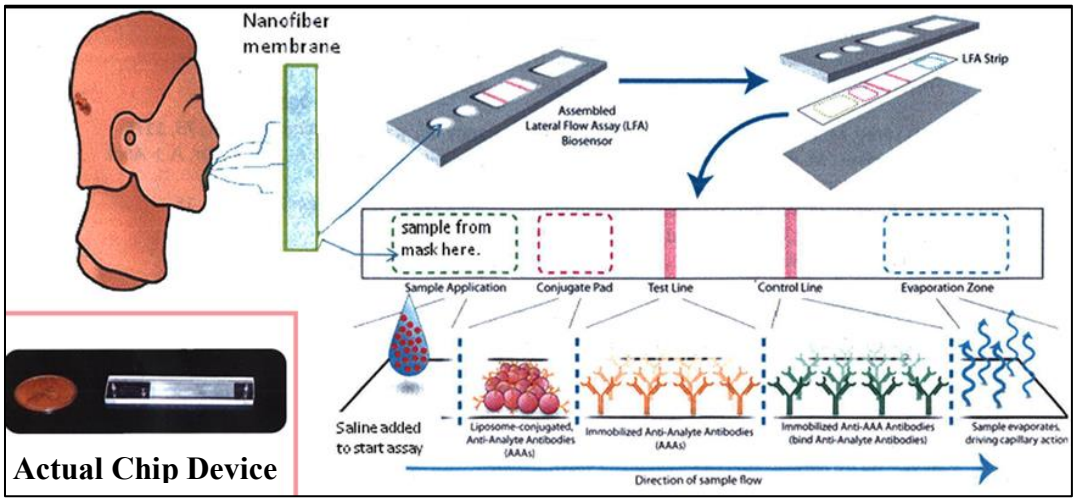

Figure 6.2-2 – Example of how a nanofiber membrane sample with collected exhaled aerosol can be coupled with an assembled Lateral Flow Assay (LFA) sensor chip (size compared to a penny, lower left) to show the presence of captured viral aerosol particles. A saline solution is added to the membrane sample, which starts the assay of viral particles with antibodies. As the combined antibody/exhaled breath mixture travels by capillary action throughout the strip, the appearance of the "Test" and/or "Control" Lines will indicate whether viral residue is present.

7 – APPENDIX

Wt. of Membranes	[#1] - 10CM NSM (g)	[#2] - 10CM SM (g)	[#3] - 12.5CM SM (g)
1	0.0027	0.0017	0.0007
2	0.0020	0.0021	0.0009
3	0.0018	0.0019	0.0008
4	0.0020	0.0022	0.0006
5	0.0024	0.0021	0.0008
Avg Weight (g)	**0.0022**	**0.0020**	**0.0008**
Thickness of Mats: ~ 12µm, ~12µm, ~9µm || Dimensions : 2cm x 4 cm			
Density of Membranes	**[#1] - 10CM NSM (g/cm^3)**	**[#2] - 10CM SM (g/cm^3)**	**[#3] - 12.5CM SM (g/cm^3)**
1	0.28	0.18	0.10
2	0.21	0.22	0.13
3	0.19	0.20	0.11
4	0.21	0.23	0.08
5	0.25	0.22	0.11
Avg Mat Density (g/cm^3)	**0.23**	**0.21**	**0.11**

Table 1 – Raw data showing the measured weights of the 3 types of electrospun membranes, the thickness of the membranes (acquired from SEM images), and the calculated density of the membranes. Averages for each are shown in green rows.

Young's Modulus Test	Membrane Type	Avg - Hor (MPa)	Avg - Vert (MPa)	Z-Value (2-Tail)	Conclusion	Avg of 2 Axes (MPa)
1	10CM, NSM	77.86 ± 16.08	65.30 ± 13.84	-1.66	Fail to Rej. H0	71.58
2	10CM, SM	35.06 ± 11.60	24.54 ± 5.88	-1.93	Fail to Rej. H0	29.80
3	12.5CM, SM	28.46 ± 11.55	17.68 ± 7.68	-1.85	Fail to Rej. H0	23.07
H0: YM (or BM) Mean of the vertical = YM (or BM) Mean of the Horizontal						
Hα: YM (or BM) Mean of the vertical ≠ YM (or BM) Mean of the Horizontal						
Z-Value Limit: [-1.96 1.96], 95% Confidence						

Table 2 - Young's Modulus averages of the horizontal and vertical axes from the 3 standard membranes. Hypothesis test results are shown to see if the arithmetic means (averages) of both axis moduli are statistically similar enough for combination.

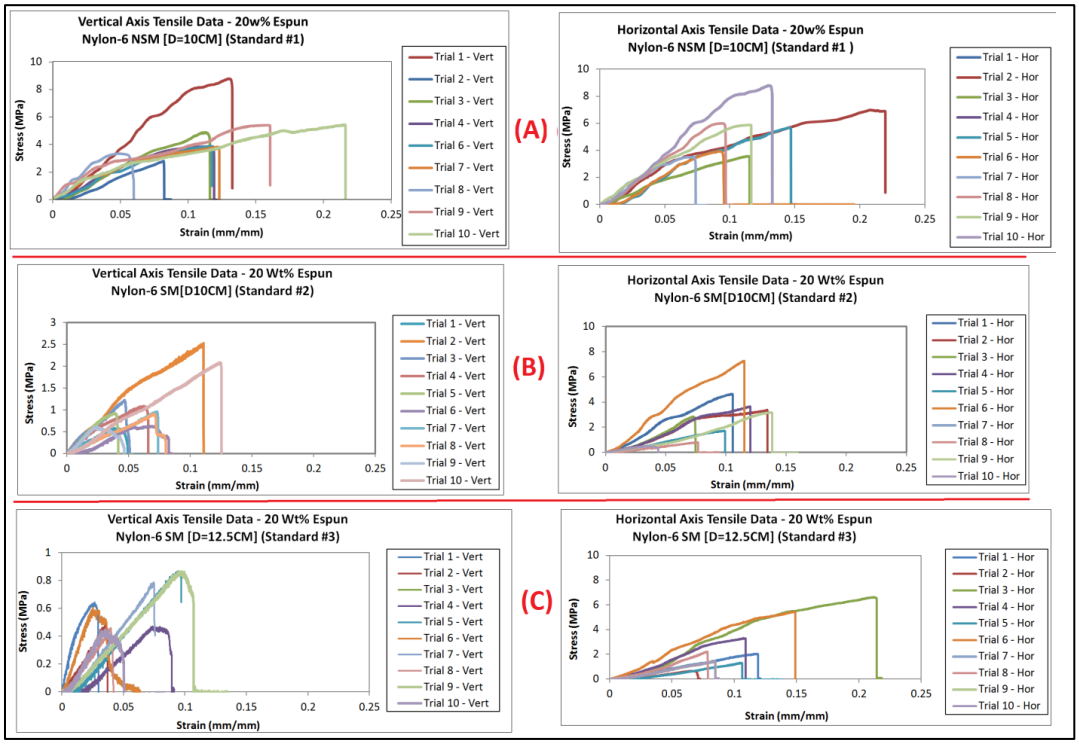

Figure 1 - Raw stress vs. strain curves for horizontal and vertical axis Instron tensile tests performed on samples from Membranes #1 - #3 [shown as A – C, above].

	Comm.F.Paper	*10CM NSM*
Mean	29.360	63.526
Known Variance	459.954	0.694
Observations	3.000	3.000
Hypothesized Mean Difference	0.000	
z	**-2.757**	
P(Z<=z) one-tail	0.003	
z Critical one-tail	1.645	
P(Z<=z) two-tail	**0.006**	**0.994**
z Critical two-tail	**1.960**	
Amount of difference from Limits (i.e. how much Statistical Diff.):	**39.487**	

Figure 3 – Raw data for comparing the statistical significance of the difference between particle capture during the aerosol capture studies. Here, the commercial filter paper mean capture amount is compared against the electrospun membrane 10CM NSM capture amount. The important factors are the Z value, the P(Z) value, the bounds for the Z Critical two-tail test and, how different the Z value is from the Z Critical bounds.

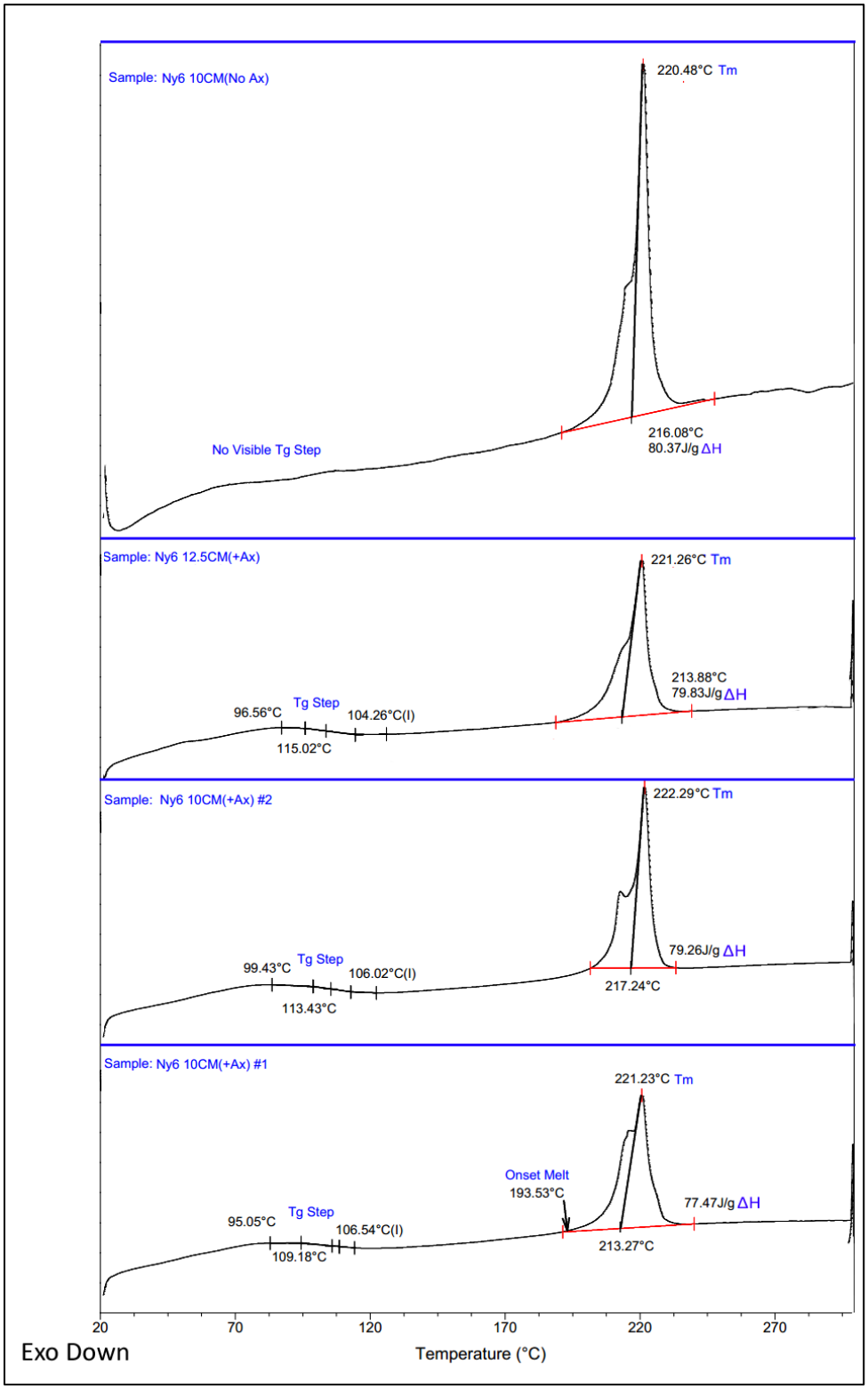

Figure 2 - Raw DSC data for all 3 electrospun Nylon-6 membranes with 1 extra replicate of the membrane spun at 10CM with the axial slide present (SM). ΔHm values, Melting onset, and Tm points, and Tg steps are labeled for each.

Sampling Flow Rate Q (LPM) 2.0
Starting Time T_1 (Hrs.) 0800
Ending Time T_2 (Hrs.) 1600
Sampling Time T_2-T_1 (Hrs.) 8
Sampling Volume V (m^3)(1) 0.958
Total Mass Concentration C_{tot} (2) (mg/m^3) 8.35

Impactor Model No. 298
Impactor Serial No. 525

Stage Number	Stage Cut-Point D_p (3) (Microns)	Initial Weight W_1 (mg)	Final Weight W_2 (mg)	Particulate Weight W (4) (mg)	Concentration ΔC (5) (mg/m^3)	$\log_{10}D_p$	$\Delta\log_{10}D_p$ (6)	$\Delta C/\Delta\log_{10}D_p$ (mg/m^3/log micron)	GMD (8) (microns)	% W_{tot} (%)	% < D_p
1	21	50	51.00	1.00	1.04	1.322	0.377 (8)	2.8	32	12.5	87.5
2	15	50	50.60	0.60	0.63	1.176	0.146	4.3	18	7.5	80.0
3	10	50	50.80	0.80	0.84	1.000	0.176	4.8	12	10.0	70.0
4	6	50	51.30	1.30	1.36	0.778	0.222	6.1	7.7	16.2	53.8
5 or 5A	3.5	50	51.20	1.20	1.25	0.544	0.234	5.3	4.6	15.0	38.8
6	2	50	51.00	1.00	1.04	0.301	0.243	4.3	2.6	12.5	26.3
7	0.9	50	51.00	1.00	1.04	-0.046	0.347	3.0	1.3	12.5	13.8
8	0.5	50	50.60	0.60	0.63	-0.301	0.255	2.5	0.7	7.5	6.3
Back-Up Filter	0.25 (8)	60	60.50	0.50	0.52	-0.602	0.301	1.7	0.4	6.3	0
W_{tot} (7)	--	--	--	8.00	8.35	--	--	--	--	100	--

NOTES: (1) $V = \frac{1}{16.7} Q(T_2-T_1)$ (2) $C_{tot} = W_{tot}/V$ (3) From Section 8.1
(4) $W = W_2 - W_1$ (5) $\Delta C = W/V$ (6) $\Delta_i \log_{10}D_p = \log_{10}D_{p_{i-1}} - \log_{10}D_{p_i}$
(7) W_{tot} = sum of particle masses for all stages including back-up filter.
(8) $GMD_i = \sqrt{D_{p_i} \times D_{p_{i-1}}}$. D_{po} is the largest particle size sampled. If not known, you can use D_{po}=50 microns. By convention, the minimum diameter for the filter stage is assigned a value one half that of the last impactor stage.

Figure 4.3-3 – Example data worksheet for relating particle size captured to weight change per stage. Important columns for data analysis include: Particulate Weight Change, Concentration, GMD (Geometric Mean Distribution), and W/W_{Total} (%).

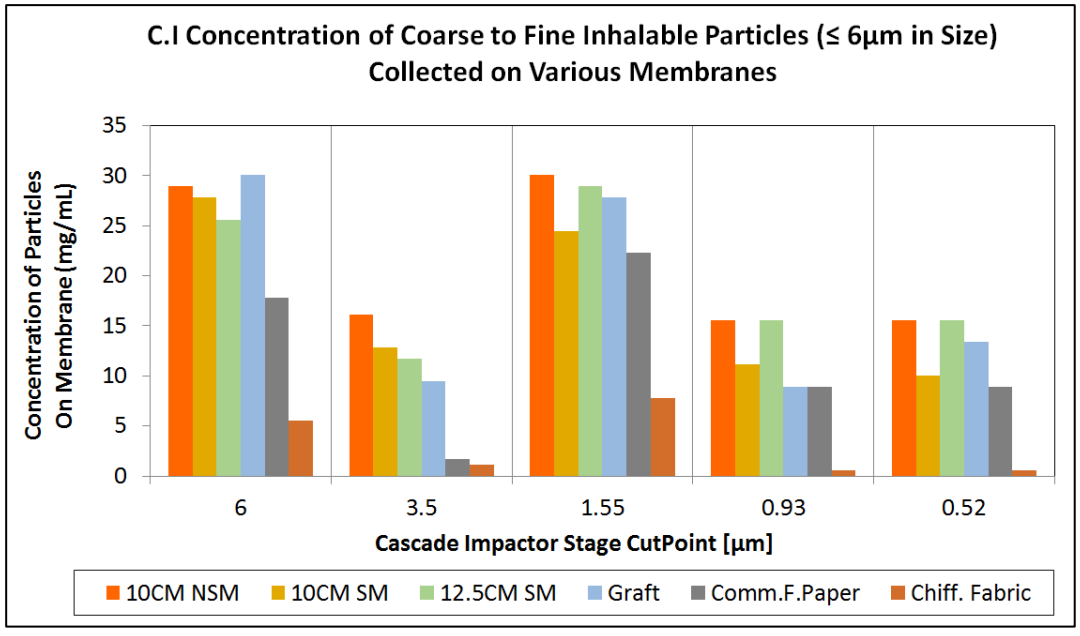

Figure 4.3-23 – Concentration of salt aerosol particles captured on the membranes found from taking the difference between total aerosol throughput possible for the stages: 0.52µm – 6.00µm, and the particle concentration experimentally gathered in Figure 4.3-20.

8 - LIST OF REFERENCES

1. Xiao, C. *et al*. Cryo-electron microscopy of the giant Mimivirus. *Journal of Molecular Biology* **353**, 493–496 (2005).

2. Giocondi, M.-C. *et al.* Organization of influenza A virus envelope at neutral and low pH. *The Journal of General Virology* **91**, 329–38 (2010).

3. Tatem, a J. *et al.* Air travel and vector-borne disease movement. *Parasitology* **139**, 1816–30 (2012).

4. Kozlowski, D. Physical interventions to interrupt or reduce the spread of respiratory viruses. *International Journal of Evidence-Based Healthcare* **10**, 159–161 (2012).

5. Brankston, G., Gitterman, L., Hirji, Z., Lemieux, C. & Gardam, M. Transmission of influenza A in human beings. *The Lancet infectious diseases* **7**, 257–65 (2007).

6. Li, K. S. *et al.* Genesis of a highly pathogenic and potentially pandemic H5N1 influenza virus in eastern Asia. *Nature* **430**, 209–13 (2004).

7. Tellier, R. Aerosol transmission of influenza A virus: a review of new studies. *Journal of the Royal Society, Interface / the Royal Society* **6 Suppl 6**, S783–90 (2009).

8. Edwards, D. A. *et al.* Inhaling to mitigate exhaled bioaerosols. *Proceedings of the National Academy of Sciences of the United States of America* **101**, 17383–8 (2004).

9. Hall, C. B. InfluenzaVirus: here, there, especially air? *The Journal of infectious diseases* **207**, 1027–9 (2013).

10. Fiegel, J., Clarke, R. & Edwards, D. A. Airborne infectious disease and the suppression of pulmonary bioaerosols REVIEWS. *Drug Discovery Today* **11**, 51–57 (2006).

11. Ross, B. B. *et al*. Physical Dynamics of the Cough Mechanism. *Journal of Applied Physiology* **8**, 264–268 (1955).

12. Yu, T. *et al.*Temporal-spatial analysis of severe acute respiratory syndrome among hospital inpatients. *Clinical Infectious Diseases* **40,** 1237–1243 (2005).

13. Cowling, B. J. *et al.* Aerosol transmission is an important mode of influenza A virus spread. *Nature Communications* **4**, 1935 (2013).

14. Blachere, F. M. *et al.* Measurement of airborne influenza virus in a hospital emergency department. *Clinical infectious diseases : an official publication of the Infectious Diseases Society of America* **48**, 438–40 (2009).

15. Yang, W., Elankumaran, S. & Marr, L. C. Concentrations and size distributions of airborne influenza A viruses measured indoors at a health centre, a day-care centre and on aeroplanes. *Journal of the Royal Society, Interface / the Royal Society* **8**, 1176–84 (2011).

16. Blachere, F. M., Cao, G., Lindsley, W. G., Noti, J. D. & Beezhold, D. H. Enhanced detection of infectious airborne influenza virus. *Journal of virological methods* **176**, 120–4 (2011).

17. Fabian, P., McDevitt, J. J., Houseman, E. a & Milton, D. K. Airborne influenza virus detection with four aerosol samplers using molecular and infectivity assays: considerations for a new infectious virus aerosol sampler. *Indoor Air* **19**, 433–41 (2009).

18. Lednicky, J. a & Loeb, J. C. Detection and Isolation of Airborne Influenza A H3N2 Virus Using a Sioutas Personal Cascade Impactor Sampler. *Influenza research and treatment* **2013**, 656825 (2013).

19. Roy, C. J. & Milton, D. K. Airborne transmission of communicable infection--the elusive pathway. *The New England journal of medicine* **350**, 1710–2 (2004).

20. Diaz, K. T. & Smaldone, G. C. Quantifying exposure risk: surgical masks and respirators. *American journal of infection control* **38**, 501–8 (2010).

21. Duran, Deniz. Investigation of the Physical Characteristics of Polypropylene Meltblown Nonwovens Under Varying Production Parameters. *Thermoplastic*

Elastomers, Adel El-Sonbati (Ed.). InTech, 2012. **Online.** Available from: http://www.intechopen.com/books/thermoplastic-elastomers/investigation-of-the-production-parameters-and-physical-characteristics-of-polypropylene-meltblown-n.

22. Farer, R. *et al.* Forming Shaped/Molded Structures by Integrating Meltblowing and Robotic Technologies. *Textile Research Journal* **73**, 15–21 (2003).

23. Dutton, K. Overview and analysis of the meltblown process and parameters. *Journal of Textile and Apparel, Technology and Management* **6**, pp. 25 (2008).

24. Khadka, D. B., Cross, M. C. & Haynie, D. T. A Synthetic Polypeptide Electrospun Biomaterial. *ACS Applied Materials & Interfaces* **3**, 2994–3001 (2011).

25. Selvakumar, N., Azhagurajan, A., Natarajan, T. S. & Khadir, M. M. A. Flame-Retardant Fabric Systems Based on Electrospun Polyamide / Boric Acid Nanocomposite Fibers. *Journal of Applied Polymer Science* **126**, 614–619 (2012).

26. Zucchelli, A., Focarete, M.L., Gualandi, C. & Ramakrishna, S. Electrospun nanofibers for enhancing structural performance of composite materials. *Polymers for Advanced Technologies* **22** (3), 339-349 (2011).

27. Subbiah, T., Bhat, G. S., Tock, R. W., Parameswaran, S. & Ramkumar, S. S. Electrospinning of nanofibers. *Journal of Applied Polymer Science* **96**, 557–569 (2005).

28. Yan, G. *et al.* Self-Assembly of Electrospun Polymer Nanofibers : A General. *Langmuir Letters* **27**, 4285–4289 (2011).

29. Pant, H. R. & Kim, C. S. Electrospun gelatin/nylon-6 composite nanofibers for biomedical applications. *Polymer International* **62**, 1008–1013 (2012).

30. Brady, George S., Clauser, Henry H. & Vaccari, John A. *Materials Handbook: An Encyclopedia for Managers, Technical Professionals, Purchasing and Production Managers, Technicians, and Supervisors (15th Ed.)*. New York, Chicago: McGraw-Hill, 2002. **Access Engineering. Web (4 Feb 2013).**

31. You, Y., Lee, S. J., Min, B.-M. & Park, W. H. Effect of solution properties on nanofibrous structure of electrospun poly(lactic-co-glycolic acid). *Journal of Applied Polymer Science* **99**, 1214–1221 (2006).

32. Hutten M. Irwin. Raw Materials for Nonwoven Filter Media. *Handbook of Nonwoven Filter Media*. Burlington, Oxford: Butterworth-Heinemann Elsevier, 2007. **Print.**

33. Li, Zhenyu & Wang, Ce. *Effects of Working Parameters on Electrospinning*. One-Dimensional Nanostructures – Electrospinning Technique and Unique Nanofibers. SpringerBriefs in Materials, 2013. **Online.**

34. Fong H, Chun I, Reneker DH. Beaded nanofibers formed during electrospinning. *Polymer* **40**, 4585–4592 (1999).

35. Yang Q, Li Z, *et al.* Influence of solvents on the formation of ultrathin uniform poly(vinyl pyrrolidone) nanofibers with electrospinning. *Journal of Polymer Science, Part B: Polymer Physics* **42,** 3721–3726 (2004).

36. Chowdhury, M. & Stylios, G. Effect of experimental parameters on the morphology of electrospun Nylon 6 fibres. *International Journal of Basic & Applied Sciences* **10**, 116–131 (2010

37. Yördem OS, Papila M, Menceloğlu YZ. Effects of electrospinning parameters on polyacrylonitrile nanofiber diameter: An investigation by response surface methodology. *Materials & Design* **29**, 34–44 (2008).

38. Huang C, *et al*. Electrospun polymer nanofibres with small diameters. *Nanotechnology* **17**, 1558–1563 (2006).

39. Hosseini, S. A. & Tafreshi, H. V. On the importance of fibers' cross-sectional shape for air filters operating in the slip flow regime. *Powder Technology* **212**, 425–431 (2011).

40. Li, L., Frey, M. W. & Green, T. B. Modification Of Air Filter Media With Nylon-6 Nanofibers. *The Journal of Engineered Fibers and Fabrics* **1**, (2006).

41. Graham, K., Ouyang, M., Raether, T., Grafe, T., McDonald, B., Knauf P. Polymeric Nanofibers in Air Filtration Applications, Advances in Filtration and Separation Technology, Proceedings of the American Filtration and Separations Society, 16, paper 1 session 14, Galveston, TX, 2002.

42. Brown, R.C. *Air filtration: an integrated approach to the theory and applications of fibrous filters*. New York, Oxford: Pergamon Press, 1993. **Print**.

43. Hinds, W.C. Aerosol Technology: Properties, Behavior, and Measurement of Airborne Particle (2nd Ed). New York: John Wiley & Sons, 1999. Print.

44. Pich, Josef. Pressure characteristics of fibrous aerosol filters. *Journal of Colloid and Interface Science* **37,** 912–917 (1971).

45. Jung, Chang H. & Lee, K. W. Analytic Solution for Diffusional Filtration across Granular Beds in Low Knudsen Number Regime. *Particle & Particle Systems Characterization* **21,** 234–242 (2004).

46. McKee, M. G.; Hunley, M. T.; Layman, J. M.; Long, T. E. Solution Rheological Behavior and Electrospinning of Cationic Polyelectrolytes. *Macromolecules* **39**, 575-583 (2006).

47. Gan, J.A. & Berndt, C.C. Quantification and Taxonomy of Pores in Thermal Spray Coatings by Image Analysis and Stereology Approach. *Metallurgical and Materials Transactions A* **44**, 4844-4858 (2013).

48. Alyamani A. & Lemine, O.M.. FE-SEM Characterization of Some Nanomaterial, Scanning Electron Microscopy, Viacheslav Kazmiruk (Ed.). InTech, 2012. Available from: http://www.intechopen.com/books/scanning-electron-microscopy/fe-sem-characterization-of-some-nanomaterials-

49. Boyes, E.D. Aberration Minimized FESEM for Nanotechnology Applications. *Microscopy and Microanalysis* **10**, 36-37 (2004).

50. Zhou, W., Apkarian, R., Wang, Z.L., & Joy, D. Fundamentals of Scanning Electron Microscopy. *Scanning Microscopy for Nanotechnology Techniques and Applications*, Weilie Zhou, Zhong Lin Wang (Ed). Springer Verlag, 2007.

51. Zottia, M., Ferronib, A., & Calvinic, P. Mycological and FTIR analysis of biotic foxing on paper substrates. *International Biodeterioration & Biodegradation* **65**, 569-578 (2011).

52. Tanaka, M., Takeguchi, M. & Furuya, K. X-ray analysis and mapping by wavelength dispersive X-ray spectroscopy in an electron microscope. *Ultramicroscopy* **108**, 1427-1431 (2008).

53. Houk, C.S. & Page, C.J. Mapping the Elemental Distribution in Sol-Gel Derived Ceramics. *Advanced Materials* **8**, 173–176 (2004).

54. Iordanidis, A., Buckman, J., Triantafyllou, A. G., & Asvesta, A. ESEM–EDX characterisation of airborne particles from an industrialised area of northern Greece. *Environmental Geochemistry and Health* **30**, 391–405 (2008).

55. Laskin, A. & Cowin, J.P. Automated Single-Particle SEM/EDX Analysis of Submicrometer Particles down to 0.1 um. *Analytical Chemistry* **73**, 1023-1029 (2001).

56. Yang, L., Hedhammar, M., Blom, T., Leifer, K. *et al*. Biomimetic calcium phosphate coatings on recombinant spider silk fibres. *Biomedical Materials* **5**, ID: 045002, 10pp, (2010).

57. Panich, I. An overview of differential mobility analyzers for size classification of nanometer-sized aerosol particles. *Songklanakarin Journal of Science and Technology* **30**, 243-256 (2008).

58. Guha, S., Li, M., Tarlov, M. J., Zachariah, M. Electrospray-differential mobility analysis of bionanoparticles. *Trends in Biotechnology* **30**, 291-300 (2012).

59. Flagan, R.C. History of Electrical Aerosol Measurements. *Aerosol Science and Technology* **28**, 301-380 (1998).

60. Xiong, C. & Friedlander, S. K. Morphological properties of atmospheric aerosol aggregates. *PNAS* **98,** 11851-11856 (2001).

61. Suvajyoti, G., Pease III, L. F., Brorsond, K. A., Tarlova, M. J., & Zachariah M. R. Evaluation of electrospray differential mobility analysis for virus particle analysis: Potential applications for biomanufacturing. *Journal of Virological Methods* **178**, 201-208 (2011).

62. Pease, L.F. Physical analysis of virus particles using electrospray differential mobility analysis. *Trends in Biotechnology* **30**, 216-224 (2012).

63. Pinkerton, K. E., Gallen, J. T., Mercer, R. R., Wong, V. C. *et al*. Aerosolized fluorescent microspheres detected in the lung using confocal scanning laser microscopy. *Microscopy Research and Technique* **26**, 437–443 (1993).

64. Sathe, T.R, Agrawal, A. & Nie, S. Mesoporous Silica Beads Embedded with Semiconductor Quantum Dots and Iron Oxide Nanocrystals: Dual-Function Microcarriers for Optical Encoding and Magnetic Separation. *Analytical Chemistry* **78**, 5627-5632 (2006).

65. Chamot, E.M. & Mason, C.W. The Handbook of Chemical Microscopy. New York: John Wiley and Sons Inc., 1966. **Print**.

66. Seely, B.K. Detection of Micron and Submicron Chloride Particles. *Analytical Chemistry* **24**, 576-579 (1952).

67. Harvey, D. Electrochemical Methods of Analysis. *Modern Analytical Chemistry*. New York: McGraw-Hill Inc., 2004. **Print**.

68. Smith, S.H. Temperature Correction in Conductivity Measurements. *Limnology and Oceanography* **7**, 330-334 (1962).

69. Yoo, H.S., Kim, T.G., & Park, T. G. Surface-functionalized electrospun nanofibers for tissue engineering and drug delivery. *Advanced Drug Delivery Reviews* **61**, 1033–1042 (2009).

70. Chew, S.Y. & Park, T.G. Nanofibers in Regenerative Medicine and Drug Delivery. *Advanced Drug Delivery Reviews* **61**, 987 (2009).

71. Yang F., Wolke J. G. C., & Jansen J.A. Biomimetic calcium phosphate coating on electrospun poly (epsilon-caprolactone) scaffolds for bone tissue engineering. *Chemical Engineering Journal* **137**, 154–161 (2008).

72. Wang, P., Wang, Y., Tong, L. Functionalized polymer nanofibers: a versatile platform for manipulating light at the nanoscale. *Light: Science & Applications* **2**, p. e102 (2013).

73. Bellan, L.M., Cross, J.D., Strychalski, E.A., Moran-Mirabal, J. & Craighead, H.G. Individually resolved DNA molecules stretched and embedded in electrospun polymer nanofibers. *Nano Letters* **6**, 2526-2530 (2006).

74. Kim, C.K, Nair, S., Kim, J., Kwak, J.H, Grate, J.W. *et al.* Preparation of biocatalytic nanofibres with high activity and stability via enzyme aggregate coating on polymer nanofibers. *Nanotechnology* **16**, S382 (2005).

75. Agarwal, S., Wendorff, J. H., & Greiner, A. Chemistry on Electrospun Polymeric Nanofibers: Merely Routine Chemistry or a Real Challenge? *Macromolecular Rapid Communications* **31**, 1317–1331 (2010).

76. Yoon, K., Hsiao, B.S., Chu, B. Functional nanofibers for environmental applications. *Journal of Materials Chemistry* **18**, 5326-5334 (2008).

77. Agarwal, S., Wendorff, J. H., & Greiner, A. Use of electrospinning technique for biomedical applications. *Polymer* **49,** 5603–5621 (2008).

78. Lee, K. H., Kim, D. J., Min, B. G., Lee, S. H. Polymeric nanofiber web-based artificial renal microfluidic chip. *Biomedical Microdevices* **9**, 435-442 (2007).

79. Park, S. P., Kim, J. M., Lee, S. J., Lee, S. G., Jeong, Y. K. *et al*. Surface hydrolysis of fibrous poly(ε-caprolactone) scaffolds for enhanced osteoblast adhesion and proliferation. M*acromolecular Research* 15, 424-429 (2007).

80. Liu, M.Y., Zhao, Q. X., Wang, Y. D., Niu, J. F. & Cao, S. K. Nylon-6 film grafted with acrylic acid for dissepiment in alkaline storage batteries. *Polymers for Advanced Technologies* **15**, 105–110 (2004).

81. Blair, H. S., Guthrie, J., Law, T. K. & Turkington P. Chitosan and Modified Chitosan Membranes I. Preparation and Characterisation. *Journal of Applied Polymer Science* **33**, 641-656 (1987).

82. Joshi, J. M. & Sinha, V. K. Ceric Ammonium Nitrate Induced Grafting of Polyacrylamide onto Carboxymethyl Chitosan. *Carbohydrate Polymer* **67**, 427-435 (2007).

83. Tobiesen, F. A. & Michielsen, S. Method for grafting poly(acrylic acid) onto nylon 6,6 using amine end groups on nylon surface. *Journal of Polymer Science Part A: Polymer Chemistry* **40**, 719–728 (2002).

84. Anlar, S., Capan, Y. & Hincal, A. A. Physio-chemical and Bioadhesive Properties of Polyacrylic Acid Polymers. *Die Pharmazie* **48**, 285–287 (1993).

85. Hajipour, M. J. *et al.* Antibacterial properties of nanoparticles. *Trends in Biotechnology* **30**, 499–511 (2011).

86. Grabarek, Z. & Gergely, J. Zero-length crosslinking procedure with the use of active esters. *Analytical Biochemistry* 185, 131–135 (1990).

87. Hoare, D. G. & Koshland, Jr, D. E. Method for the Quantitative Modification and Estimation of Carboxylic Acid Groups in Proteins. *The Journal of Biological Chemistry* **242**, 2447-2453 (1967).

88. Kale, K. H. & Desai, A. N. Atmospheric pressure plasma treatment of textiles using non-polymerising gases. *Indian Journal of Fibre & Textile Research* **36**, 289-299 (2011).

89. Morent, R., De Geyter, N., Verschuren, J., De Clerck, K. *et* al. Non-thermal plasma treatment of textiles. *Surface and Coatings Technology* **202**, 3427-3449.

90. Clough, R. High-energy radiation and polymers: A review of commercial processes and emerging applications. *Nuclear Instruments and Methods in Physics Research Section B: Beam Interactions with Materials and Atoms* **185**, 8-33 (2001).

91. Nho, Y. C., Mook, L. Y. & Moo, Y. L. Preparation, properties and biological application of pH-sensitive poly(ethylene oxide) (PEO) hydrogels grafted with acrylic acid(AAc) using gamma-ray irradiation. *Radiation Physics and Chemistry* **71**, 239-242 (2004).

92. El-Naggar, A. M., El-Salmawi, K., Ibraheim, S. M. & Zahran, A. H. Direct Radiation Grafting of Acrylic Acid to Nylon-6 Fabric and the Behaviour of the Resulting Graft Copolymer. *Polymer International* **38**, 125-139 (1995).

93. Busfield, W. K. & Watson, G. S. Free radical activity in gamma-irradiated polyethylene film, drawn tape and ultra-high modulus fibres determined by grafting performance. *Polymer International* **54**, 1047-1054 (2005).

94. Li, B., Feng, Y., Ding, K. W., Qian, G., Zhang, X. B. *et* al. The effect of gamma ray irradiation on the structure of graphite and multi-walled carbon nanotubes. *Carbon* **60**, 186-192 (2013).

95. Bobadilla-Sanchez, E. A., Martinez-Barrera, G., Brostow, W. & Datashvili, T. Effects of polyester fibers and gamma irradiation on mechanical properties of polymer concrete containing CaCO3 and silica sand. *Express Polymer Letters* **3**, 615-620 (2009).

96. Schrote, K. & Frey, M.W. Effect of irradiation on poly(3,4-ethylenedioxythiophene):poly(styrenesulfonate) nanofiber conductivity. *Polymer* **54**, 737-742 (2013).

97. He, C., Feng, W., Cao, L. & Fan, L. Crosslinking of poly(L-lactide) nanofibers with triallyl isocyanutrate by gamma-irradiation for tissue engineering application. *Journal of Biomedical Materials Research. Part A* **99**, 655-665 (2011).

98. Huglin, M. B., & Johnson, B. L. Graft copolymerisation of acrylic acid to nylon-6 by mutual irradiation – Part 3: Influence of radiation intensity and monomer diffusion. *Colloid and Polymer Science* **249**, 1080-1084 (1971).

99. Huglin, M. B., & Johnson, B. L. Graft copolymerization of acrylic acid to nylono6 by mutual irradiation – Part 4: Influence of monomer concentration *European Polymer Journal* **8**, 911-920 (1972).

100. Tuladhar, E., Hazeleger, W. C., Koopmans, M., *et al*. Residual Viral and Bacterial Contamination of Surfaces after Cleaning and Disinfection. *Applied and Environvironmental Microbiology* **78,** 7769-7775 (2012).

101. Smith, A. L. Principles of Microbiology, 10th ed. (Mosby College Publishers, St. Louis, 1995) pp. 145.

102. Walton, W. H. Feret's Statistical Diameter as a Measure of Particle Size. *Nature* **162**, 329-330 (1948).

103. Merkus, H. G. Particle Size, Size Distributions and Shape. *Particle Size Measurements: Fundamentals, Practice, Quality*. Particle Technology Series **17** Springer. Online **(**2009).

104. Liu, X., Wu, Q., Berglund, L. a. & Qi, Z. Investigation on Unusual Crystallization Behavior in Polyamide 6/Montmorillonite Nanocomposites. *Macromolecular Materials and Engineering* **287**, 515–522 (2002).

105. Karacan, I. & Baysal, G. Investigation of the effect of cupric chloride on thermal stabilization of polyamide 6 as carbon fiber precursor. *Fibers and Polymers* **13**, 864–873 (2012).

106. Liu, Y., Cui, L., Guan, F., Gao, Y. & Hedin, N. Crystalline morphology and polymorphic phase transitions in electrospun nylon-6 nanofibers. *Macromolecules* **40**, 6283–6290 (2007).

107. Yu, J. *et al.* Thermal Conductivity and Heat Capacity of a Nylon-6⁄Multi-wall Carbon Nanotube Composite Under Pressure. *International Conference on Times of Polymers (TOP) and Composites* 145–147 (2010). doi:10.1063/1.3455559

108. Beer, F, Johnston, R, Dewolf, J, & Mazurek, D. (2009). Mechanics of materials. New York: McGraw-Hill companies pgs50-60

109. Warner, S. B. Mechanical Properties of Fibers: Shear, Bending, Torsion and Compression. *Fiber Science*. New Jersey: Prentice Hall (1995).

110. Morton, W.S. & Hearle, J.W.S. *Physical Properties of Textile Fibers.* London: The Textile Institute and Heinemann (1975).

111. Peters, L. & Woods, H.J. Creep and relaxation. *R. Meredith (Ed.), The Mechanical Properties of Textile Fibres.* Amsterdam: North-Holland Publishing Co. (1956).

112. Deitzel, J. M., Kleinmeyer, J., Harris, D. & Beck Tan, N. C. Corresponding author contact information The effect of processing variables on the morphology of electrospun nanofibers and textiles. *Polymer* **42**, 261–272 (2001).

113. Lee, K. H, Kim, H. Y., Khil, M. S. Ra, Y. M. *et al.* Characterization of nano-structured poly(1-caprolactone) nonwoven mats via electrospinning *Polymer* **44,** 1287–1294 (2003).

114. Hummel, D. O. & Scholl, F. K. *Infrared analysis of polymers, resins, and additives; an atlas (Volumes 1, 2)*. University of Michigan: Hanser (1969).

115. Enlow, E. M., Kennedy, J. L., Nieuwland, A. A., Hendrix, J. E., Morgan, S. L. Discrimination of Nylon Polymers Using Attenuated Total Reflection Mid-infrared Spectra and Multivariate Statistical Techniques. *Applied Spectroscopy* **59**, 986-992 (2005).

116. Arimoto, H. *et al*. α–γ Transitions of nylon 6. *Journal of Polymer Science A* **2**, 2283–2295 (1964). doi: 10.1002/pol.1964.100020520

117. Scheirs, J. *Compositional and Failure Analysis of Polymers: A Practical Approach.* West Sussex: Wiley & Sons, Ltd. (2000), pp. 165-166.

118. Dehabadi, V. A., Buschmann, H. J., & Gutmann, J. S. Durable press finishing of cotton fabrics with polyamino carboxylic acids. *Carbohydrate Polymers* **89**, 58-563 (2012).

119. Gillingham, E. L., Lewis, D. M., & Voncina, B. An FTIR Study of Anhydride Formation on Heating Butane Tetracarboxylic Acid in the Presence of Various Catalysts. *Textile Research Journal* **69**, 949-955 (1999).

120. Parthasarathy, V., Dhanalakshm, V. & Anbarasan, R. FTIR and thermal studies on esters grafted HDPE. *Current Chemistry Letters* **2**, 135-144 (2013).

121. Mukherjee, A. K. & Goel, H. R. Characterization of nylon 6 fibers grafted by acrylic monomers. *Angewandte Makromolekulare Chemie*, **121**, 195–208 (1984).

122. Do, C. H., Pearce, E. M., Bulkin, B. J. & Reimschuessel, H. K. FT-IR Spectroscopic Study on the Photo-and Photooxidative Degradation of Nylons. *Journal of Polymer Science Part A: Polymer Chemistry* **25**, (2003).

123. Roger, A., Sallet, D. & Lemaire, J. Photochemistry of aliphatic polyamides. 4. Mechanisms of photooxidation of polyamides 6, 11, and 12 at long wavelengths. *Macromolecules* **19**, 579-584 (1986).

124. Chou, F. Y., Shih, C. M., Tsai, M. C., Chiu, W.Y. *et al.* Functional acrylic acid as stabilizer for synthesis of smart hydrogel particles containing a magnetic Fe3O4 core. *Polymer* **53**, 2839-2846 (2012).

125. Petrovic, S. C., Zhang, W. & Ciszkowska, M. Preparation and Characterization of Thermoresponsive Poly(N-isopropylacrylamide-co-acrylic acid) Hydrogels: Studies with Electroactive Probes. *Analytical Chemistry* **72**, 3449-3454 **(**2000).

126. Brunauer, S., Deming, L. S., Deming, W.E. & Teller, E. J. On a Theory of the van der Waals Adsorption of Gases. *Journal of the American Chemical Society* **62**, 1723-1732 (1940).

127. Schneider, P. Adsorption isotherms of microporous-mesoporous solids revisited. *Applied Catalysis A: General* **129**, 157-165 (1995).

128. Desai, R., Tomar, J. L. & Chakrabarty, B. S. Thermal analysis of microwave assisted synthesized poly(acrylic) acid/alumina composites. *AIP Conference Proceedings* **1536**, 897-898 (2013).

129. Engelhardt, F., Ebert, G. & Funk, R. Cross-linking in water-absorbent polymers. *Advanced Materials* **4,** 227–230 (1992).

130. Degoutin, S., Martel, B., Jimenez, M., Casetta, M., *et* al. Anticoagulant and antimicrobial finishing of non-woven polypropylene textiles. *Biomedical Materials* **7**, ID: 035001 (2012).

131. . Marple, V.A & Liu, B.Y.H. Characteristics of Laminar Jet Impactors. *Environmental Science and Technology* **8**, 648 – 654 (1974).

132. Rubow, K.L., Marple, V.A., Olin, J.G. & McCawley, M.A. A Personal Cascade Impactor: Design, Evaluation and Calibration. *American Industrial Hygiene Association Journal* **48**, 532–538 (1987).

133. Ranđelović, M.S, Zarubica, A. R. & Purenović, M. M. *New Composite Materials in the Technology for Drinking Water Purification from Ionic and Colloidal Pollutants, Composites and Their Applications*, Ning Hu (Ed.). InTech, 2012. Available from: http://www.intechopen.com/books/composites-and-their-applications/new-composite-materials-in-the-technology-for-drinking-water-purification-from-ionic-and-colloidal-p

134. Ribeiro, D. V., Labrincha, J. A. & Morelli, M. R. Chloride diffusivity in red mud-ordinary portland cement concrete determined by migration tests. *Materials Research* **14,** 227-234 (2011).

135. Mamunya, Y. Carbon Nanotubes as Conductive Filler in Segregated Polymer Composites - Electrical Properties, Carbon Nanotubes - Polymer Nanocomposites, Dr.

Siva Yellampalli (Ed.), ISBN: 978-953-307-498-6, InTech, DOI: 10.5772/18878. Available from: http://www.intechopen.com/books/carbon-nanotubes-polymer-nanocomposites/carbon-nanotubes-as-conductive-filler-in-segregated-polymer-composites-electrical-properties

136. Wickman, H. H. & Korley, J. N. Colloid crystal self-organization and dynamics at the water/air surface. *Letters to Nature* **395**, 445-447 (1998).

137. Langer, J. S. Instabilities and pattern formation in crystal growth. *Reviews of Modern Physics* **52**, 1-30 (1980).

138. Grouchko, M., Popov, I., Uvarov, V., *et al*. Coalescence of Silver Nanoparticles at Room Temperature: Unusual Crystal Structure Transformation and Dendrite Formation Induced by Self-Assembly. *Langmuir* **25**, 2501-2503 (2009).

139. Neeleshwar, S., Chen, C. L., Tsai, C. B. & Chen, Y. Y. Size-dependent properties of CdSe quantum dots. *Physical Review B* **71**, ID: 201307(R) (2005).

140. Gao, X., Yang, L., Petros, J. A., Marshall, F. F. *et al*. *In vivo* molecular and cellular imaging with quantum dots. *Current Opinion in Biotechnology* **16**, 63-72 (2005).

141. Zrazhevskiy, P., Sena, M. & Gao, X. Designing multifunctional quantum dots for bioimaging, detection, and drug delivery. *Chemical Society Review* **39**, 4326-4354 (2010).

142. Xu, Lizhi *et* al. 3D multifunctional integumentary membranes for measurements and stimulation across the entire epicardium. *Nature Communications* **5,** Article #: 3329 (2014).

143. Meng, G., Paulose, J. Nelson, D. R., & Manoharan, V. N. Elastic Instability of a Crystal Growing on a Curved Surface. *Science* **7**, 634-637 (2014).

144. Braghirolli, D. I*.,* Steffens, D*.,* Quintiliano, K*, &* Acasigua, G. A. X. *et al*. The effect of sterilization methods on electronspun poly(lactide-*co*-glycolide) and subsequent

adhesion efficiency of mesenchymal stem cells. *Journal of Biomedical Materials Research Part* B **102B**, 700–708 (2014).

145. Thomas,M.V., Chowdhury, J.S., Sullivan,J.F., Dean, D.R. et al. Polymer Edn Mechano-morphological studies of aligned nanofibrous scaffolds of polycaprolactone fabricated by electrospinning. *Biomaterial Science Polymer Ed*. **17**, 969-984 (2006).

146. Meng, Z. X., Wang, Y. S., Ma, C., Zheng, W. et al. Electrospinning of PLGA/gelatin randomly-oriented and aligned nanofibers as potential scaffold in tissue engineering. *Materials Science & Engineering C* **30**, 1204 - 1210 (2010).

147. Reneker, D. H. & Yarin, A. L. Electrospinning jets and polymer nanofibers. *Polymer* **49**, 2387-2425 (2008).